Mechanical Motion Oscillator Based on Energy/Phase Control for Legged Robots

January 2022

ABE, Yoshitaka

A Thesis for the Degree of Ph.D. in Engineering

Mechanical Motion Oscillator Based on Energy/Phase Control for Legged Robots

January 2022

Graduate School of Science and Technology
Keio University

ABE, Yoshitaka

Acknowledgements

I have researched at Katsura Laboratory since my 4th-year undergraduate, 2012. This dissertation is the summary of my recent research in this several years. The experiences I have had in the laboratory are irreplaceable and valuable to me. Here, I would like to express my gratitude to all the people who have supported me.

Firstly, I would like to express my sincere gratitude to my supervisor Professor Dr. Seiichiro Katsura, Department of System Design Engineering, Keio University. He taught me attitudes as a researcher: a passion for novel research and a methodology to conduct research logically and smartly. His warm heart as an educator motivated me to overcome the difficulties of research many times. He provided many opportunities to improve research abilities: research discussion at the laboratory, academic conferences, exhibitions, etc. It was very precious that he spared much time to research discussions despite his busy schedule. It is a lifelong fortune for me to have learned and researched under him.

I would like to offer my special thanks to the members of my Ph.D. dissertation committee, Professor Dr. Jingang Yi, Department of Mechanical and Aerospace Engineering, Rutgers University, Professor Dr. Masaki Takahashi, Department of System Design Engineering, Keio University, and Associate Professor Dr. Genya Ishigami, Department of Mechanical Engineering, Keio University.

I would appreciate to professors who gave precious comments at SUM meetings: Professor Dr. Kouhei Ohnishi, Professor Dr. Toshiyuki Murakami, Professor Dr. Hiroaki Nishi, Professor Dr. Takahiro Yakoh, and Senior Lecturer Dr. Takahiro Nozaki in Keio University. Their kind and insightful advice were significant to raise the level of my research.

I would also like to convey my deep gratitude to Professor Dr. Jingang Yi at Rutgers University. He was my supervisor while I was at Rutgers University for the joint research. He supported my research many times: the instruction at Rutgers University, the research discussion at the academic conference, and the instruction at Keio University. Dr. Kuo Chen and Dr. Mitja Trkov were co-researchers at Rutgers University. They helped me very much both publicly and privately. I could not have spent such a fruitful time without Dr. Yi's and their kind help.

I would appreciate the Keio Program for Leading Graduate School and MEXT (Ministry of Education, Culture, Sports, Science and Technology). The program provided me many opportunities: studying

abroad, presenting at international conferences, field works, etc. These experiences and the bonds with the people related to this program are irreplaceable for me.

I would like to appreciate the organizations for financial support. Keio Engineering Foundation and Tamura Atsushi Memorial Scholarship helped me to continue the Ph.D. research financially. Keio Leading-edge Laboratory of Science and Technology (KLL) Ph.D. Program Research Grant has provided me the chance to manage the research expense by myself.

I am deeply grateful to the people of Meidensha Corporation, represented by President Takeshi Miida. My supervisors of the company, Mr. Yugo Tadano, Mr. Shota Urushibata, Dr. Hajime Kubo, Mr. Masashi Takiguchi, and Mr. Kento Yoshida showed understanding of the Ph.D. research while working. My colleague Dr. Hayato Higa gave me insights about completing the doctoral course.

I would like to appreciate the members of Katsura laboratory. I would deeply thank Dr. Eiichi Saito and Dr. Hiroki Nagashima, who are my seniors in Katsura laboratory. They gave me a lot of kind advice. I would like to express my gratitude to the members who researched legged robots together at Katsura Laboratory: Dr. Kazumasa Miura, Mr. Masahiro Komuta, Mr. Yuji Ogitani, Mr. Masaki Takeuchi, Mr. Takuya Shimura, and Mr. Kazuma Morikawa. Especially, Mr. Masaki Takeuchi, Mr. Takuya Shimura, and Mr. Kazuma Morikawa helped me with conducting the additional experiments of this dissertation. Dr. Hiroki Kurumatani gave me insights about motion control of the leg robots. I would like to express my gratitude to the members who joined Katsura laboratory in the same year: Dr. Satoshi Nishimura, Mr. Hiroki Onoyama, Mr. Yusuke Kawamura, Mr. Koichiro Nagata, and Mr. Takami Miyagi. We improved our abilities and cheered up each other. I would appreciate everyone who collaborated with and helped me in Katsura Laboratory. The things which I obtained at this laboratory are precious for me.

Finally, I would like to express my deep gratitude to my family who has supported me warmly. I could focus on research thanks to their warm supports.

January, 2022
Yoshitaka Abe

Table of Contents

List of Figures

List of Tables

Chapter 1

Introduction

1.1 Background of This Dissertation

Labor shortage is a serious issue in recent society, especially in Japan. Robots are expected to be a solution to the labor shortage. Application of robots is being developed continuously [1]. Although an automatic guided vehicle (AGV) [2–4] is already applied to the logistics industry, robots are being applied to other fields: a service robot [5], a security robot [6, 7], a disinfection robot [8], etc. While wheel-type robots are popular in industry applications, legged robots are being applied to industries such as Spot [9] and DIGIT [10]. One advantage of legged robots is the ability to move on uneven ground like steps or stairs. Another advantage of a biped robot is that biped locomotion has an affinity to a human. Human living space is often designed based on biped locomotion. Pedaling tasks and riding a Segway also become available if the leg structure of the robot is biped [11, 12]. A biped robot contribudes to realistic sensations in tele-existance [13, 14] in tems of the leg motion [15–17]. Also, research of legged robot control gives insights to verify the principle of legged locomotion. For example, biped robots can help to demonstrate and prove concepts of human locomotion [18].

The energy efficiency of a robot is one of the important issues [19]. Energy saving is important in terms of the limitation of battery capacitance. In general, a legged robot mounts a battery as an energy source. Because the size and the weight of the battery are limited, the battery capacity is also limited. In order to operate a legged robot for a long time with a limited battery, energy efficiency is important. From these backgrounds, the focused technical issue of this dissertation is to attain legged functions with energy efficiency. The main function of legged motion control is locomotion. The represented locomotion is walking. Moreover, it is also considered that a legged robot will need to get over stepping stones or a small stream for such as delivery to a mountainous area. In such applications, vertical hopping control is the basic problem. This dissertation considers legged hopping motion control as well as walking control.

1.1.1 Energy/Phase Control as a Motion Oscillator

Control engineering has often dealt with stability, tracking performance, robustness against parameter variation, disturbance response, etc. On the other hand, energy efficiency has not been dealt much with. Classical control theory is systemized using Laplace transformation and a transfer function. An input-output transfer function can analyze the tracking performance without disturbance. Transfer functions also enable to analyze the disturbance response and the robustness against parameter variation.

Energy efficiency is also being an important issue for control problems in industries. A quadratic optimal regulator in modern control engineering can design the input to decrease the energy consumption (concretely the quadratic form of the input vector) [20,21]. However, it is difficult for the optimal control method to tune the energy efficiency directly.

Power factor is an index of efficiency for power transmission in electrical engineering. Mizoguchi et al. extended the concept of the power factor into a mechanical system, and proposed mechanical power factor [22, 23]. In the previous researches about the mechanical power factor, the mechanical power factor is mainly used for analysis [22–24]. Few kinds of research explicitly applied the mechanical power factor to the design of the control.

As one research related to utilizing power factor to control, De et al. [25, 26] proposed an efficient hopping control “energy pumping.” A spring-mass system is oscillated by synchronizing the actuation phase to the vibration phase. However, it is difficult for energy pumping to control the hopping height (or the mechanical energy) directly.

As related researches considering both energy and phase, Kusaka [27–29] and Kajiwara employed periodic input control. A redundant degree of freedom is required for periodic input control. The phase in periodic input control is the phase difference between the two degrees of freedom. Kajiwara et al. conducted hopping-height control by controlling the phase difference between the body and the arms [30]. Kusaka et al. conducted skill-assist control by controlling the phase difference between the human handle and the actuator [30]. A difficulty of periodic input control is that a redundant degree of motion is required. Also, because the phase in periodic input control does not mean power factor, the energy-efficient oscillation like energy pumping is not discussed.

1.1.2 Nominalization Control

As for compensation control for nominalization to simple dynamics, there are some popular methods. Feedback linearization is a popular approach that is often used in theoretical research [31]. The computed torque method is also popular in industrial applications. However, it is necessary for these methods to identify the nonlinear terms precisely. The identification is often difficult in the real world.

Disturbance observer is a popular method for the nominalization of dynamics in motion control [32–34]. A typical disturbance observer nominalizes the actuator inertia as constant. As a disturbance observer for nominalizing the mass in the workspace as constant, a joint space observer and a workspace observer are previously researched [35]. A joint space observer changes the nominal inertia to make the mass in the workspace constant. A workspace observer is a disturbance observer constructed in the dimension of the workspace. In the control system of workspace, there are two options for the transformation of the controller output from workspace to joint space [35]. The first option is the inverse of the Jacobian matrix, which is induced by kinematics. The second option is the transpose of the Jacobian matrix, which is induced from torque-force relation in static mechanics. A disadvantage of the first option is that the robot tends to become out of control near a singular posture because of the calculation of the inverse matrix. Parameter design of the mass in the workspace observer is also researched [36, 37]. Generalized Nyquist stability criterion [38] is used for the analyses of the multi-input and multi-output systems.

As well as realizing the desired mass, there are cases that the virtual spring force is required. Impedance control [39–41] adds a virtual spring-damper force in a control system. Compliance control [42, 43] is also another method to give a virtual spring-damper force. In general, impedance control calculates the virtual force from the position displacement and the velocity. Compliance control calculates the compensation position and velocity from the force response. From these characteristics, compliance control is often applied to the position control system. Impedance control is easy to use in the case that the compensation force should be calculated.

1.1.3 Hopping Robot and Hopping-Height Control

A hopping robot has been researched by many researchers [44]. The initial researches of a hopping robot are conducted by Matsuoka et al. [45] and Raibert et al. [46, 47]. Many kinds of research of a hopping robot utilize the spring-mass dynamics. It is shown that hopping and running motions can be modeled as a simple spring-mass model [48]. The advantage of employing a mechanical spring is to supply additional power from the potential energy. This advantage is significant because actuator power is often low compared to the required power for hopping. The hopping robot in Raibert [47] utilizes an air spring. Okubo et al. [49] use a mechanical spring for a vertical hopping robot. The total mechanical energy is amplified by utilizing the stored potential energy of the mechanical spring. “Kenken” by Hyon et al. is a famous articulated hopping robot that employs a mechanical spring and tendon drive inspired by the biomechanics of a kangaroo [50]. A monopod “Thumper” is developed by Hurst et al. in order to realize a simple spring-mass hopper utilizing a plate spring, pulley, and differential gears [51]. The monopod is extended to the biped robot named as “MABEL” [52], and MABEL attains high-speed running [53]. Reis et al. [54] realize energy-efficient hopping utilizing free vibration of a curved beam and a rotating mass.

As for control of a hopping robot, Raibert proposed the three decomposed hopping controls: the hopping-height control, the forward velocity control, and the attitude control. The hopping height is controlled by specifying the thrust force. The forward velocity is tuned by changing the position of the foot placement. The body is maintained in an upright attitude by servoing the hip during the stance. The extensibility of Raibert’s hopping strategy is also shown. 3D-running is also available using the hopping strategy [55]. The strategy is also applicable to a multi-leg robot [47, 56].

Hopping-height control is one of the difficult problems in terms of motion control. Hopping motion requires high energy, and the duration of energy injection is short. Under the difficult conditions, it is necessary to control the hopping height. Control of energy is a popular approach for hopping-height control in the case of a legged robot with a spring. This approach is simple and practical because the control goal in the stance phase becomes the constant value induced from the desired hopping height. Raibert et al. controlled hopping height by tuning the compression of the leg spring to attain the desired energy, or the desired height [46]. Ahmadi et al., Ishikawa et al., and Hyon et al. also dealt with hopping height control by controlling the energy [57–59]. On the other hand, hopping control based on phase attracts attention recently. Kajiwara et al. conducted hopping-height control by controlling the phase difference between the body and the arms [30]. De et al. [25, 26] proposed a phase control “energy pumping.” In the conventional phase control [25, 26], the spring-mass system is oscillated by synchronizing the actuation phase to the vibration phase. Energy-efficient oscillation becomes available by the conventional phase control. However, it is difficult for the conventional phase control to control the desired hopping height directly. The actuation amplitude of the conventional phase control is constant, and its design method is not discussed in detail.

1.1.4 Biped Robot and Walking Control

A biped robot has also been researched by many researchers. The textbook by Kajita et al. summarizes the history of humanoid researches [60]. WABOT-1 and 2 by Kato are ones of the initial researches of a biped robot [61, 62]. Hirose et al. in Honda R&D Corp. developed a biped robot named P2 [63]. The biped robot is autonomous and attains biped walking stably. The robot is improved moreover, and the next developed biped robot is ASIMO [64]. The improved points are lightweight, small-size, and perception with a vision system, etc. ASIMO is a famous humanoid robot in the world as well as in Japan, and has been improved continuously. The improvement is summarized totally in 2009 [65–68], and the history of the development is summarized in 2018 [69]. AIST (The National Institute of Advanced Industrial Science and Technology) developed humanoid robots HRP-2 [70]. The robot was improved as HRP-3 [71], HRP-4, and HRP-5 [72]. JAXON is also a famous biped robot, and was recently improved in terms of output power [73–75]. Many popular biped robots have been developed and improved in Japan. In Korea, HUBO and DRC-HUBO are famous biped robots developed by KAIST (Korea Advanced Institute of Science and Technology) [76–78].

Since the 2010s, some popular biped robots have been developed in USA. A biped robot Petman was developed by Boston Dynamics [79]. Boston dynamics is founded by Raibert, and also developed quadrupedal robots Bigdog [80] and Spot [9]. Atlas [9, 81] is the recent improved biped robot. MABEL [52, 82] is a biped robot with a plate spring and differential mechanism for fast walking and running. ATRIAS [83, 84] is a parallel-link biped robot with a heavy torso. Cassie is a biped robot with a light-weight torso [85–87]. Ames et al. developed a biped robot AMBER for a light-weight 2D biped walking robot based on hybrid zero dynamics: with point feet [88, 89] and with feet [90]. DURUS was also developed for 3D biped walking [91]. Martin et al. [92, 93] constructed an experimental setup of HZD (hybrid zero dynamics) walking with curved feet.

The control architecture of the representative biped walking robots is as follows. The sub controls of ATRIAS are the torso balance, the stride trajectory and, the energy injection [94]. The torso balance block conducts the control of the torso angle. The stride trajectory block generates the toe trajectory. The energy injection block outputs the extension force of leg length in response to the desired velocity. The control architecture of HRP-4C is composed of the three blocks: the walking pattern generator, the COG-ZMP feedback, and the abstracted robot [60]. The COG trajectory is designed at the upper layer, which corresponds to the walking pattern generator. The concrete stabilization control and the low-level control are implemented at the lower layers, which corresponds to the COG-ZMP feedback and the abstracted robot. The common thing of the biped control architecture in general is that a hierarchical control structure is employed. In the control architecture, the walking pattern generator (upper layer) and the stabilization control (lower layer) are separated.

As for the stabilization control, many kinds of research have been conducted. HRP-4C [95] employs the tracking control of the abstracted linear inverted pendulum. Kamioka et al. realized balance recovery by combining hopping motions and changing the foot placement [96]. Hybrid zero dynamics stabilizes a biped robot by zero dynamics [97]. For example, by determining the swing-leg trajectory in response to the body position, the dynamics of the body are designed stable. Garofalo et al. [98] employe the COG for the biped control based on hybrid zero dynamics. There is an approach to apply model predictive control to biped walking [99–101]. Stability analysis based on phase diagram is also recently popular [102].

As for the upper-layer walking pattern generator, a popular method is to utilize a general solution of a linear inverted pendulum [103, 104]. The method is applicable to a 3D linear inverted pendulum as well as 2D. As an energy-efficient walking pattern generator, Kormushev et al. [105] generates the energy-efficient COG trajectory by reinforced learning. In the work by Ding et al. [106], the energy-efficient COG trajectory is generated by optimization based on the COG acceleration of a linear inverted pendulum. Shin et al. [107] generate the energy-efficient walking gait by optimizing the gate parameter which determines the trajectories of the body and the swing foot. However, it is necessary for these methods to calculate the solution of the trajectory mathematically beforehand.

1.2 Motivation of This Dissertation

As the discussion of the background, the main function of legged motion control is locomotion. The main horizontal locomotion is walking, and the main vertical locomotion is hopping. An important value of hopping for vertical locomotion is hopping height. The dynamics of hopping are often modeled as a harmonic oscillator. The hopping height corresponds to the mechanical energy of a harmonic oscillator. An important value of walking for horizontal locomotion is walking speed. The dynamics of biped walking are often modeled as a linear inverted pendulum. Walking speed corresponds to the energy of a linear inverted pendulum. From above, both the hopping height control and the walking speed control

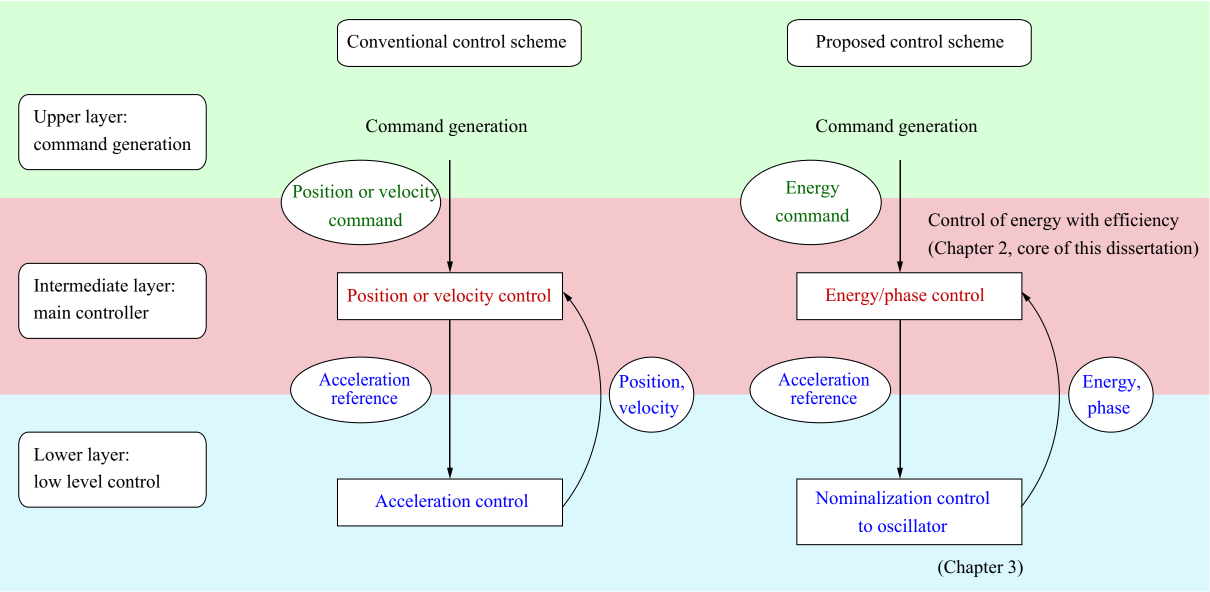

Fig. 1-1: Control schemes of the conventional motion control and the proposal.

can be transformed as the problem of the energy control. The technical problem of this dissertation can be generalized as control of energy with efficiency.

Motion control is a popular control scheme for control of robots. In motion control, acceleration control based on disturbance observer is the foundation. The acceleration control compensates the modeling error and the disturbance, which realizes the desired dynamics of a mass. On the foundation of the acceleration control, position control or velocity control are often constructed in the outer loop. In the conventional scheme, position or velocity are controlled directly. To design energy-efficient motion in the conventional control scheme, it is necessary to calculate trajectory beforehand.

On the other hand, the proposed control scheme aims at direct control of energy and efficiency. Fig. 1-1 shows the correlation of the conventional control scheme and the proposed control scheme. Although it is common that the foundation is the acceleration control, the proposed scheme controls energy and phase directly in the outer loop. The energy and the phase correspond to the polar display of the state space (scaled position and velocity) as Fig. 1-2. In Fig. 1-2, x, $\dot{x}$, and ω are the position, the velocity, and the resonant angular frequency. E and ϕ are the energy per unit mass and the phase. This research gives functions to the energy and the phase. As for the energy, a function to control the energy is implemented. As for the phase, a function of efficient oscillation is implemented. The phase control in the dissertation is to synchronize the actuation phase to the phase of the state. By adding the functions to the two variables

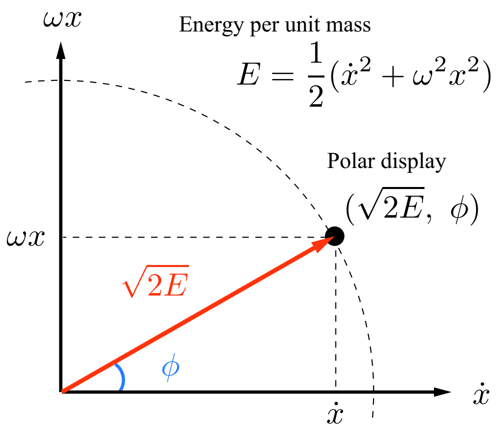

Fig. 1-2: Energy and phase of harmonic oscillator.

respectively, the proposed method attains both the energy efficiency and the energy control.

The core of this dissertation is not only for a general control method in control engineering, but also for a method of hopping height control and a method of walking velocity control. The following is the positioning of the proposal compared to the respective conventional methods.

In terms of a general control method related to energy efficiency in control engineering, few kinds of research attain both energy efficiency and energy control. Moreover, although some related methods assume the redundant system with multi-input, the proposed method requires only one input. The structure multiplying the input amplitude by the input phase enables the proposed method to attain the two requirements in one input.

As for hopping control, few kinds of research realize both hopping height control and energy-efficient hopping. Although hopping height control is often attained by energy control, there are few methods with energy efficiency. The conventional method by De et al. [25,26] has difficulty in control of hopping height while the conventional method by De et al. enables energy-efficient hopping. In the conventional method by De et al., it is necessary for realizing constant hopping height to add a damping term and to tune the damping coefficient by trial and error. On the other hand, fine parameter tuning is not necessary for the proposed energy/phase control. This is because the feedback stabilization structure of energy control is included in the energy/phase control. Because the phase control exists in the inner loop of the energy/phase control, energy efficiency as well as the energy stabilization is guaranteed.

As for walking control, the conventional control schemes are composed of the upper-layer walking pattern generator and the lower-layer stabilization control. Motions become energy-efficient when

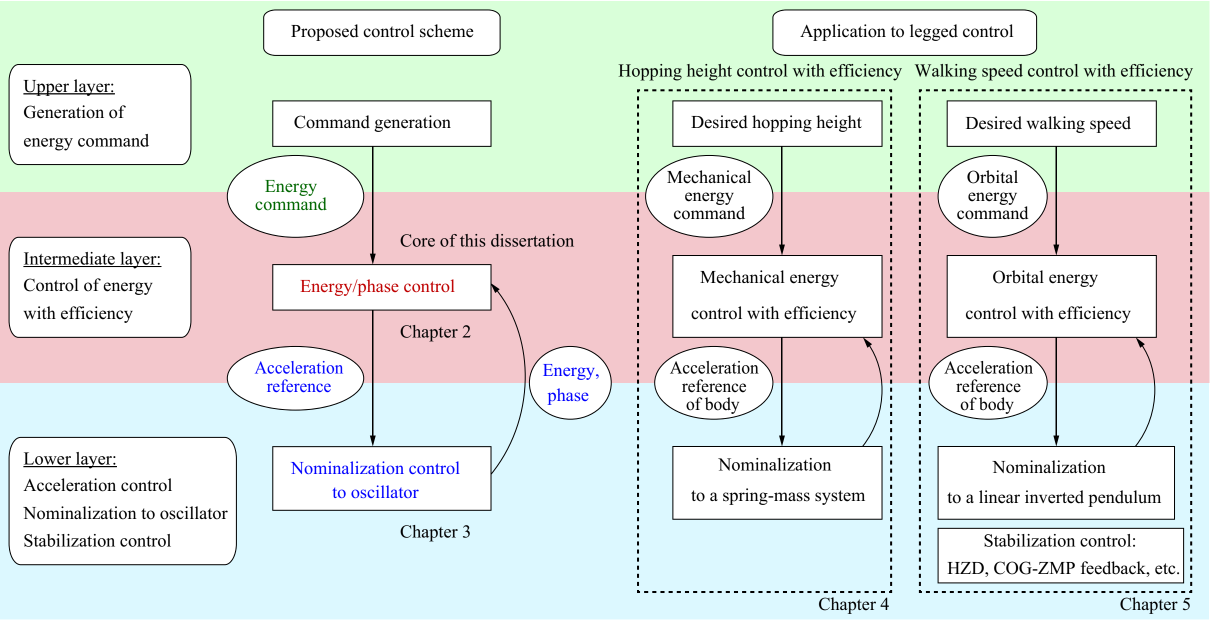

Fig. 1-3: Framework of this dissertation.

the dynamics are utilized adequately. Because biped walking can be approximated as a linear inverted pendulum, trajectory generation in the upper layer is often described using hyperbolic functions. The difficulty of the conventional method is the necessity to calculate the trajectory beforehand mathematically. Because the approach of the proposed energy/phase control is to oscillate the plant dynamics, it is not necessary to calculate the trajectory beforehand.

1.3 Organization of This Dissertation

Figs. 1-3 and 1-4 show the framework and the organization of this dissertation. The framework of Fig. 1-3 is based on the structure of hierarchical controls [108, 109]. The upper layer denotes the outermost loop, the intermediate layer is the middle outer loop, and the lower layer is the innermost loop. The motion bandwidth becomes higher in response to going down the layers. In terms of functions, the upper layer takes on the role of the command generation, the intermediate layer deals with the efficient oscillation, and the lower layer realizes the robustness. In the middle layer and the lower layer, the trade off between the energy efficiency and the robustness is designed.

In Chapter 2, the energy/phase control, which is the core of this dissertation, is described. The generalized theory for a harmonic oscillator is discussed. The proposed method enables both energy efficiency

1-3.

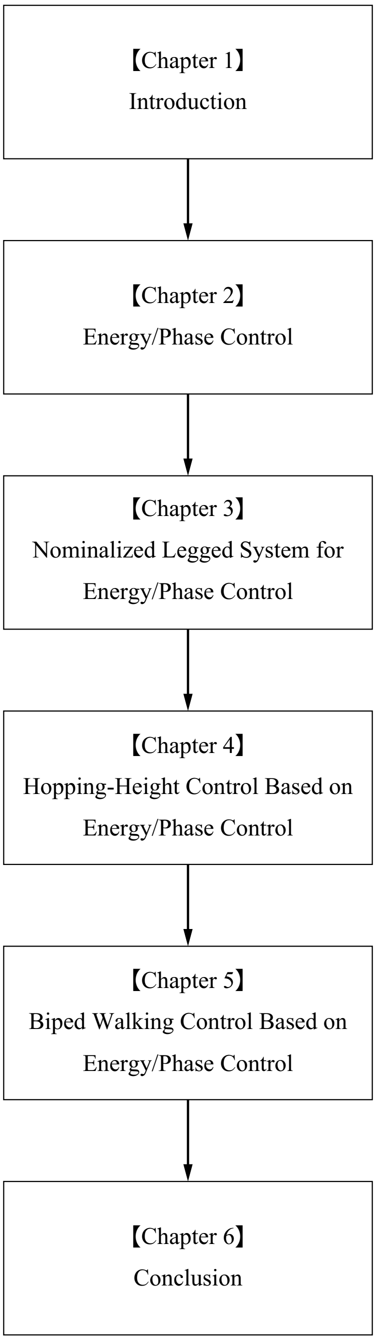

Fig. 1-4: Chapters constructed in this dissertation.

and control of energy. Analysis and comparative simulations under the dynamics of a harmonic oscillator are also conducted. Chapter 2 is located at the intermediate layer of the proposed control scheme in Fig. 1-3.

In Chapter 3, the system design of a legged robot for nominalization is discussed in order to extend the application of the energy/phase control to a multi-degree-of-freedom leg robot. In order to extend the energy/phase control for a harmonic oscillator to a legged robot, the design of the mechanics and the control are discussed. Analysis and comparative simulations under the dynamics of the legged robot are also conducted. Chapter 3 is located at the lower layer of the proposed control scheme in Fig. 1-3.

In Chapter 4, the hopping height control based on the energy/phase control is explained. The proposed energy/phase control and the legged robot system in Chapters 2 and 3 are applied to a vertical hopping motion. Because the hopping height is proportional to the vertical mechanical energy, the proposed method is easily applied. The hopping height is controlled energy efficiently. Chapter 4 corresponds to the center column of Fig. 1-3.

In Chapter 5, the biped control based on the energy/phase control is explained. The proposed energy/phase control and the legged robot system in Chapters 2 and 3 are applied to a horizontal walking motion. Biped walking dynamics are often simply modeled using a linear inverted pendulum model. The dynamics of a linear inverted pendulum and a harmonic oscillator have duality. While a general solution of a harmonic oscillator is expressed using trigonometric functions, a linear inverted pendulum is expressed using hyperbolic functions. The energy/phase control for a harmonic oscillator is extended to the one for a linear inverted pendulum. Chapter 5 corresponds to the right column of Fig. 1-3.

Finally, Chapter 6 concludes this dissertation.

Chapter 2

Energy/Phase Control

2.1 Introduction

This chapter describes the energy/phase control, which is the core of this dissertation. The energy/phase control is explained under the dynamics of a simple harmonic oscillator. The proposed energy/phase control can be said as a mechanical oscillator. Comparison with conventional methods is also conducted.

In Section 2.2, conventional energy control is explained. The proposed energy/phase control is described in Section 2.3. The energy and the phase in a harmonic oscillator are firstly defined. The phase control is introduced to enable efficient oscillation. Under the phase control, the energy control is constructed to control the system energy with efficiency. The energy/phase control is simulated, and the behavior is discussed. Section 2.4 shows the theoretical comparison of the conventional method and the proposed method, especially in terms of energy consumption, control error, and robustness. Comparative simulations are conducted in Section 2.5. The results are evaluated in terms of the three indices.

2.2 Conventional Methods of Oscillation

Van der Pol oscillator is a famous oscillator, which is expressed as

$$\ddot{x} - \mu(1 - x^2)\dot{x} + x = 0. \tag{2.1}$$

The coefficient of the velocity term is proportional to 1 minus square of the position x. μ is the constant. It can be interpreted as the potential energy control.

As a similar equation to Van der Pol oscillator, Reileigh equation is also famous. Reileigh equation is written as

$$\ddot{x} - \mu(1 - \dot{x}^2)\dot{x} + x = 0. \tag{2.2}$$

The coefficient of the velocity term is proportional to 1 minus square of the velocity $\dot{x}$. It can be interpreted as kinetic energy control.

As a hybrid of Van der Pol oscillator and Reileigh equation, energy control is introduced by some researches as

$$\ddot{x} - K_{\mathrm{p}}(E^{\mathrm{cmd}} - E)\dot{x} + \omega^2 x = 0 \tag{2.3}$$

$$E = \frac{1}{2}(\dot{x}^2 + \omega^2 x^2). \tag{2.4}$$

K_{p} is the proportional gain. E^{cmd} and E are the energy command and the energy response, respectively. The coefficient of the velocity term is proportional to the error of the energy $E^{\mathrm{cmd}} - E$. In the case of the spring-mass oscillation by the enregy control, the motion equation is

$$\ddot{x} + \omega^2 x = F_{\mathrm{a}}^{\mathrm{ref}} \tag{2.5}$$

$$F_{\mathrm{a}}^{\mathrm{ref}} = K_{\mathrm{p}}(E^{\mathrm{cmd}} - E)\dot{x}. \tag{2.6}$$

$F_{\mathrm{a}}^{\mathrm{ref}}$ is the force reference in the acceleration dimension.

2.3 Proposed Energy/Phase Control

The proposed energy/phase control is explained in this section. The energy/phase control is composed of the energy control and the phase control. The role of the phase control is to make the oscillation energy-efficient by synchronizing the phase of the force reference to the phase of the vibration. The role of the energy control is to control the amplitude of the oscillation by tuning the amplitude of the force reference.

The motion equation of the energy/phase control is expressed as

$$\ddot{x} - K_{\mathrm{p}}(A^{\mathrm{cmd}} - A)\cos\phi + \omega^2 x = 0 \tag{2.7}$$

$$A^{\mathrm{cmd}} = \sqrt{2E^{\mathrm{cmd}}} \tag{2.8}$$

$$A = \sqrt{2E} \tag{2.9}$$

$$\phi = \tan^{-1}\frac{\omega x}{\dot{x}}. \tag{2.10}$$

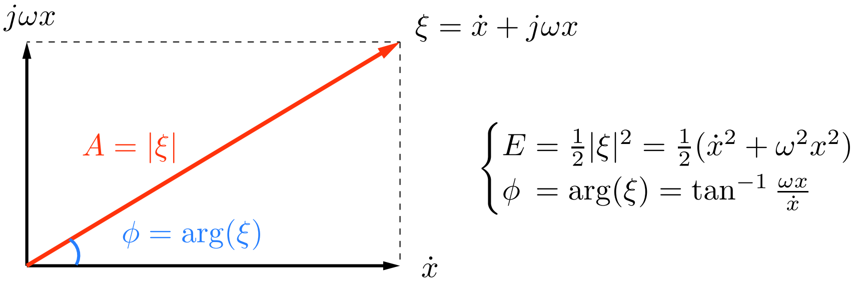

Fig. 2-1: Relation between ξ and the energy/phase in spring-mass oscillator

A^{cmd} and A are the energy-equivalent variables. ϕ is the phase.

Theoretical induction of the energy/phase control is described. Firstly, the energy and the phase are derived from the dynamics of the spring-mass oscillator. Next, the phase control is introduced for efficient oscillation. Third, the energy control under the phase control is constructed to manipulate the energy.

2.3.1 Energy and Phase of Spring-mass Oscillator

The motion equation of the spring-mass oscillator is expressed as

$$\ddot{x} + \omega^2 x = F_{\mathrm{a}}^{\mathrm{ref}}(t), \tag{2.11}$$

where ω is the resonant angular frequency and $F_{\mathrm{a}}^{\mathrm{ref}}(t)$ is the force reference in the acceleration dimension.

For calculation of the energy and the phase, a complex variable ξ

$$\xi = \dot{x} + j\omega x \tag{2.12}$$

is introduced. j is the imaginary unit. As shown in Fig. 2-1, the amplitude of ξ is proportional to the mechanical energy of the spring-mass oscillator, and the argument of ξ is equal to the phase of the spring-mass oscillator. Using ξ, the motion equation is transformed as

$$\dot{\xi} - j\omega\xi = F_{\mathrm{a}}^{\mathrm{ref}}(t). \tag{2.13}$$

The energy E and the vibration phase ϕ can be expressed using ξ as

$$E = \frac{1}{2}(\dot{x}^2 + \omega^2 x^2) = \frac{1}{2}|\xi|^2 = \frac{1}{2}A^2 \tag{2.14}$$

$$\phi = \arg(\xi) = \tan^{-1}\frac{\omega x}{\dot{x}}, \tag{2.15}$$

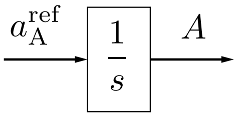

Fig. 2-2: Dynamics from the actuation amplitude $a_{\mathrm{A}}^{\mathrm{ref}}$ to the vibration amplitude A.

where the amplitude A is defined as $A = |\xi|$. "$\tan^{-1}$" in (2.15) is implemented using "atan2" function. The "atan2" function can output the value even if $\dot{x} = 0$. The amplitude A and the phase ϕ of the complex variable ξ correspond to the energy and the phase of the spring-mass oscillator.

2.3.2 Phase Control

De et al. [25, 26] proposed an oscillation method based on the phase of the spring-mass oscillator. The conventional method makes the actuation phase to be equal to the vibration phase of the spring-mass oscillator. The phase of the oscillator is induced as (2.15). Force reference $F_{\mathrm{a}}^{\mathrm{ref}}(t)$ is designed in order to synchronize with the phase of the oscillator as

$$F_{\mathrm{a}}^{\mathrm{ref}}(t) = a_{\mathrm{A}}^{\mathrm{ref}} \cos\phi, \tag{2.16}$$

where $a_{\mathrm{A}}^{\mathrm{ref}}$ is the actuation amplitude, and it is a positive constant value in the conventional method.

The advantage of the phase control is the efficiency of power transmission. Power factor indicates the efficiency of power transmission. The power factor in mechanical systems is expressed as the cosine of the phase difference between the actuation force and the velocity. The maximum power factor is 1. In this case, the force and the velocity have the same phase. The phase control in (2.16) realizes the phase synchronization, and the power factor is maximized as 1.

However, it is difficult to control the energy with efficiency by only the phase control. The previous research [25, 26] does not formulate clearly the relation between the actuation amplitude $a_{\mathrm{A}}^{\mathrm{ref}}$ and the desired energy.

2.3.3 Energy Control under Phase Control

This paper introduces a method to vary the constant $a_{\mathrm{A}}^{\mathrm{ref}}$ in order to attain the desired energy. Firstly, the dynamics of the energy under the phase control are induced. Next, the energy control system is designed based on the dynamics. By these steps, the actuation amplitude $a_{\mathrm{A}}^{\mathrm{ref}}$ is determined uniquely in real time.

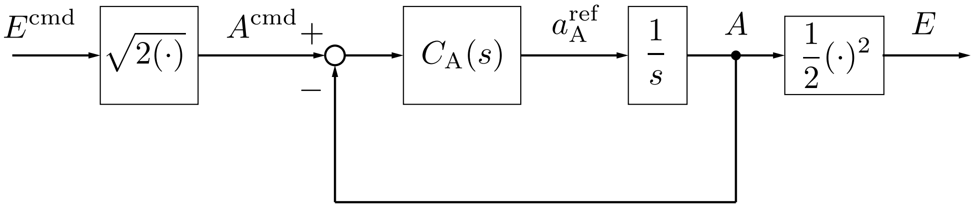

Fig. 2-3: Block diagram of the energy controller.

The first step is to induce the dynamics under the phase control. ξ of (2.12) can be transformed as $\xi = A(t)e^{j\omega t+\phi_0}$. ϕ_0 is the initial phase, or the phase at touch down. $\xi = A(t)e^{j\omega t+\phi_0}$ is substituted to the motion equation (2.13) as

$$\dot{A}(t) = F_{\mathrm{a}}^{\mathrm{ref}}(t)e^{-j(\omega t+\phi_0)}. \tag{2.17}$$

Because the actuation phase is equal to the phase of ξ by the phase control, the force input can be expressed as $F_{\mathrm{a}}^{\mathrm{ref}}(t) = a_{\mathrm{A}}^{\mathrm{ref}}(t)e^{j\omega t+\phi_0}$. The force input is substituted to the motion equation (2.17) as

$$\dot{A}(t) = a_{\mathrm{A}}^{\mathrm{ref}}(t)e^{j(\omega t+\phi_0)}e^{-j(\omega t+\phi_0)} \tag{2.18}$$

$$= a_{\mathrm{A}}^{\mathrm{ref}}(t). \tag{2.19}$$

The dynamics are expressed from the actuation amplitude $a_{\mathrm{A}}^{\mathrm{ref}}$ to the amplitude A of ξ as

$$A(s) = \frac{1}{s}a_{\mathrm{A}}^{\mathrm{ref}}(s). \tag{2.20}$$

Its block diagram is shown in Fig. 2-2.

As the next step, a feedback controller is constructed based on the dynamics as Fig. 2-3. The feedback controller is expressed as

$$a_{A}^{\mathrm{ref}} = C_{\mathrm{A}}(s)(A^{\mathrm{cmd}} - A). \tag{2.21}$$

In this paper, the feedback controller is assumed as P controller $C_{\mathrm{A}}(s) = K_{\mathrm{ep}}$ for control of a first-order system. The transfer function from the amplitude command A^{cmd} to the vibration amplitude A becomes

$$\frac{A}{A^{\mathrm{cmd}}} = \frac{K_{\mathrm{ep}}}{s + K_{\mathrm{ep}}}. \tag{2.22}$$

The transfer function is a typical first-order lag system. (2.22) indicates that the gain K_{ep} corresponds to the bandwidth of the energy control. By making the gain K_{ep} higher, it is possible to make the control bandwidth higher.

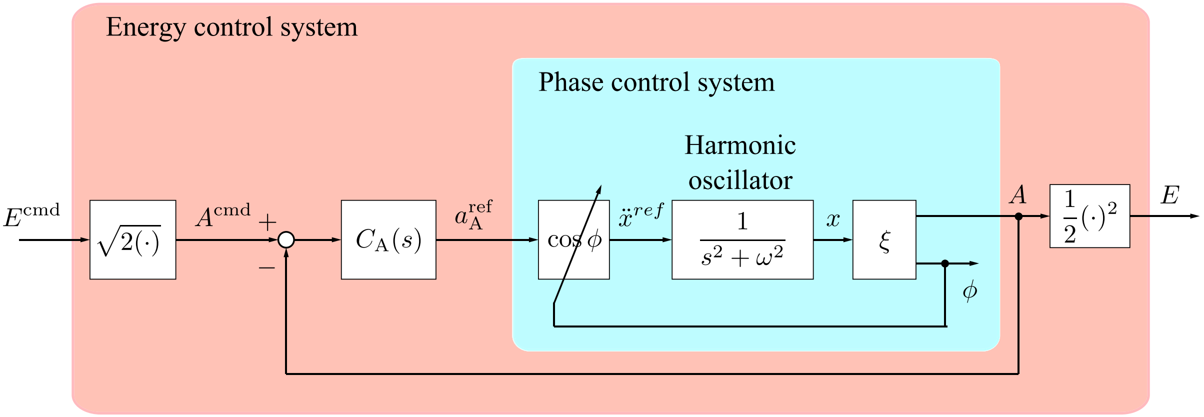

Fig. 2-4: Total block diagram of the energy/phase control.

2.3.4 Total Structure of Energy/Phase Control

The total block diagram of the energy/phase control for implementation is summarized as Fig. 2-4.

The outer loop is the energy control. The command is transformed from the energy command E^{cmd} to the amplitude command A^{cmd}. In the dimension of the amplitude, the energy control is constructed. The acceleration reference of the amplitude $a_{\mathrm{A}}^{\mathrm{ref}}$ is the reference of the energy control.

The inner loop is the phase control. The acceleration reference of the amplitude $a_{\mathrm{A}}^{\mathrm{ref}}$ is multiplied by $\cos\phi$. The calculated product is the acceleration reference $\ddot{x}^{\mathrm{ref}} (= F_{\mathrm{a}}^{\mathrm{ref}})$ for the control input. The block of $\cos\phi$ is the phase controller, which makes the control input energy-efficient.

The energy E and the phase ϕ in a harmonic oscillator are calculated concretely by (2.14) and (2.15).

2.3.5 Behavior of the Proposed Energy/Phase Control in Simulations

To confirm the behavior of the proposed energy/phase control, two simulations are conducted. The first simulation is the case of constant energy command, and the second is the case of step-wise energy command. The dynamics of the robot are modeled as a spring-mass system. The initial position is set as $x(0) = -0.05$ m. The desired constant amplitude of the position is set as 0.1 m. The desired amplitude of the position in step-wise energy command is set as 0.05, 0.10, 0.15, 0.10, 0.05 m.

Fig. 2-5 shows the simulation results of the constant energy command. The amplitude and the period of the position response are constant. The phase response increases from $-\pi$ to π periodically. The energy amplitude follows the constant command. It is confirmed that the energy can be controlled by the proposed method. The force reference rises sharply at the beginning, and is almost zero after the

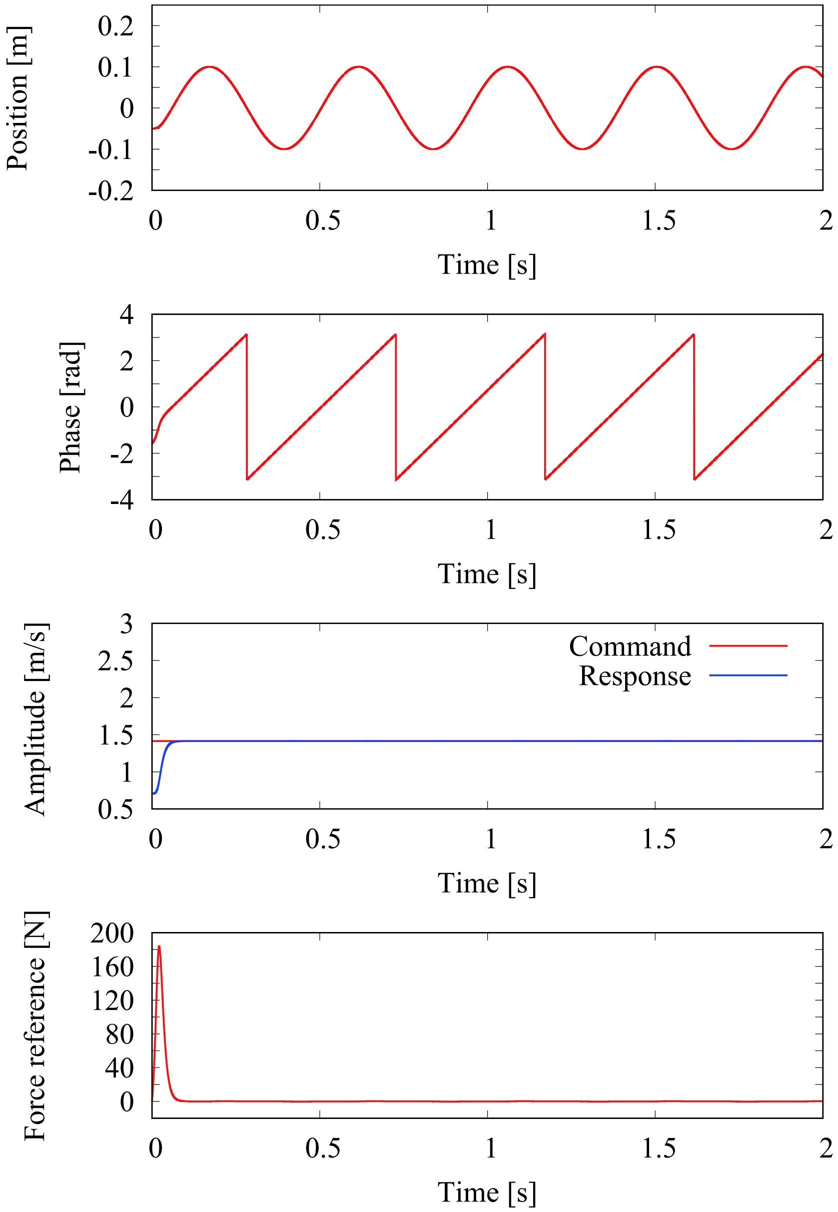

Fig. 2-5: Simulation results of the proposed energy/phase control with constant command.

beginning. While it is necessary to inject energy at the begininng, the energy is preserved and the additional energy is not necessary.

Fig. 2-6 shows the simulation results of the step-wise energy command. The amplitude and the position response changes stepwise. The phase response moves from $-\pi$ to π periodically like the case of the constant energy command. The energy amplitude follows the step-wise energy command. The

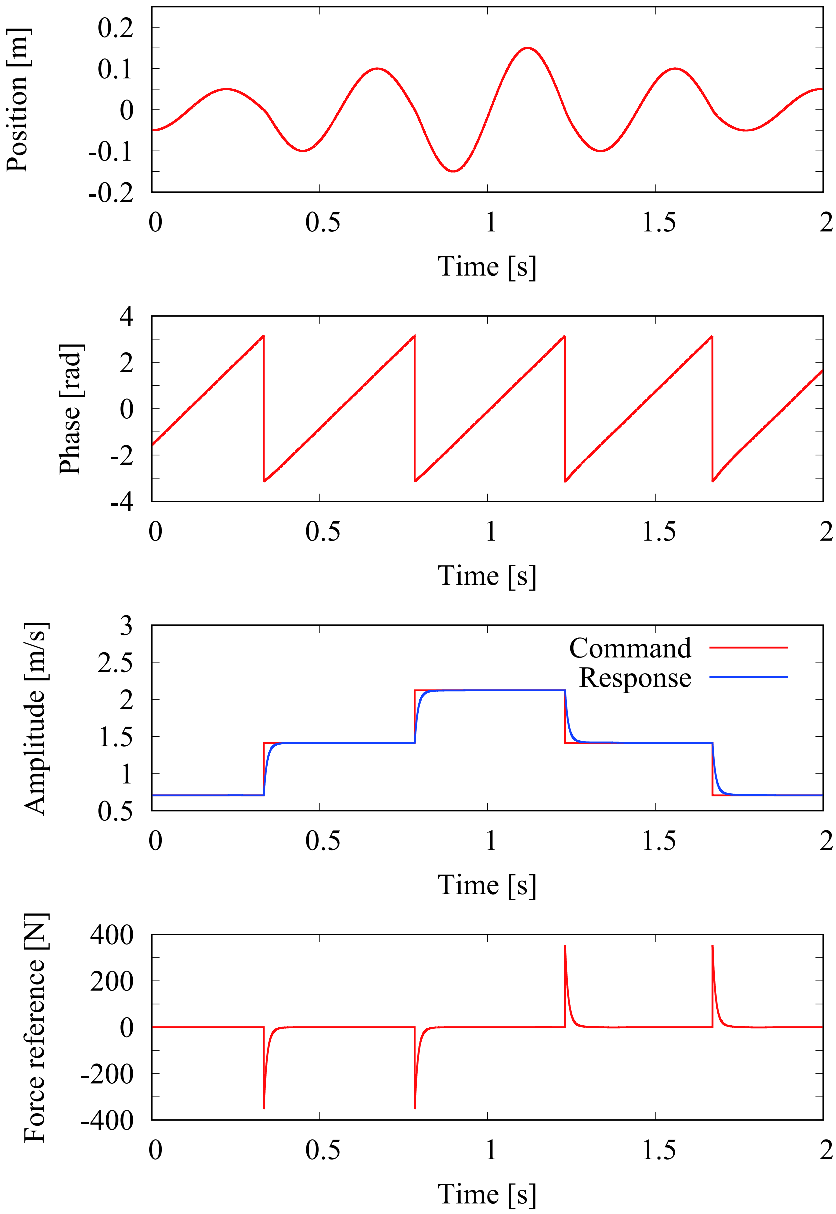

Fig. 2-6: Simulation results of the proposed energy/phase control with step-wise command.

force reference rises sharply at the change point of the energy command.

2.4 Theoretical Analysis

The proposed energy/phase control and the conventional energy control are compared theoretically. The three kinds of analyses are conducted. The first is stability analysis. The second is the analysis of energy efficiency. The third is the analysis of robustness against parameter variation.

2.4.1 Stability Analysis

Stability analysis of the conventional energy control is conducted based on eigenvalue of the state matrix. The motion equation of the conventional energy control is expressed as

$$\ddot{x} - K_{\mathrm{p}}(E^{\mathrm{cmd}} - E)\dot{x} + \omega^2 x = 0 \tag{2.23}$$

$$E = \frac{1}{2}(\dot{x}^2 + \omega^2 x^2). \tag{2.24}$$

Trasforming the motion equation in the form of a state-space equation,

$$\frac{d}{dt}\begin{bmatrix} x \\ \dot{x} \end{bmatrix} = \begin{bmatrix} 0 & 1 \\ -\omega^2 & K_{\mathrm{p}}(E^{cmd} - E) \end{bmatrix}\begin{bmatrix} x \\ \dot{x} \end{bmatrix} \tag{2.25}$$

$$\dot{\boldsymbol{x}} = \boldsymbol{A}\boldsymbol{x} \tag{2.26}$$

is obtained. $\boldsymbol{x}$ is the state vector and $\boldsymbol{A}$ is the state matrix. The eigenvalue λ is derived from the state matrix as

$$|\lambda\boldsymbol{I} - \boldsymbol{A}| = \lambda^2 - K_{\mathrm{p}}(E^{\mathrm{cmd}} - E)\lambda + \omega^2 = 0 \tag{2.27}$$

$$\lambda = \frac{1}{2}\left(K_{\mathrm{p}}(E^{\mathrm{cmd}} - E) \pm \sqrt{K_{\mathrm{p}}^2(E^{\mathrm{cmd}} - E)^2 - 4\omega^2}\right). \tag{2.28}$$

When $E^{\mathrm{cmd}} - E > 0$, the real part of the eigenvalue is positive and the trajectory diverges. When $E^{\mathrm{cmd}} - E = 0$, the real part of the eigenvalue is zero and the trajectory becomes circular. When $E^{\mathrm{cmd}} - E < 0$, the real part of the eigenvalue is negative and the trajectory converges.

Stability analysis of the proposed energy/phase control is considered based on eigenvalue. The motion equation is expressed as

$$\ddot{x} - K_{\mathrm{p}}(A^{\mathrm{cmd}} - A)\cos\phi + \omega^2 x = 0 \tag{2.29}$$

$$A = \sqrt{2E} \tag{2.30}$$

$$E = \frac{1}{2}(\dot{x}^2 + \omega^2 x^2) \tag{2.31}$$

$$\phi = \tan^{-1}(\omega x/\dot{x}). \tag{2.32}$$

Because the equations are nonlinear, linearization is conducted as

$$\dot{x}_1 = f_1(x_1, x_2) \tag{2.33}$$

$$\dot{x}_2 = f_2(x_1, x_2) \tag{2.34}$$

$$\boldsymbol{A} = \begin{bmatrix} \partial f_1/\partial x_1 & \partial f_1/\partial x_2 \\ \partial f_2/\partial x_1 & \partial f_2/\partial x_2 \end{bmatrix}. \tag{2.35}$$

Here, x_1 and x_2 are position and velocity, respectively. The concrete equations are substituted as

$$f_1(x, \dot{x}) = \dot{x} \tag{2.36}$$

$$f_2(x, \dot{x}) = K_\mathrm{p}(A^\mathrm{cmd} - A)\cos\phi - \omega^2 x \tag{2.37}$$

$$\boldsymbol{A} = \begin{bmatrix} 0 & 1 \\ \partial f_2/\partial x_1 & \partial f_2/\partial x_2 \end{bmatrix} \tag{2.38}$$

$$|\lambda \boldsymbol{I} - \boldsymbol{A}| = \lambda^2 - (\partial f_2/\partial x_2)\lambda - \partial f_2/\partial x_1 = 0 \tag{2.39}$$

$$\lambda = \frac{1}{2}\left(\partial f_2/\partial x_2 \pm \sqrt{(\partial f_2/\partial x_2)^2 + 4\partial f_2/\partial x_1}\right). \tag{2.40}$$

$\boldsymbol{I}$ is a unit matrix. From (2.40), the real part of the eigenvalue is equal to $\frac{1}{2}\frac{\partial f_2}{\partial \dot{x}}$. $\frac{\partial f_2}{\partial \dot{x}}$ is concretely calculated as

$$\frac{\partial f_2}{\partial \dot{x}} = -K_\mathrm{p}\left\{\frac{\partial A}{\partial \dot{x}}\cos\phi + (A^\mathrm{cmd} - A)\sin\phi\frac{\partial \phi}{\partial \dot{x}}\right\} \tag{2.41}$$

$$= -K_\mathrm{p}\left\{\frac{\dot{x}}{\sqrt{\dot{x}^2 + \omega^2 x^2}}\cos\phi + (A^\mathrm{cmd} - A)\sin\phi\frac{-\omega x/\dot{x}^2}{1 + (\omega x/\dot{x})^2}\right\}. \tag{2.42}$$

If the sign of (2.42) depends on the error of energy as the conventional energy control, it can be proved that the proposed energy/phase control works properly.

While it is strict and ideal to show the stability from (2.42) theoretically, it is also possible to confirm the stability through numerical calculation. Fig. 2-7 (a) and (b) show the vecotr fields of the conventional energy control and the proposed energy control. The x axis is the velocity and the y axis is the position. In the both figres, the vectors near the origin diverge, and the outside vectors converges to a certain circle. It can be interpreted that the energy increases when $E^\mathrm{cmd} - E > 0$, the energy decreases when $E^\mathrm{cmd} - E < 0$, and the energy is conserved when $E^\mathrm{cmd} - E = 0$.

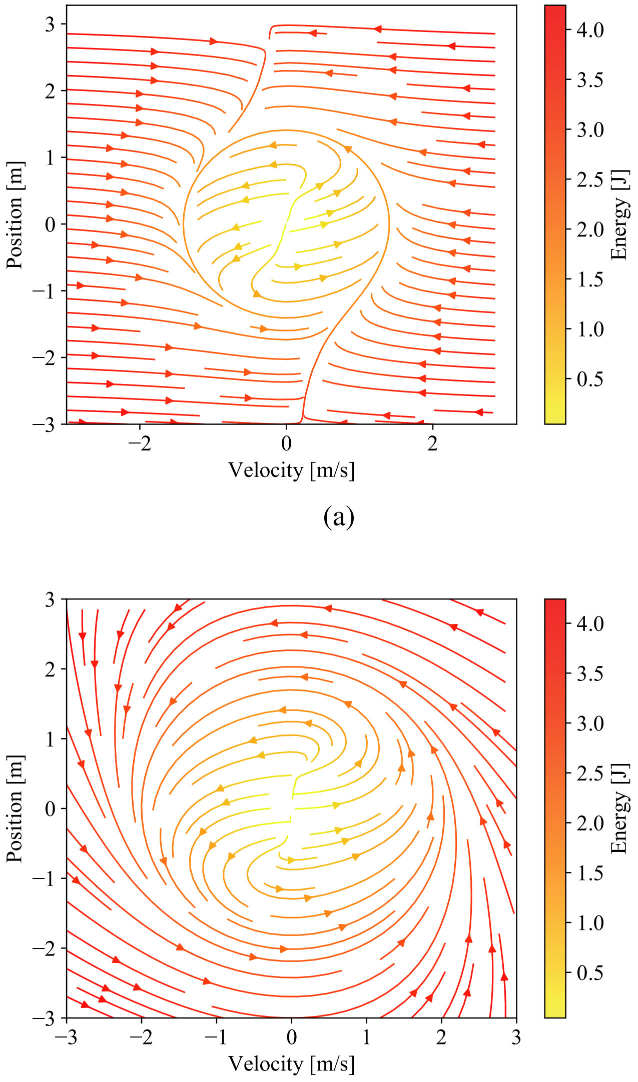

(a)

(b)

Fig. 2-7: Vector field of the convnetional and the proposed method.

2.4.2 Analysis of Energy Efficiency

Force reference in the acceleration dimension $F_{\mathrm{a}}^{\mathrm{ref}}(t)$ and velocity $\dot{x}(t)$ are written in the form of Fourier series expansion as

$$F_{\mathrm{a}}^{\mathrm{ref}}(t) = \sum_{n} F_n \sin(\omega_n t + \phi_n) = \sum_{n} (A_n \cos n\omega_0 t + B_n \sin n\omega_0 t) \tag{2.43}$$

$$\dot{x}(t) = \sum_{n} V_n \sin(\omega_n t + \phi_{vn}) = \sum_{n} (C_n \cos n\omega_0 t + D_n \sin n\omega_0 t). \tag{2.44}$$

Energy increase per cycle ΔE is expressed as

$$\begin{aligned}
\Delta E &= \int_0^T F_{\mathrm{a}}^{\mathrm{ref}}(t)\dot{x}(t)dt && (2.45)\\
&= \int_0^T \sum_n (A_n \cos n\omega_0 t + B_n \sin n\omega_0 t) \sum_n (C_n \cos n\omega_0 t + D_n \sin n\omega_0 t)dt && (2.46)\\
&= \int_0^T \sum_n (A_n C_n \cos^2 n\omega_0 t + B_n D_n \sin^2 n\omega_0 t)dt && (2.47)\\
&= \sum_n (A_n C_n + B_n D_n)\frac{T}{2}. && (2.48)
\end{aligned}$$

T is the cycle period. When $\dot{x}(t) = C_1 \cos \omega_0 t$, the energy increase is transformed using $D_n = 0(\forall n), C_n = 0(n \geq 2)$ as

$$\Delta E = A_1 C_1 \frac{T}{2}. \tag{2.49}$$

Energy efficiency of the conventional energy control and the proposed energy/phase control is compared. The force refernces in the acceleration dimension of the conventional energy control and the proposed energy control $F_{\mathrm{a\,conv}}^{\mathrm{ref}}$ and $F_{\mathrm{a\,prop}}^{\mathrm{ref}}$ are written as

$$\begin{aligned}
F_{\mathrm{a\,conv}}^{\mathrm{ref}} =& K_{\mathrm{p}}\Delta e \dot{x} && (2.50)\\
F_{\mathrm{a\,prop}}^{\mathrm{ref}} =& K_{\mathrm{p}}\Delta e \cos\left(\mathrm{atan}\frac{\omega x}{\dot{x}}\right), && (2.51)
\end{aligned}$$

where Δe is the control error. Energy increase per cycle in the case of the conventional method ΔE_{conv} is calculated as

$$\begin{aligned}
\Delta E_{\mathrm{conv}} &= \int_0^T F_{\mathrm{a\,conv}}^{\mathrm{ref}}(t)\dot{x}(t)dt && (2.52)\\
&= \int_0^T K_{\mathrm{p}}\Delta e \dot{x} \cdot \dot{x}(t)dt && (2.53)\\
&= \int_0^T K_{\mathrm{p}}\Delta e \sum_n (C_n \cos n\omega_0 t + D_n \sin n\omega_0 t) \sum_n (C_n \cos n\omega_0 t + D_n \sin n\omega_0 t)dt && (2.54)\\
&= \int_0^T K_{\mathrm{p}}\Delta e \sum_n (C_n^2 \cos^2 n\omega_0 t + D_n^2 \sin^2 n\omega_0 t)dt && (2.55)\\
&= K_{\mathrm{p}}\Delta e \sum_n (C_n^2 + D_n^2)\frac{T}{2}. && (2.56)
\end{aligned}$$

From (2.56), it is found out that the conventional method oscillates all the components of frequency.

Energy increase per cycle in the case of the proposed method ΔE_{prop} is calculated as

$$\Delta E_{\mathrm{prop}} = \int_0^T F^{\mathrm{ref}}_{\mathrm{a\ prop}}(t)\dot{x}(t)dt \tag{2.57}$$

$$= \int_0^T K_{\mathrm{p}}\Delta e \cos\left(\tan^{-1}\frac{\omega x}{\dot{x}}\right)\cdot\dot{x}(t)dt. \tag{2.58}$$

Here, it is assumed that $\cos\left(\tan^{-1}\frac{\omega x}{\dot{x}}\right)$ extracts the fundamental frequency. The energy increase is transformed as

$$\Delta E_{\mathrm{prop}} = \int_0^T K_{\mathrm{p}}\Delta e(C_1\cos\omega_0 t + D_1\sin\omega_0 t)\sum_n (C_n\cos n\omega_0 t + D_n\sin n\omega_0 t)dt \tag{2.59}$$

$$= K_{\mathrm{p}}\Delta e(C_1^2 + D_1^2)\frac{T}{2}. \tag{2.60}$$

From (2.60), it is found out that the proposed method oscillates only the fundamental component of frequency.

2.4.3 Analysis of Robustness

Dynamic sensitivity is able to analyze the effect of parameter variation in a dynamical system [110–112]. Dynamic sensitivity $\boldsymbol{S}_(t)$ is defined as

$$\boldsymbol{S}(t) := \frac{\partial\boldsymbol{x}(t)}{\partial\boldsymbol{w}}, \tag{2.61}$$

where $\boldsymbol{x}$ is the state vector and $\boldsymbol{w}$ is the parameter vector. Trajectory variation $\Delta\boldsymbol{x}(t)$ is expressed using the dynamic sensitivity $\boldsymbol{S}(t)$ as

$$\Delta\boldsymbol{x}(t) \simeq \boldsymbol{S}(t)\Delta\boldsymbol{w}. \tag{2.62}$$

The dynamic sensitivity $\boldsymbol{S}(t)$ satisfies

$$\frac{d\boldsymbol{S}}{dt} = \frac{\partial\boldsymbol{f}}{\partial\boldsymbol{x}}\boldsymbol{S} + \frac{\partial\boldsymbol{f}}{\partial\boldsymbol{w}}. \tag{2.63}$$

The determinant of $\frac{\partial\boldsymbol{f}}{\partial\boldsymbol{x}}$ is induced as

$$\left|\frac{\partial\boldsymbol{f}}{\partial\boldsymbol{x}}\right| = \left|\begin{bmatrix} 0 & 1 \\ \frac{\partial f_2}{\partial x} & \frac{\partial f_2}{\partial\dot{x}}\end{bmatrix}\right| \tag{2.64}$$

$$= \frac{\partial f_2}{\partial x}. \tag{2.65}$$

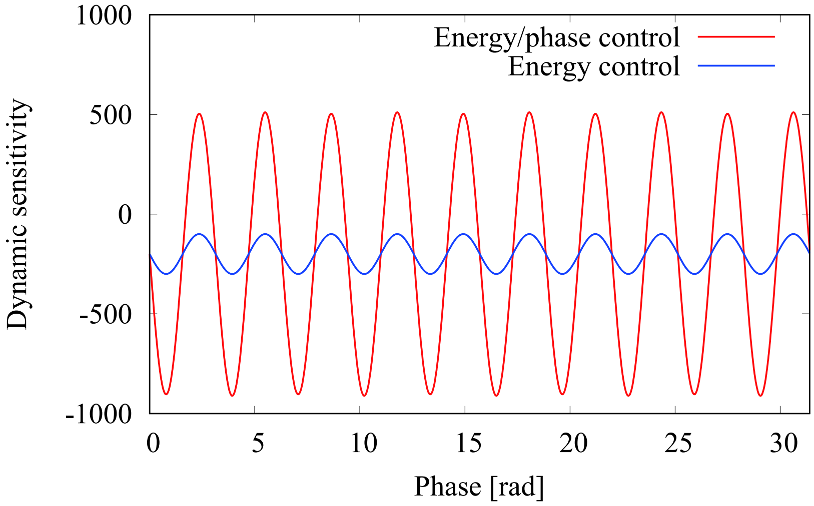

Fig. 2-8: Comparison of the dynamic sensitivity.

In the case of the conventional energy control, the dynamic sensitivity is derived as

$$\frac{\partial f_2}{\partial x} = \frac{\partial}{\partial x}\left[K_\mathrm{p}\left\{E^\mathrm{cmd} - \frac{1}{2}(\dot{x}^2 + \omega^2 x^2)\right\}\dot{x} - \omega^2 x\right] \tag{2.66}$$

$$= -\omega - K_\mathrm{p}\omega^2 x\dot{x}. \tag{2.67}$$

In the case of the proposed energy/phase control, the dynamic sensitivity is derived as

$$\frac{\partial f_2}{\partial x} = \frac{\partial}{\partial x}\left[K_\mathrm{p}\left\{A^\mathrm{cmd} - \sqrt{\dot{x}^2 + \omega^2 x^2}\right\}\cos\left(\tan^{-1}\frac{\omega x}{\dot{x}}\right) - \omega^2 x\right] \tag{2.68}$$

$$= -\omega^2 - \frac{K_\mathrm{p}\omega^2 x}{\sqrt{\dot{x}^2 + \omega^2 x^2}}\cos\left(\tan^{-1}\frac{\omega x}{\dot{x}}\right) + K_\mathrm{p}\sqrt{\dot{x}^2 + \omega^2 x^2}\sin\left(\tan^{-1}\frac{\omega x}{\dot{x}}\right)\frac{x/\dot{x}}{1 + (\omega x/\dot{x})^2}. \tag{2.69}$$

As a reference trajectory, $x = A\sin\omega t$ and $\dot{x} = \omega A\cos\omega t$, or the resonance of the plant is assumed. Under the reference trajectory, the dynamic sensitivity is calculated and compared as Fig. 2-8. In Fig. 2-8, the maximum value of the dynamic sensitivity in the proposed method is higher than the conventional method. It can be said that the conventional method is more robust to the small change of the parameter.

2.5 Comparative Simulations

The validity of the proposed energy/phase control is confirmed through simulations comparing with conventional methods. It is ideal to reduce the control error, the robust variation, and the energy consumption. There is a trade-off in the design of the control system as Fig. 2-9. While increasing gains

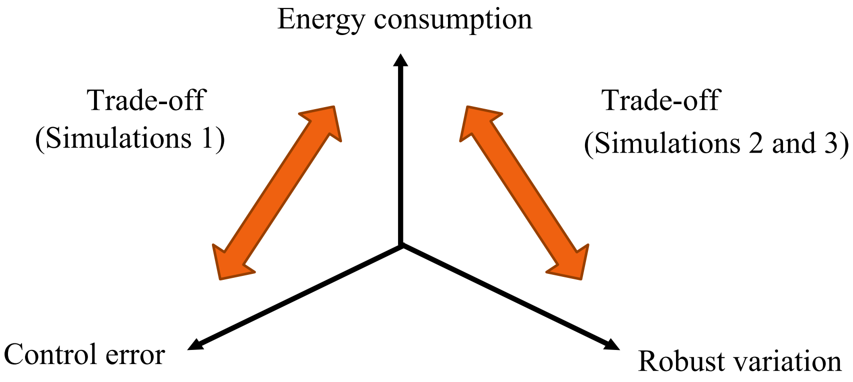

Fig. 2-9: Three axes of the numerical analysis and the gain design.

Table 2.1: Parameters of the comparative simulations.

Description	Parameter	Value
Body mass	M	5.0 kg
Stiffness of the leg spring	k	1000 N/m
Sampling time of control	T_s	0.100 ms
Nominal torque constant	K_tn	0.091 N/A
Maximum force reference	u_max	500 N

leads to improvement of control performance, increasing gains leads to an increase in energy consumption. While it is possible to increase robustness against the parameter variation, increasing robustness leads to an increase in energy consumption. This section deals with the determination of a control method and its gains to satisfy the specifications.

Three types of simulations are conducted as Fig. 2-9. Simulations 2-1 focus on the trade-off between the control error and the energy consumption. Each control method is compared in terms of the control error and the energy consumption. Simulations 2-2 focus on the trade-off between the robustness and the energy consumption. As for the robustness, a parameter (concretely the stiffness of the plant) is varied, and the variation of the trajectory is evaluated. Simulations 2-3 deal with increasing the robustness by adding a disturbance observer.

The simulation parameters are shown in Table 2.1.

2.5.1 Simulations 2-1: Energy Consumption versus Control Error

Firstly, the trade-off of the control error and the energy consumption is visualized in the case of the respective control method (the energy/phase control, the energy control, and the position contorl). The

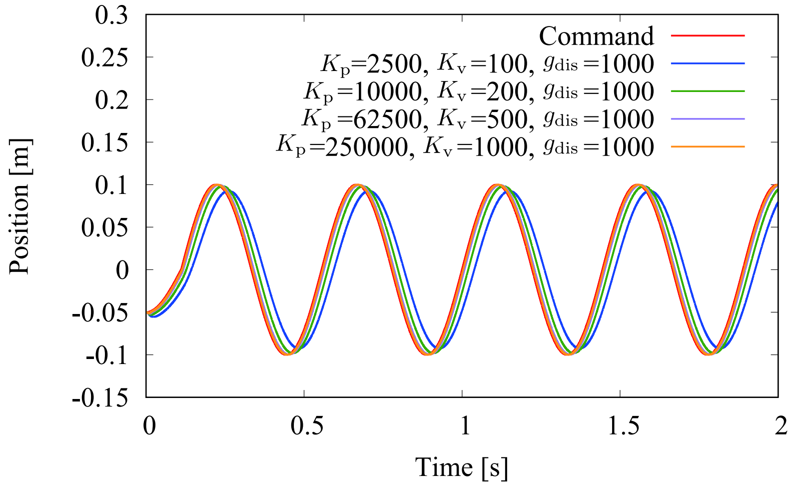

Fig. 2-10: Position command and response of the position control in each gain.

indices of the control error and the energy consumption are defined as follows.

The indices of the control error are root squared control error of amplitude and period RMSE_A^{con}, RMSE_T^{con}. They are defined as

$$\mathrm{RMSE}_A^{\mathrm{con}} = \sqrt{\sum_{i=1}^{n} (A_{\mathrm{mp}}^{\mathrm{des}} - A_{\mathrm{mp}i})^2 / n} \tag{2.70}$$

$$\mathrm{RMSE}_T^{\mathrm{con}} = \sqrt{\sum_{i=1}^{n} (T^{\mathrm{des}} - T_i)^2 / n} \tag{2.71}$$

where $A_{\mathrm{mp}i}$ is the amplitude of the i th peak, and $A_{\mathrm{mp}i}^{\mathrm{des}}$ is the desired amplitude of of the i th peak. n is the number of the peaks in the simulation periods. T_i is the period from the i th peak to the $(i+1)$ th peak, and T_i^{des} is the desired period from the i th to the $(i+1)$ th peak. The total error is defined by averaging the two RMSEs in terms of nondimensional rate as

$$\mathrm{TotalError} = \left(\frac{\mathrm{RMSE}_A^{\mathrm{con}}}{A_{\mathrm{mp}}^{\mathrm{des}}} + \frac{\mathrm{RMSE}_T^{\mathrm{con}}}{T^{\mathrm{des}}} \right) / 2. \tag{2.72}$$

As the index of efficiency, energy consumption is adopted. The energy consumption EC is calculated as

$$\mathrm{EC} = \int F^{\mathrm{ref}} \dot{x} dt, \tag{2.73}$$

where F^{ref} is the force reference, and $\dot{x}$ is the velocity of the body mass.

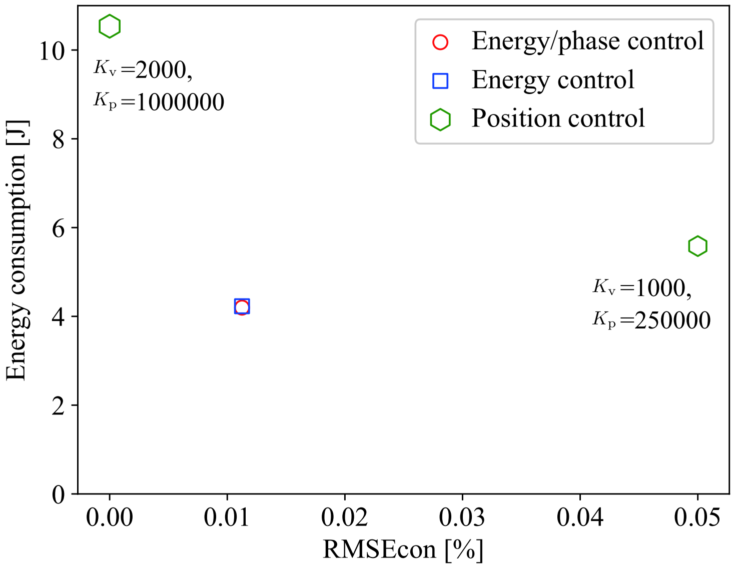

Fig. 2-11: Summary results of simulations 2-1: the best results of the respective methods.

The proposed energy/phase control is compared with the conventional energy control and position control in the case of a simple P controller. The initial position is set as -0.05 m, and the initial velocity is zero. From the initial condition, each control is implemented. The amplitude command A^{cmd} is set as 0.10 m. Simulations 2-1 change the the controller gains. In the case of the energy-based controls and the velocity control, the proportional gain is varied. In the case of the position control, the position gain is set as $K_{\mathrm{p}} = K_{\mathrm{v}}^2/4$, where K_{v} is the velocity gain. Due to the response in Fig. 2-10, it is necessary to set the high gain in the position control for tracking the command. The patterns of the velocity gain K_{v} are 200, 1000, and 2000. g_{dis} in Fig. 2-10 is the cut-off frequency of the DOB. The control error and the energy consumption are evaluated in the simulations. The control error are calculated using the amplitude, the period, and (2.72). The amplitude and the period are calculated from the peak values. The peak values are detected from the time-series position response. The energy consumption is calculated using (2.73).

Fig. 2-11 and Table 2-11 show the comparison in terms of the control error and the energy consumption. Although the position control attains the lowest control error as TotalError=0.0000 % when $K_{\mathrm{v}} = 2000$, the energy consumption is the highest as 10.536 J. The control errors of the energy/phase control and the energy control are equal to 0.0113 %. The energy consumption of the energy/phase control and the energy control is around 4.2 J. While the position control has an advantage in terms of the control error, the energy-based controls have an advantage in terms of the energy consumption. The

Table 2.2: Results of simulations 2-1: energy consumption and control error.

Controller		Control error	Energy consumption
Control method	Gain	$\mathrm{TotalError}$ [%]	EC [J]
Energy/phase control	$K_{\mathrm{p}} = 50$	0.0113	4.197
	$K_{\mathrm{p}} = 100$	0.0113	4.235
	$K_{\mathrm{p}} = 200$	0.0113	4.251
Energy control	$K_{\mathrm{p}} = 50$	0.0113	4.228
	$K_{\mathrm{p}} = 100$	0.0113	4.244
	$K_{\mathrm{p}} = 200$	0.0113	4.256
Position control with DOB	$K_{\mathrm{v}} = 200$	1.0000	5.545
	$K_{\mathrm{v}} = 1000$	0.0500	5.583
	$K_{\mathrm{v}} = 2000$	0.0000	10.536

proposed energy/phase control has the lowest energy consumption compared to the energy control and the position control.

2.5.2 Simulations 2-2: Energy Consumption versus Robustness when there are Parameter Variation

In simulaitons 2-2, the control methods are compared in terms of the robustness when there is parameter variation. It is desirable to realize the same response whether the parameters have variation. In the simulations, the stiffness of the spring is varied ± 10 %.

The indices of robustness are root mean squared error of amplitude variation and period variation with parameter variation $\mathrm{RMSE}_A^{\mathrm{rob}}, \mathrm{RMSE}_T^{\mathrm{rob}}$. They are defined as

$$\mathrm{RMSE}_A^{\mathrm{rob}} = \sqrt{\frac{(\overline{A_{\mathrm{mp}}}(k+\Delta k) - \overline{A_{\mathrm{mp}}}(k))^2 + (\overline{A_{\mathrm{mp}}}(k-\Delta k) - \overline{A_{\mathrm{mp}}}(k))^2}{2}} \tag{2.74}$$

$$\mathrm{RMSE}_T^{\mathrm{rob}} = \sqrt{\frac{(\overline{T}(k+\Delta k) - \overline{T}(k))^2 + (\overline{T}(k-\Delta k) - \overline{T}(k))^2}{2}} \tag{2.75}$$

where $\overline{A_{\mathrm{mp}}}(k)$ is the average of the position amplitude with the stiffness k. $\overline{T}(k)$ is the average of the vibration period with the stiffness k. $k \pm \Delta k$ is the stiffness with paramter variation. The variation is set as ± 10 %. The total robustness is defined by averaging the two RMSEs in terms of nondimensional rate as

$$\mathrm{TotalRobustness} = \left(\frac{\mathrm{RMSE}_A^{\mathrm{rob}}}{A_{\mathrm{mp}}^{\mathrm{des}}} + \frac{\mathrm{RMSE}_T^{\mathrm{rob}}}{T^{\mathrm{des}}} \right) /2. \tag{2.76}$$

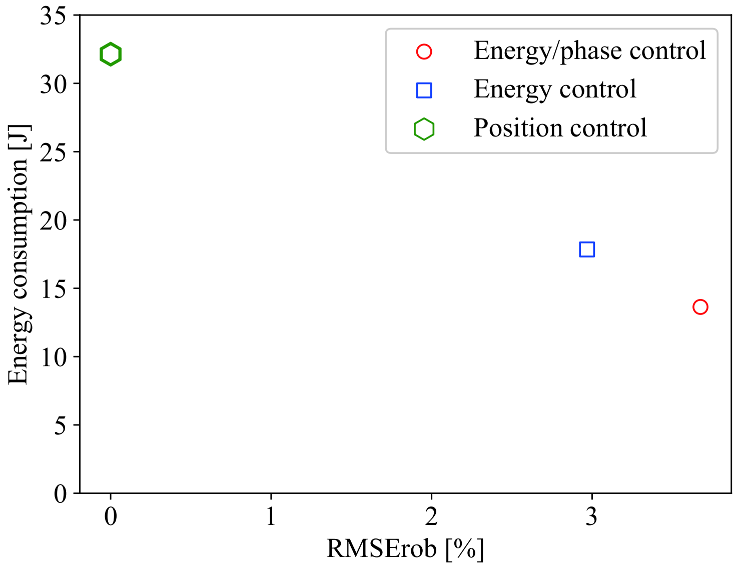

Fig. 2-12: Summary results of simulations 2-2: the best results of the respective methods.

Table 2.3: Results of simulations 2-2: energy consumption and robustness.

Controller Control method	 Gain	Robustness TotalRobustness [%]	Energy consumption EC [J]
Energy/phase control	$K_\mathrm{p} = 50$	3.6752	13.635
	$K_\mathrm{p} = 100$	3.0007	17.895
	$K_\mathrm{p} = 200$	2.3326	20.800
Energy control	$K_\mathrm{p} = 50$	2.9683	17.845
	$K_\mathrm{p} = 100$	2.3267	20.770
	$K_\mathrm{p} = 200$	1.7894	22.630
Position control with DOB	$K_\mathrm{v} = 200$	0.0000	26.050
	$K_\mathrm{v} = 1000$	0.0000	27.155
	$K_\mathrm{v} = 2000$	0.0000	32.135

The energy consumption EC in simulation 2-2 is induced as the average of the EC when the stiffness is $+10$ % and -10%.

Fig. 2-12 shows the summary results of simulations 2-2 in terms of the energy consumption and the robustness. The results in the case of the higher gains are also shown in Table 2.3. The trade-off of the energy consumption and the robustness is visualized from Fig. 2-12. The position control attains that the robust variation is equal to 0.000 % while the energy consumption is the highest. The energy/phase control attains the lowest energy consumption while the robust variation is the highest.

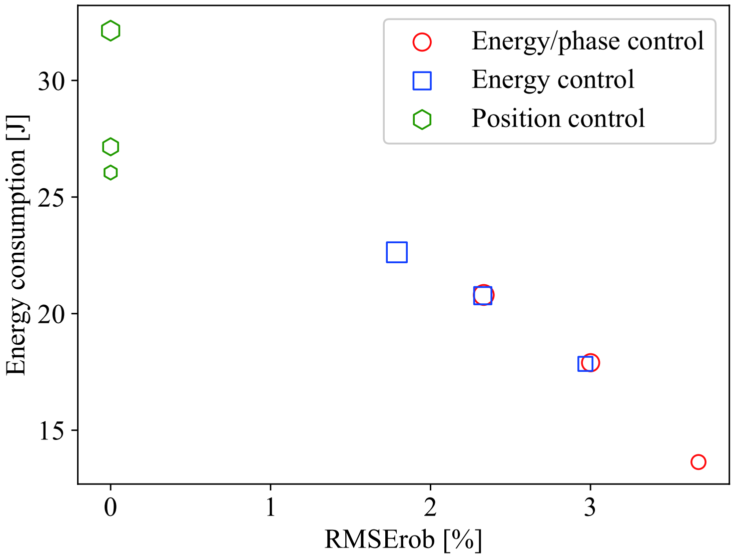

Fig. 2-13: Results of simulations 2-2 when the gain increases (the size of the marker corresponds to the magnitide of the gain in Table 2.3).

Table 2.4: Results of simulations 2-3: addition of DOB to energy/phase control.

DOB Cut-off frequency	Robustness TotalRobustness [%]	Energy consumption EC [J]
$g_{\text{dis}} = 0$ (without DOB)	3.6752	13.635
$g_{\text{dis}} = 50$	1.1645	39.7750
$g_{\text{dis}} = 100$	0.5238	26.4600
$g_{\text{dis}} = 200$	0.2105	27.6000

The energy control is located between the position control and the energy/phase control. These results are natural and consistent with the theoretical analysis. The position control is a robust control system by a disturbance observer. The theoretical analysis showed that the energy control is more robust but consumes more energy than the energy/phase control. The results in the case of the higher gains (Table 2.3) are also visualized as Fig. 2-13. The tendency of Fig. 2-12 is also consistent in Fig. 2-13.

2.5.3 Simulations 2-3: Addition of a Disturbance Observer for Higher Robustness

For improving the robustness of the proposed energy/phase control, Simulations 2-3 deals with the addition of a disturbance observer. Several cut-off frequencies of the disturbance observer are simulated. The energy consumption and the robustness are calculated as simulations 2-2.

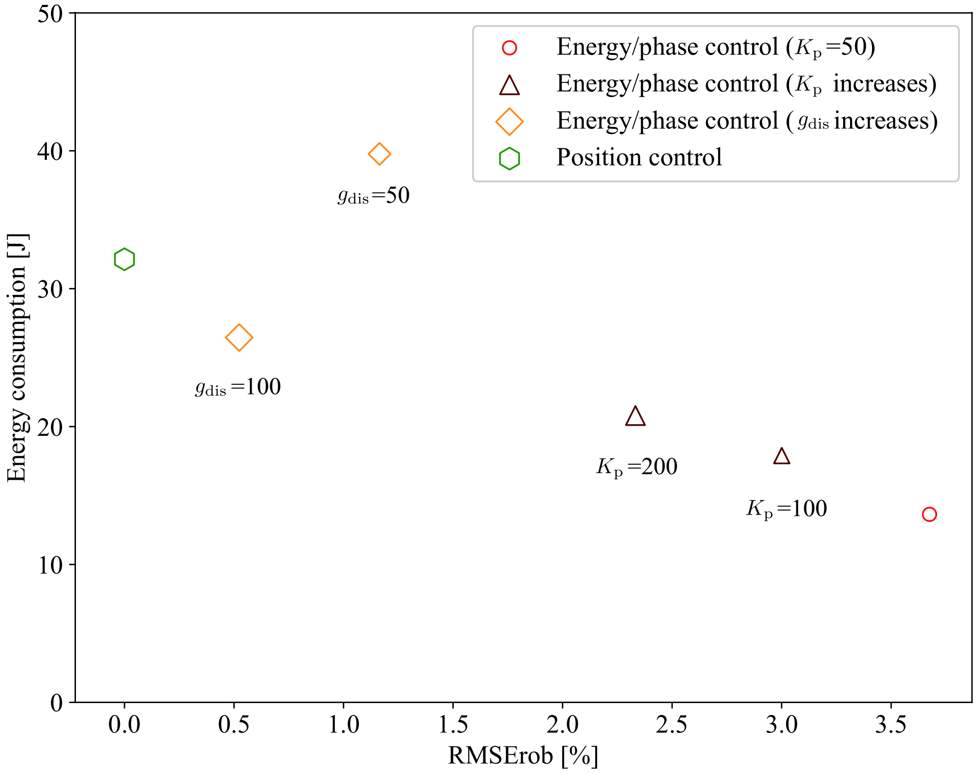

Fig. 2-14: Summary results of simulations 2-3: increasing the P gain and the cut-off frequency of the DOB.

The simulation results are shown in Fig. 2-14 and Table 2.4. Fig. 2-14 compares the proposed energy/phase control with a DOB and the position control with a DOB. By adding a disurbance observer, the robustness is greatly improved while the energy consumption is increased. It became possible to realize the performance between the position control and the energy-based control (without DOB).

2.6 Additional Simulations Considering Impact and Damping

In the additional simulations, impact force and damping force are considered.

Firstly, the simulations with impact force are conducted. Assuming the impact at the landing of hopping motion, the impact force is applied when the body goes through zero from the positive to the negative. As the impact force, five times the force of the robot weight is applied in 0.05 s. The simulation results including impact are shown in Fig. 2-15. Although the control error of the energy is large when the impact force is being applied, the errors are converged to zero after the impact. In the case of hopping motions, it is sufficient that the errors are converged to zero at the timing of lift off. The convergence

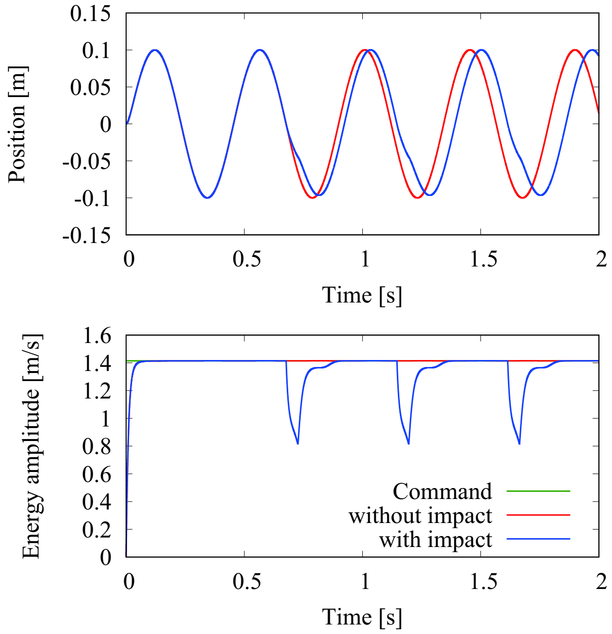

Fig. 2-15: Results of the energy/phase control simulations for a harmonic oscillator with impact.

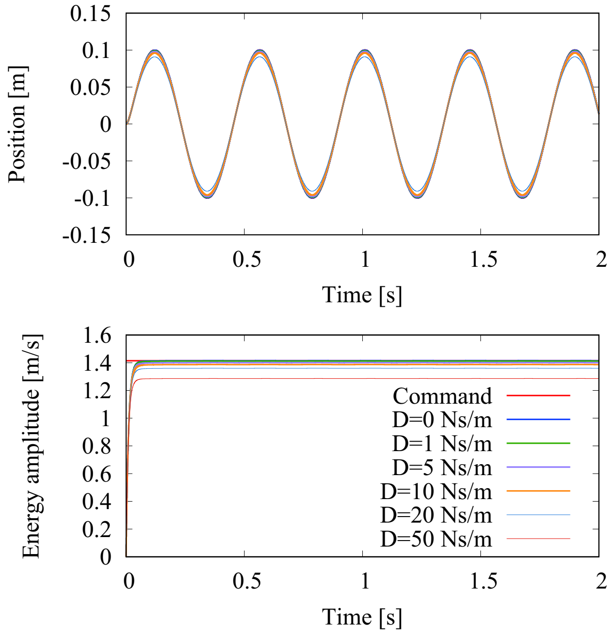

Fig. 2-16: Results of the energy/phase control simulations for a harmonic oscillator with damper.

speed is determined by the energy P control gain. The P gain can be tuned considering that the P gain corresponds to the time constant of the energy control.

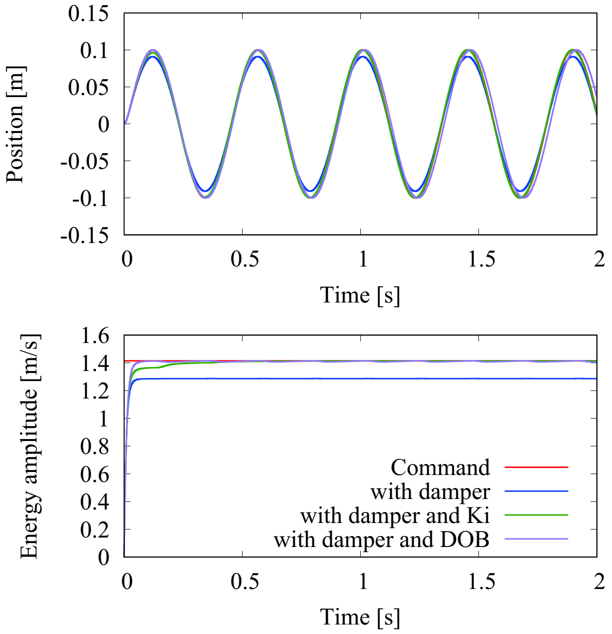

Fig. 2-17: Results of the energy/phase control simulations for a harmonic oscillator with damper and the compensation.

Next, the simulations with damping force are conducted. The tested patterns of the damping coefficient are 1, 5, 10, 20, 50 Ns/m. The results of the damping simulations are shown in Fig. 2-16. In the position responses, the amplitude decreases in response to the magnitude of the damping coefficient while the phases are equal. In the energy responses, the damping causes the steady-state error. To the steady-state error of the energy, two solutions are considered and tested: a PI controller and a disturbance observer. Fig. 2-17 shows the results of the solutions. It is found that the errors approach zero in each solution.

2.7 Summary

This chapter dealt with the energy/phase control as a mechanical oscillator. The conventional energy control and the proposed energy/phase control are explained. The induction of the energy/phase control is also described. As the structure, the energy control is implemented under the phase control. It was confirmed that the energy/phase control works properly through the simulations. The conventional energy control and the proposed energy/phase control were compared through the theoretical analysis and the numerical analysis. It was confirmed that the advantage of the energy/phase control is low energy consumption. It is also possible to increase the robustness of the energy/phase control by introducing a disturbance observer in return for the energy consumption. In addition, additional simulations considering impact and damping were also conducted. It was shown that the energy P controller recovers the control error after the impact, and that the damping can be compensated by an energy PI controller or a disturbance observer.

Chapter 3

Nominalized Legged System for Energy/Phase Control

3.1 Introduction

This chapter deals with mechanism and control for nominalizing the dynamics. The mechanism is designed for realizing similar dynamics to the desired. Linearization control of a multi-degree-of-freedom (MDOF) robot is introduced for compensating the residual error of the dynamics. Several types of disturbance observers are compared. Based on the system consisting of the mechanism and the control, the energy/phase control is implemented. Numerical and analytical comparisons are conducted.

Section 3.2 presents the design philosophy of the legged mechanism. Section 3.3 describes the model of the robot: definition of coordinate, kinematics, and dynamics. Section 3.4 introduces DOBs for an MDOF robot. Joint-space observer and workspace observer are introduced. Section 3.5 deals with comparative simulations. The DOBs are compared under the legged robot and the energy/phase control. The evaluation indices are the same as the simulations in Chapter 2: the control error, the energy consumption, and the robustness.

3.2 Design Philosophy of Leged Mechanism

The desired dynamics are two patterns: a mass system and a spring-mass system. A mass system has a mass point on the body, and has a no-weight leg. The desired spring-mass system is composed of a mass point and a no-weight linear springy leg. From these background, two analyses are conducted

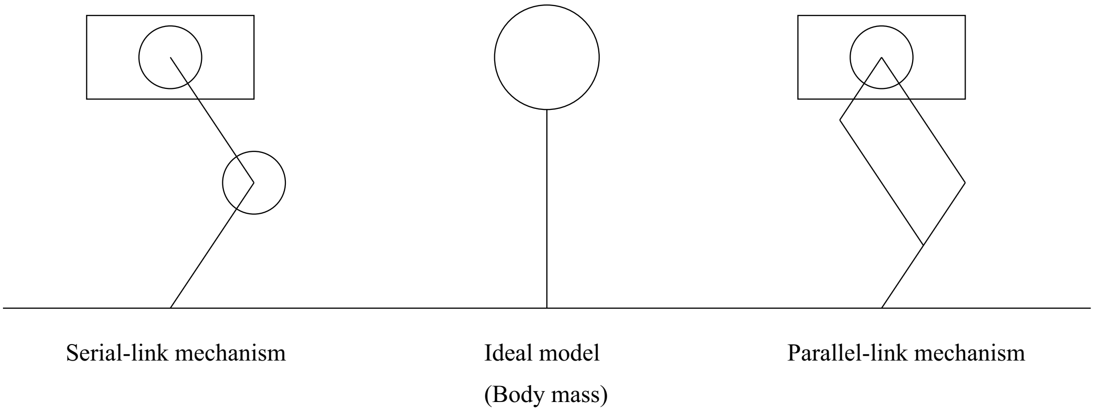

Fig. 3-1: Illustration of the leg robot: serial-link mechanism and parallel-link mechanism.

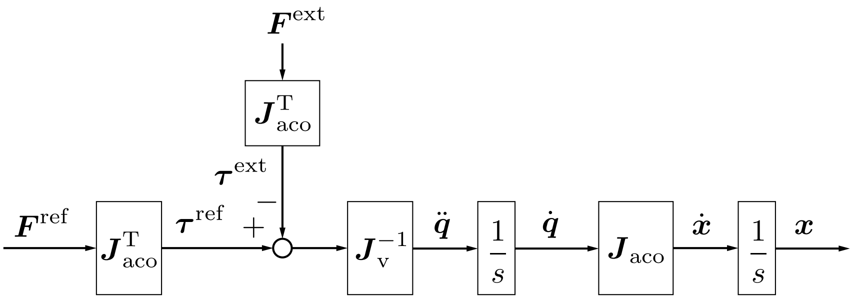

Fig. 3-2: Block diagram of the equivalent mass.

for the desired dynamics. The first analysis evaluates which mechanism is closer to the ideal mass system. Concretely, the serial-link mechanism and the parallel-link mechanism are compared. The second analysis evaluates which spring realizes the closer dynamics to the ideal spring-mass system. Concretely, a rotary spring and a linear spring are compared analytically.

3.2.1 Design of a Mass System: Serial Link Mechanism versus Parallel Link Mechanism

In order to make the dynamics of the legged robot similar to the ideal body mass model, comparative analyses are conducted. Concretely, mass variation in response to posture change is analyzed in the cases of the serial-link mechanism and the parallel-link mechanism. Illustrations of the serial-link and the parallel-link leg robots are shown in Fig. 3-1. The serial link has one actuator on the hip and the other on the knee. The two actuators of the parallel link are concentrated on the hip. The actuators are heavy because they include the motors and the gears. The concerete mass distribution is assumed as Tables 3.1 and 3.2.

Table 3.1: Mass parameters of the parallel link mechanism.

Description	Parameter	Value
Total mass	m	6.50 kg
Body mass in parallel link	m_{b}	5.20 kg
Mass of bar 1 in parallel link	m_1	0.35 kg
Mass of bar 2 in parallel link	m_2	0.35 kg
Mass of bar 3 in parallel link	m_3	0.25 kg
Mass of bar 4 in parallel link	m_4	0.35 kg

Table 3.2: Mass parameters of the serial link mechanism.

Description	Parameter	Value
Total mass	m	6.50 kg
Body mass in serial link	m_{bs}	4.00 kg
Mass of knee joint in serial link	m_{k}	1.80 kg
Mass of bar 1 in serial link	m_{1s}	0.35 kg
Mass of bar 2 in serial link	m_{2s}	0.35 kg

In the ideal body mass model, the inertia is constant regardless of the posture, and has no interference term. This is embodied as that the diagonal elements of the inertia matrix are constant, and the non-diagonal elements are zero. Each inertia matrix can be calculated from the block diagram of Fig. 3-2. $\boldsymbol{F}^{\mathrm{ref}}$ and $\boldsymbol{F}^{ext}$ are the forece reference and the external force. $\boldsymbol{\tau}^{\mathrm{ref}}$ and $\boldsymbol{\tau}^{\mathrm{ext}}$ are the torque reference and the external torque. $\boldsymbol{J}_{\mathrm{aco}}$ is the Jacobian matrix and $\boldsymbol{J}_{\mathrm{aco}}^{\mathrm{T}}$ is the transpose of the Jacobian matrix. $\boldsymbol{J}_{\mathrm{v}}^{-1}$ is the inverse of the inertia matrix in the joint space. $\boldsymbol{q}, \dot{\boldsymbol{q}}$ and $\ddot{\boldsymbol{q}}$ are the joint angle vector, the angular velocity vector, and the acceleration vector in the joint space. $\boldsymbol{x}$ and $\dot{\boldsymbol{x}}$ are the position vector and the velocity vector in the workspace. s is the Laplace operator. The concrete equations of $\boldsymbol{J}_{\mathrm{aco}}$ and $\boldsymbol{J}_{\mathrm{v}}$ are different between the serial link and the parallel link.

From Fig. 3-2, the matrix of the transfer functions from the force reference to the body position is induced as

$$\boldsymbol{x}(\boldsymbol{F}^{\mathrm{ref}})^{-1} = \boldsymbol{s}^{-1} J_{\mathrm{aco}} \boldsymbol{s}^{-1} \boldsymbol{J}_{\mathrm{v}}^{-1} \boldsymbol{J}_{\mathrm{aco}}^{T}, \tag{3.1}$$

where $\boldsymbol{s}^{-1} = \begin{bmatrix} \frac{1}{s} & 0 \\ 0 & \frac{1}{s} \end{bmatrix}$. The equivalent mass $\boldsymbol{M}_{\mathrm{eq}}$ in the workspace is derived as the inverse matrix of the transfer functions from the force reference to the body acceleration as

$$\boldsymbol{M}_{\mathrm{eq}} = (\ddot{\boldsymbol{x}}(\boldsymbol{F}^{\mathrm{ref}})^{-1})^{-1} = \boldsymbol{J}_{\mathrm{aco}}^{-T} \boldsymbol{J}_{\mathrm{v}} J_{\mathrm{aco}}^{-1}. \tag{3.2}$$

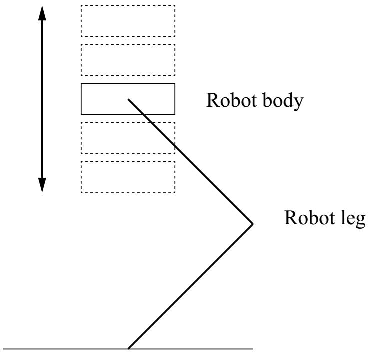

Fig. 3-3: Illustration of the squat simulation.

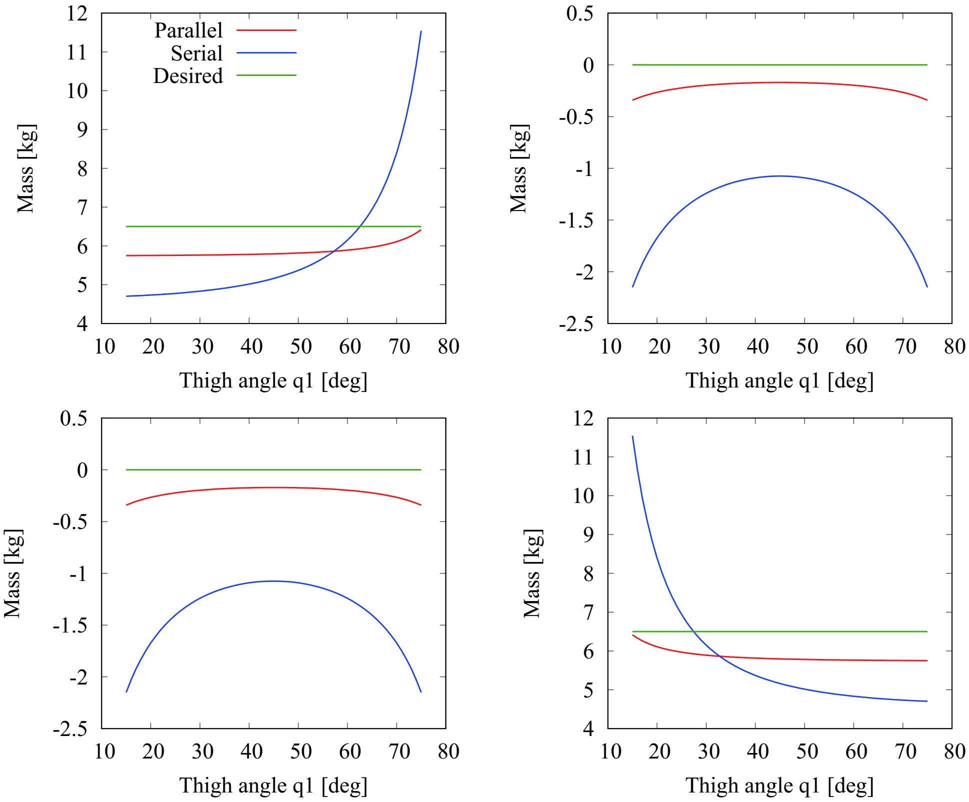

Fig. 3-4: Analysis of mass matrices (Parallel link, serial link, and desired value).

The inertia matrix $\boldsymbol{J}_{\mathrm{v}}$ is different depending on whether the mechanism is serial or parallel. This leads to the different characteristics of the equivalent mass.

The analytical results of each equivalent mass matrix $\boldsymbol{M}_{\mathrm{eq}}$ are compared. The mass values in response to the angle of the leg bending are plotted. The posture is assumed as that the center of the body is on the vertical line from the tiptoe as Fig. 3-3. The analytical results are shown in Fig. 3-4. The 2 × 2

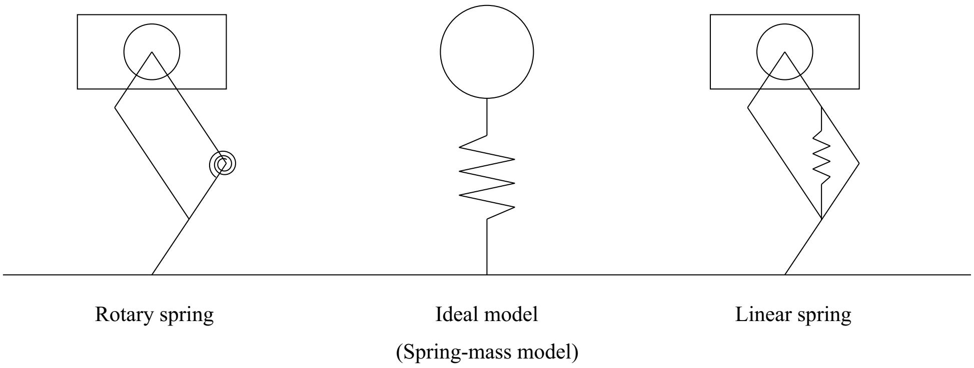

Fig. 3-5: Illustration of the parallel-link leg robot with spring: a rotary spring and a linear spring.

figures correspond to the 2 × 2 inertia matrices. In each figure, the mass in response to the thigh angle is plotted. The three patterns of mechanics are compared: the parallel link, the serial link, and the ideal model. In the ideal model, the diagonal elements are constant, and the non-diagonal elements are zero. In the results of the parallel link, the respective elements vary less than the case of the serial link. The non-diagonal elements of the parallel link are nearer to zero than the serial link. From these results, it is concluded that the parallel link is more adequate to make the robot dynamics similar to the ideal body mass model.

3.2.2 Design of a Spring-Mass System: Rotary Spring versus Linear Spring in the Parallel Link Leg Robot

The parallel-link leg robots with a rotary spring and with a linear spring are shown in Fig. 3-5. While a legged robot with a rotary spring is popular [51, 84], the proposed leg mechanism employs a linear spring so that the dynamics are closer to the ideal spring-mass model. The two types of mechanisms are compared using bode plots.

Fig. 3-6 (a) shows the block diagram of the spring-mass model with the rotary spring. $\boldsymbol{K}_{\mathrm{R}}$ is the stiffness matrix and $\boldsymbol{q}_0$ is the angle vector of the natural length. $\boldsymbol{\tau}^{\mathrm{sp}}$ is the vector of the spring torque. By transforming the block diagram, the transfer function matrix from the force reference to the position is induced. Fig. 3-6 (b) shows the block diagram of the spring-mass model with the linear spring. $\boldsymbol{p}, \dot{\boldsymbol{p}}$ are the position and the velocity in the polar coordinate. $\boldsymbol{J}_{\mathrm{acp}}$ shows the Jacobian matrix in the polar coordinate. The elastic force of the leg spring is proportional to the displacement of the length between the body center and the tiptoe. $\boldsymbol{K}_{\mathrm{sp}}$ is the stiffness matrix and $\boldsymbol{F}^{\mathrm{sp}}$ is the vector of the elastic force. The transfer function matrix is induced from the block diagram of Fig. 3-6 (b).

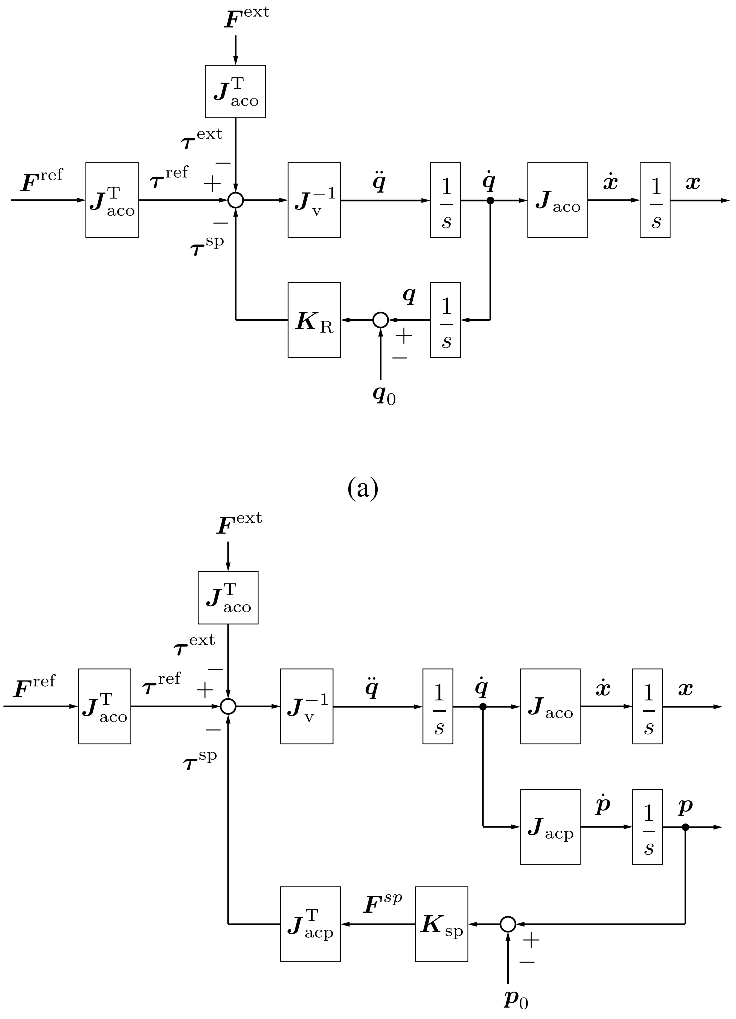

(a)

(b)

Fig. 3-6: Block diagram of the parallel-link leg robot with spring: (a) rotary spring, (b) linear spring.

The bode diagrams of the transfer function with the rotary spring are shown in Fig. 3-7 (a). The cases of $q_1 = 30, 40, 50$ deg are plotted. The most important characteristics are the responses from the vertical force reference to the vertical position, which corresponds to the second-row, second-column figure. The desired response is the purple line. The resonance point of each curve is different. In the case of the rotary spring, the resonance point moves in response to the posture. The bode diagrams of the linear spring are shown in Fig. 3-7 (b). The desired line and the other response lines almost overlap. In the case of the linear spring, the resonance point is almost constant regardless of the change of the posture.

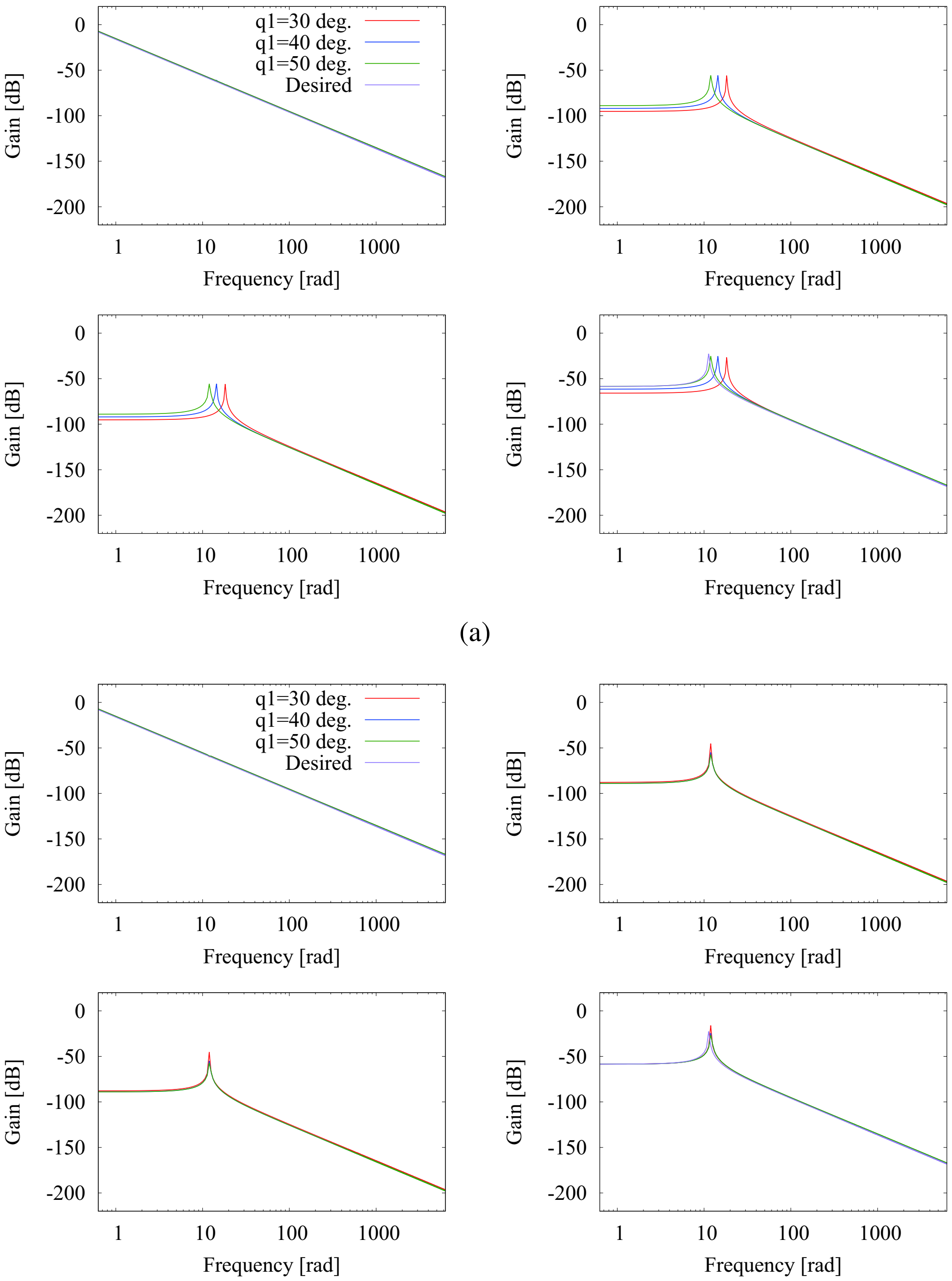

(a)

(b)

Fig. 3-7: Analysis of spring-mass characteristic with the springs: (a) rotary spring, (b) linear spring.

From these results, it is concluded that the linear spring is superior for the legged robot.

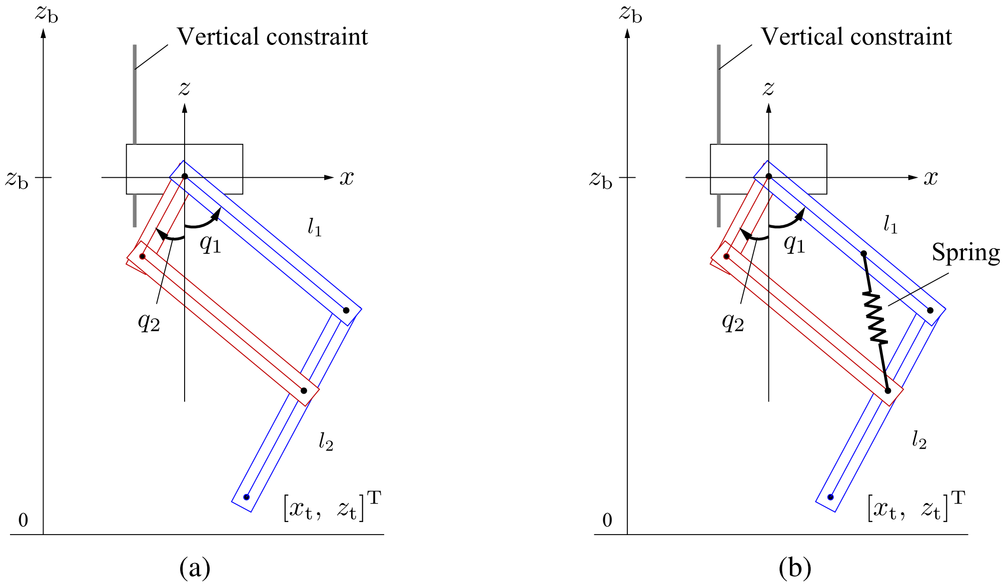

Fig. 3-8: Illustrations of the leg robot: (a) without spring, (b) with spring.

3.3 Mechanical Model

This section introduces the 2-DOF parallel link robot with the linear spring in detail.

This research employs an articulated one-leg robot which can be approximated to a spring-mass model as Figs. 3-8 and 3-9. In Fig. 3-8, z_b is the vertical body position, q_1, q_2 are the angles of the geared motors, l_1, l_2 are the lengths of the leg bars, and $[x_\mathrm{t}, z_\mathrm{t}]$ is the position vector of the tiptoe. In Fig. 3-9, q_c and q_d are the common-mode and the differential-mode angles. The detail of these angles is explained in Subsection 3.3.3. The important features of the spring-mass are 1) a concentrated body mass with a light-weight leg, and 2) a linear spring which is proportional to the leg length. To attain the first point, a parallel-link mechanism is employed. In a parallel link mechanism, the heavy actuator parts are located on the body base, and the leg parts become lightweight. The robot dynamics becomes similar to a concentrated body mass with a lightweight leg. As for the second point, a leg spring is set on the knee to become parallel to the line of the body and the tiptoe. By this setting, the elastic force becomes parallel to the line length of the body and the tiptoe, or leg length. These two points realize dynamics near spring-mass dynamics. Fig. 3-8 shows kinematic illustrations of the legged robot in the experiments. The robot body is constrained to the vertical axis for the simplicity of experiments. The tiptoe in the air is not constrained.

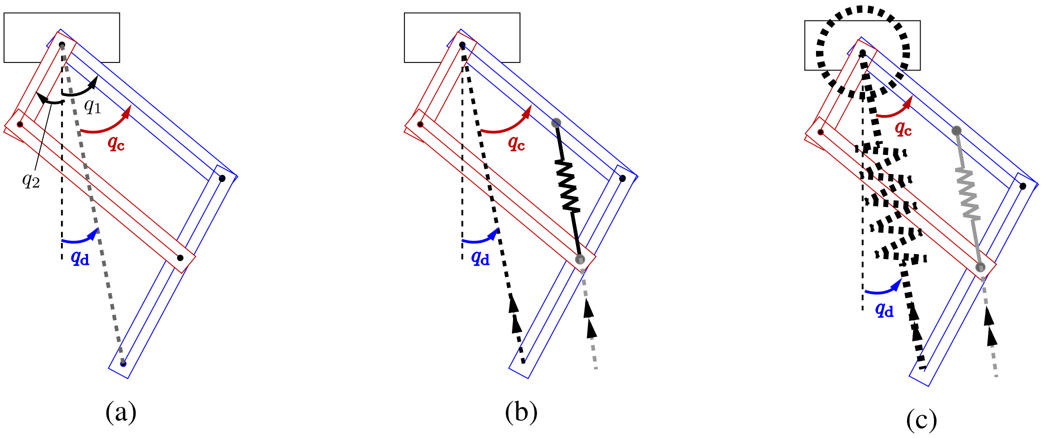

Fig. 3-9: Geometric relation: (a) Leg length and leg angle, (b) Parallel spring (c) Approximation to a spring-mass model.

3.3.1 Definitions of Coordinates

This paper uses three coordinates: the world coordinate, the base coordinate, and the polar base coordinate. The definitions of the coordinates are as follows. The world coordinate is an orthogonal coordinate in which the origin is the cross point of the ground and the vertical axis as Fig. 3-10. The robot dynamics for simulation are calculated in the world coordinate. The base coordinate is an orthogonal coordinate in which the origin is the axis of the two actuators in the sagittal plane as Fig. 3-11. The base coordinate is used for control. The polar base coordinate is a polar coordinate in which the origin is the axis of the two actuators in the sagittal plane. The polar base coordinate is used for calculating the elastic force of the linear leg spring.

3.3.2 Kinematcis

Jacobian matrices are induced in the world coordinate and in the base coordinate.

From Fig. 3-8, the tiptoe position in the world coordinate $\boldsymbol{x}_{\mathrm{tW}} = [x_{\mathrm{tW}}, z_{\mathrm{tW}}]$ is expressed as

$$[x_{\mathrm{tW}}, z_{\mathrm{tW}}] = [l_1 \sin q_1 - l_2 \sin q_2, z_{\mathrm{b}} - l_1 \cos q_1 + l_2 \cos q_2], \tag{3.3}$$

where l is link length, $\boldsymbol{q} = [q_1, q_2]$ is the vector of the actuator angles, and z_{b} is height of body in the world coordinate. Because the robot body is constrained to the vertical axis, the variables of the motion equation in the world coordinate are $\boldsymbol{q}_{\mathrm{w}} = [z_{\mathrm{b}}, q_1, q_2]$. The Jacobian matrix in the world coordinate

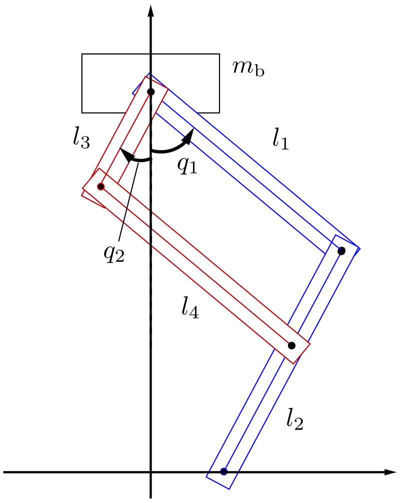

Fig. 3-10: World coordinate: the origin is at the cross point of the ground and the vertical axis.

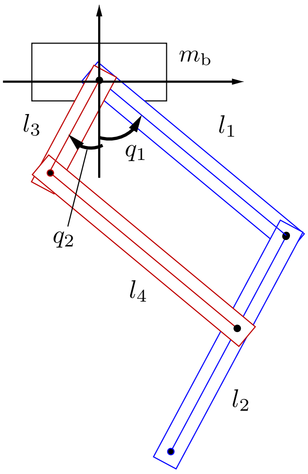

Fig. 3-11: Base coordiante: the origin is at the center of the body.

$\boldsymbol{J}_\mathrm{acoW}$ can be induced from partial derivative by $\boldsymbol{q}_\mathrm{w}$ as

$$\begin{aligned}\boldsymbol{J}_\mathrm{acoW} = \frac{\partial \boldsymbol{x}_\mathrm{tW}}{\partial \boldsymbol{q}_\mathrm{w}} &= \begin{bmatrix} \frac{\partial x_\mathrm{tW}}{\partial z_\mathrm{b}} & \frac{\partial x_\mathrm{tW}}{\partial q_1} & \frac{\partial x_\mathrm{tW}}{\partial q_2} \\ \frac{\partial z_\mathrm{tW}}{\partial z_\mathrm{b}} & \frac{\partial z_\mathrm{tW}}{\partial q_1} & \frac{\partial z_\mathrm{tW}}{\partial q_2} \end{bmatrix} \\ &= \begin{bmatrix} 0 & l_1 \cos q_1 & l_2 \cos q_2 \\ 1 & l_1 \sin q_1 & l_2 \sin q_2 \end{bmatrix}. \end{aligned} \tag{3.4}$$

The tiptoe position in the base coordinate $\boldsymbol{x}_t = [x_\mathrm{t}, z_\mathrm{t}]$ is

$$[x_\mathrm{t}, z_\mathrm{t}] = [l_1 \sin q_1 - l_2 \sin q_2, -l_1 \cos q_1 - l_2 \cos q_2]. \tag{3.5}$$

Because the variable in the base coordinate is $\boldsymbol{q} = [q_1, q_2]$, the Jacobian matrix in the base coordinate $\boldsymbol{J}_\mathrm{aco}$ is induced as

$$\begin{aligned}\boldsymbol{J}_\mathrm{aco} = \frac{\partial \boldsymbol{x}_\mathrm{t}}{\partial \boldsymbol{q}} &= \begin{bmatrix} \frac{\partial x_\mathrm{t}}{\partial q_1} & \frac{\partial x_\mathrm{t}}{\partial q_2} \\ \frac{\partial z_\mathrm{t}}{\partial q_1} & \frac{\partial z_\mathrm{t}}{\partial q_2} \end{bmatrix} \\ &= \begin{bmatrix} l_1 \cos q_1 & -l_2 \cos q_2 \\ l_1 \sin q_1 & l_2 \sin q_2 \end{bmatrix}. \end{aligned} \tag{3.6}$$

3.3.3 Leg Spring

For presenting the ideal characteristics of the leg spring, “leg length” and “leg angle” are defined. The leg length is the line length between the body and the tiptoe. The leg angle is the angle between the vertical line which crosses the center of the body and the line of the leg length. The leg length and the leg angle are the variables of the polar base coordinate. The ideal characteristics of the leg spring are that the elastic force is proportional to the leg length, and that the elastic force is not determined by the leg angle.

Fig. 3-9 shows the geometric relation of the robot body, the spring, and the leg angle. Assuming that the common mode and the differential mode of $[q_1, q_2]$ are q_c and q_d, the variables $[q_c, q_\mathrm{d}]$ are defined as

$$\begin{bmatrix} q_c \\ q_\mathrm{d} \end{bmatrix} = \frac{1}{2} \begin{bmatrix} 1 & 1 \\ 1 & -1 \end{bmatrix} \begin{bmatrix} q_1 \\ q_2 \end{bmatrix}. \tag{3.7}$$

When $l_1 = l_2 = l$, the leg length L and the leg angle Θ are expressed using q_c and q_d as

$$L = 2l \cos q_c \tag{3.8}$$

$$\Theta = q_\mathrm{d}. \tag{3.9}$$

From (3.8) and (3.9), the leg length and the leg angle are independent variables in terms of q_c and q_d.

The leg spring at the knee joint is set parallel to the line of the body and the tiptoe as Fig. 3-9 (b). The elastic force of the leg spring can be induced from the partial derivative of the potential energy. The potential energy of the leg spring U is calculated as

$$U = \frac{1}{2} K_\mathrm{sp} \left(\frac{L}{3} - l_0 \right)^2 . \tag{3.10}$$

Here, l_0 is the natural length of the spring. K_sp is the stiffness of the linear spring. The elastic force $\boldsymbol{F}_\mathrm{k}$ of the leg spring in terms of $[L, \Theta]$ is induced from the partial derivative of the potential energy by $[L, \Theta]$ as

$$\boldsymbol{F}_\mathrm{k} = \left[\frac{\partial U}{\partial L}, \frac{\partial U}{\partial \Theta} \right] = \left[\frac{K_\mathrm{sp}}{3} \left(\frac{L}{3} - l_0 \right), 0 \right] . \tag{3.11}$$

As (3.11), the elastic force affects the leg length, and does not affect the leg angle. This is equal to the ideal characteristics of the spring in a spring-mass hopping. Because the center of gravity of the legged robot is set almost in the body by the parallel-link mechanism, the total dynamics become near a spring-mass model as Fig. 3-9 (c).

3.3.4 Dynamics

The motion equation of the robot in the world coordinate is described. The motion equation in the world coordinate is

$$\boldsymbol{J}(\boldsymbol{q}_\mathrm{w})\ddot{\boldsymbol{q}}_\mathrm{w} + \boldsymbol{g}(\boldsymbol{q}_\mathrm{w}, \dot{\boldsymbol{q}}_\mathrm{w}) + \boldsymbol{\tau}_\mathrm{k}(\boldsymbol{q}_\mathrm{w}) = \boldsymbol{\tau}^\mathrm{ref} - \boldsymbol{\tau}^\mathrm{fric} + \boldsymbol{J}_\mathrm{acoW}^T \boldsymbol{F}_\mathrm{e}. \tag{3.12}$$

Here, $\boldsymbol{J}(\boldsymbol{q}_{\mathrm{w}})$ is the inertia matrix, $\boldsymbol{g}(\boldsymbol{q}_{\mathrm{w}}, \dot{\boldsymbol{q}}_{\mathrm{w}})$ is the nonlinear terms of the rigid-body dynamics, $\boldsymbol{\tau}_{\mathrm{k}}(\boldsymbol{q}_{\mathrm{w}})$ is the elastic torque of the leg spring, $\boldsymbol{\tau}^{\mathrm{ref}}$ is the torque reference of the actuators, $\boldsymbol{\tau}^{\mathrm{fric}}$ is the friction torque, $\boldsymbol{J}_{\mathrm{acoW}}$ is Jacobian matrix of the tiptoe in the world coordinate, and $\boldsymbol{F}_{\mathrm{e}}$ is the external force from the environment to the tiptoe. It is possible to induce the elastic force in the torque dimension as $\boldsymbol{\tau}_{\mathrm{k}}$ by partial derivative.

The elastic force of the leg spring is transformed in the torque dimension for the motion equation. The elastic torque $\boldsymbol{\tau}_{\mathrm{k}}$ of the leg spring in terms of the joint angles $[q_1, q_2]$ is induced from the partial derivative of the potential energy U by the joint angles $[q_1, q_2]$. Using (3.10) and that the leg lenght is $L = 2l\cos\frac{q_1+q_2}{2}$, the elastic torque of the leg spring is derived as

$$\boldsymbol{\tau}_{\mathrm{k}} = \frac{\partial U}{\partial \boldsymbol{q}} = \left[\frac{\partial U}{\partial q_1}, \frac{\partial U}{\partial q_2}\right] \tag{3.13}$$

$$\frac{\partial U}{\partial q_1} = \frac{\partial U}{\partial q_2} = -\frac{K_{\mathrm{sp}} l \sin\frac{q_1+q_2}{2}}{3}\left(\frac{2l\cos\frac{q_1+q_2}{2}}{3} - l_0\right). \tag{3.14}$$

The inertia matrices in the base cooridnate $\boldsymbol{J}_{\mathrm{b}}$ and in the world coordinate $\boldsymbol{J}_{\mathrm{sp}}$ are induced. $\boldsymbol{J}_{\mathrm{b}}$ is used when the body mass does not affect the control of the leg motion (such as in the aerial phase). $\boldsymbol{J}_{\mathrm{sp}}$ is used when the body mass affects the control of the leg motion (such as in the support phase). The elements of the inertia matrix in the base cooridnate $\boldsymbol{J}_{\mathrm{b}}$ can be calculated based on Fig. 3-11 as

$$J_{\mathrm{b}11} = m_1 r_1^2 + m_2 l_1^2 + m_4 r_4^2 \tag{3.15}$$

$$J_{\mathrm{b}12} = -(m_2 l_1 r_2 + m_4 l_3 r_4)\cos(q_1 + q_2) \tag{3.16}$$

$$J_{\mathrm{b}21} = J_{12} \tag{3.17}$$

$$J_{\mathrm{b}22} = m_3 r_3^2 + m_4 l_3^2 + m_2 r_2^2. \tag{3.18}$$

Here, m_i, l_i, and r_i show the mass, the link length, and the COG position of the i th bar. The elements of the inertia matrix in the world coordinate $\boldsymbol{J}_{\mathrm{sp}}$ are calculated based on Fig. 3-10 as

$$J_{\mathrm{sp}11} = m_1 r_1^2 + m_{\mathrm{b}} l_1^2 + m_3 l_1^2 + m_4 (l_1 - r_4)^2 \tag{3.19}$$

$$J_{\mathrm{sp}12} = -(m_1 l_2 r_1 + m_{\mathrm{b}} l_1 l_2 + m_3 (l_2 - r_3) l_1 + m_4 (l_2 - l_3)(l_1 - r_4))\cos(q_1 + q_2) \tag{3.20}$$

$$J_{\mathrm{sp}21} = J_{12} \tag{3.21}$$

$$J_{\mathrm{sp}22} = m_1 l_2^2 + m_2 r_2^2 + m_3 (l_2 - r_3)^2 + m_4 (l_2 - l_3)^2 + m_{\mathrm{b}} l_2^2. \tag{3.22}$$

Here, m_{b} is the mass of the base. From the comparison of $\boldsymbol{J}_{\mathrm{b}}$ and $\boldsymbol{J}_{\mathrm{sp}}$, it is found that the inertia matrix is different. Because the mass of the base m_{b} is large in general, $\boldsymbol{J}_{\mathrm{sp}}$ becomes larger in general.

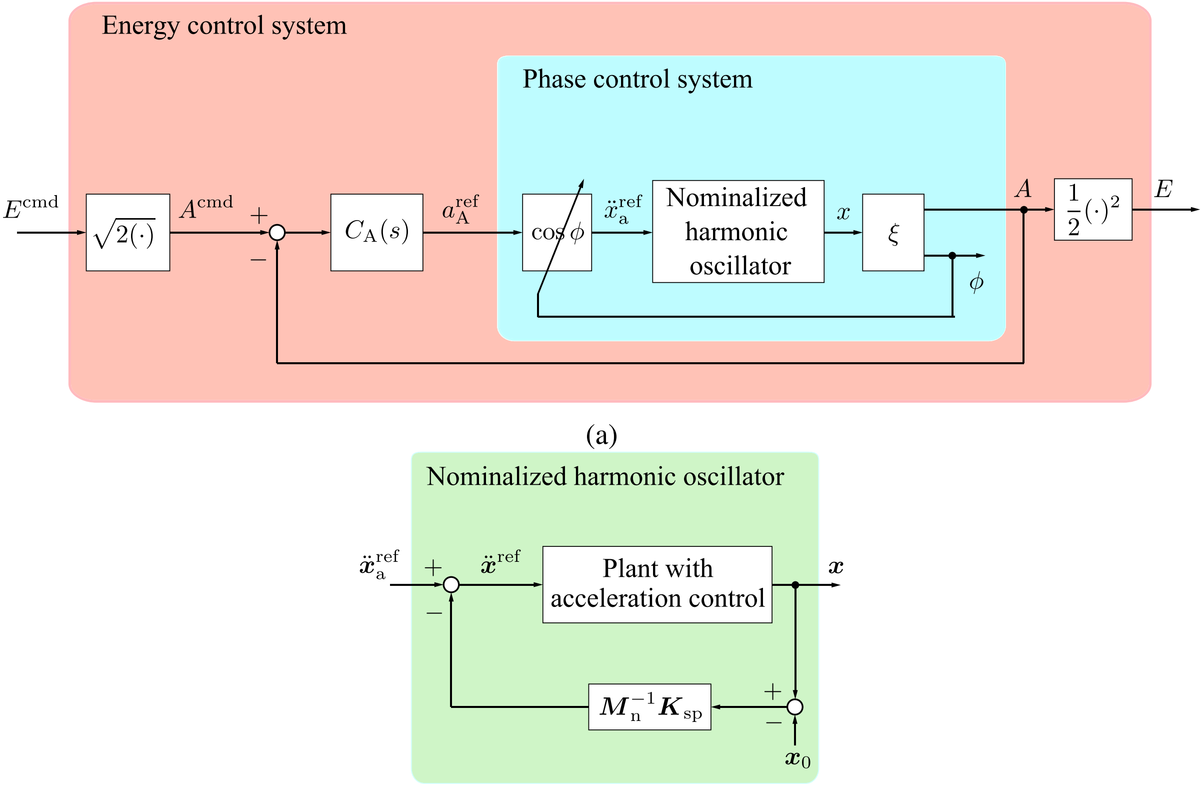

(a)

(b)

Fig. 3-12: Block diagram of energy/phase control for a multi-degree-of-freedom system: (a) total control system, (b) nominalized harmonic oscillator.

In the simulations and the experiments in this dissertation, the desired nominal inertia $\boldsymbol{J}_{\mathrm{n}} = \boldsymbol{J}_{\mathrm{aco}}^T \boldsymbol{M}_{\mathrm{d}} \boldsymbol{J}_{\mathrm{aco}}$ is employed. Here, $\boldsymbol{M}_{\mathrm{d}} = \begin{bmatrix} M_{\mathrm{d}} & 0 \\ 0 & M_{\mathrm{d}} \end{bmatrix}$ is the desired inertia, and $M_{\mathrm{d}} = M = m_{\mathrm{b}} + m_1 + m_2 + m_3 + m_4$. The inertia matrix is derived as

$$\boldsymbol{J}_{\mathrm{aco}}^T \boldsymbol{M}_{\mathrm{d}} \boldsymbol{J}_{\mathrm{aco}} = \boldsymbol{J}_{\mathrm{aco}}^T \begin{bmatrix} M & 0 \\ 0 & M \end{bmatrix} \boldsymbol{J}_{\mathrm{aco}} \tag{3.23}$$

$$= \begin{bmatrix} Ml_1^2 & -Ml_1 l_2 \cos(q_1 + q_2) \\ -Ml_1 l_2 \cos(q_1 + q_2) & Ml_2^2 \end{bmatrix} \tag{3.24}$$

(3.24) is equal to $\boldsymbol{J}_{\mathrm{sp}}$ with the case that the mass is concentrated on the body (namely $m_{\mathrm{b}} = M$ and $m_1 = m_2 = m_3 = m_4 = 0$).

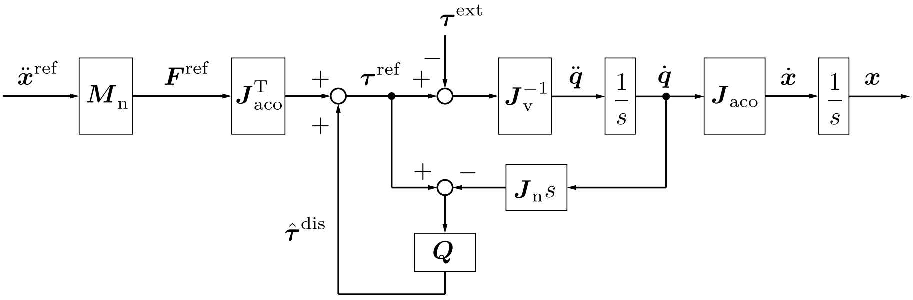

Fig. 3-13: Block diagram of joint space observer.

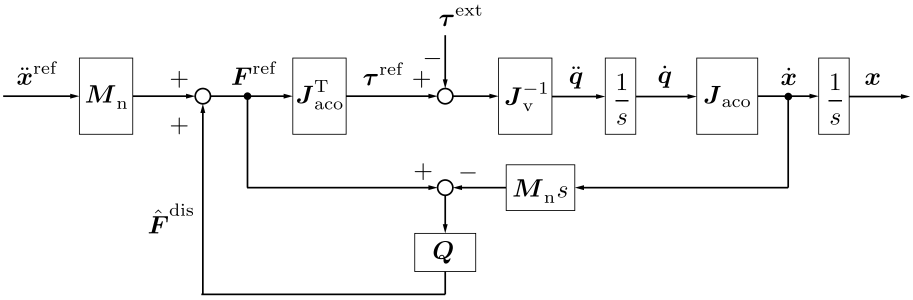

Fig. 3-14: Block diagram of workspace observer.

3.4 Disturbance Observers for a Multi-DOF Robot

Disturbance observers for nominalization are introduced. The total block diagram of the energy/phase control for a multi-degree-of-freedom system is shown in Fig. 3-12 (a). $\ddot{x}_{\mathrm{a}}^{\mathrm{ref}}$ is the acceleration reference of the energy/phase control. The “nominalized harmonic oscillator” block is concretely shown as Fig. 3-12 (b). $\ddot{x}^{\mathrm{ref}}$ is the acceleration reference of the acceleration control system. M_{n} is the nominal mass matrix. x_0 is the position of the equilibrium point. The inner block of Fig. 3-12 (b) is the plant with acceleration control, and the outer loop implies a virtual elastic force. The “plant with acceleration control” block expresses the plant with a disturbance observer. Two types of disturbance observers are considered: a joint-space observer and a workspace observer. A joint-space observer is a disturbance observer in joint space, and a workspace observer is a disturbance observer in the workspace.

3.4.1 Joint-Space Observer

A block diagram of a joint-space observer is shown in Fig. 3-13. J_{n} is the nominal inertia, and Q is a low-pass filter. J_{v} is the variable inertia which expresses the real dynamics. The output of the joint

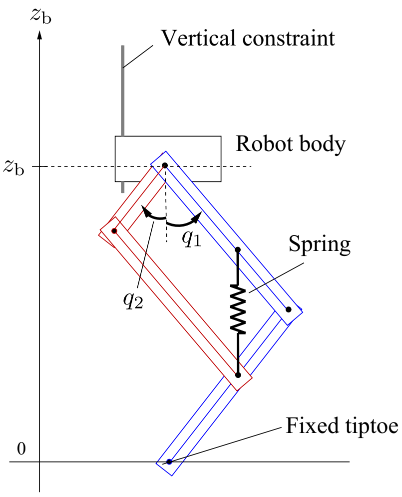

Fig. 3-15: Simulation setup in Chapter 3.

space observer $\hat{\boldsymbol{\tau}}^\mathrm{dis}$ is written as

$$\hat{\boldsymbol{\tau}}^\mathrm{dis} = \boldsymbol{Q}(\boldsymbol{\tau}^\mathrm{ref} - \boldsymbol{J}_\mathrm{n} s). \tag{3.25}$$

$\boldsymbol{J}_\mathrm{v}$ is equal to $\boldsymbol{J}_\mathrm{sp}$ when the tiptoe contacts the ground, and is equal to $\boldsymbol{J}_\mathrm{b}$ in the air. Three patterns are considered as the candidates of the nominal inertia $\boldsymbol{J}_\mathrm{n}$:

- constant inertia $\boldsymbol{J}_\mathrm{c} = \mathrm{diag}(\boldsymbol{J}_\mathrm{v})$, which is often used as a simple nominal inertia
- variable inertia $\boldsymbol{J}_\mathrm{v}$, which expresses the real dynamics (the elements of the inertia matrix vary in response to the posture)
- variable inertia $\boldsymbol{J}_\mathrm{p} = \boldsymbol{J}_\mathrm{aco}^\mathrm{T} M_\mathrm{n} \boldsymbol{J}_\mathrm{aco}$, which is equivalent to constant mass in the workspace

3.4.2 Workspace Observer

A block diagram of a workspace observer is drawn as Fig. 3-14. The output of the workspace observer $\hat{\boldsymbol{F}}^\mathrm{dis}$ is the disturbance in the workspace. $\hat{\boldsymbol{F}}^\mathrm{dis}$ is calculated as

$$\hat{\boldsymbol{F}}^\mathrm{dis} = \boldsymbol{Q}(\boldsymbol{F}^\mathrm{ref} - \boldsymbol{M}_\mathrm{n} s). \tag{3.26}$$

Here, $\boldsymbol{M}_\mathrm{n}$ is the nominal mass matrix, or the desired mass matrix. The estimated disturbance in the workspace $\hat{\boldsymbol{F}}^\mathrm{dis}$ is compensated in the workspace as Fig. 3-14.

3.5 Comparative Simulations

Simulations are conducted in order to verify the proposed energy/phase control for a multi-DOF robot by the disturbance observers.

The four observer-based nominalization controls are compared: a joint-space observer with constant mass (JOBc), a joint-space observer with variable mass (JOBv), a joint-space observer proposed in [113] (JOBp), and a workspace observer (WOB). A joint-space observer nominalizes dynamics in the joint space as Fig. 3-13, and a workspace observer nominalizes dynamics in the workspace as Fig. 3-14. While the nominal inertia of the JOBc is constant, the nominal inertia of the JOBv is varied so that the nominal inertia is equal to the theoretical inertia. The nominal inertia of the JOBp is varied so that the mass in the workspace is constant. The JOBp and the WOB are common in terms of that the mass in the workspace is set as constant.

The detail of the simulations is as follows. The simulation setup is considered as Fig. 3-15. The robot body is constrained to the vertical motion, and the tiptoe is fixed to the ground. The robot body is oscillated by the energy/phase control with the disturbance observers. The disturbance observers are JOBc, JOBv, JOBp, and WOB. The energy command in the energy/phase control is set so that the desired position amplitude in the vibration is 0.1 m. The indices are the energy consumption, the control error, and the robust variation. An example of the times-series results is shown in Fig. 3-16. The amplitudes and the periods are measured from the time-series results. The amplitude in the simulations is calculated as the peak value from the equilibrium point. The period in the simulations is calculated as the peak-to-peak time.

Two types of the simulations are conducted as Chapter 2. Simulations 3-1 deal with the trade-off between the control error and the energy consumption. The indices of the control error and the energy consumption are calculated and compared. The control error and the energy consumption are concretely calculated using (2.72) and (2.73) in Subsection 2.5.1, respectively. In simulations 3-1, the simulations are conducted with the three patterns of the observer cut-off frequency $g_{\mathrm{dis}} = 25, 50, 100$ rad/s. Simulations 3-2 deal with the trade-off between the robustness and the energy consumption. Simulations 3-2 also employ the three patterns of the observer cut-off frequency $g_{\mathrm{dis}} = 25, 50, 100$ rad/s. The evaluation index of the robustness is the trajectory variation by the stiffness variation (2.76) as Subsection 2.5.2. The stiffness is varied $\pm 10\%$ in each case as Subsection 2.5.2.

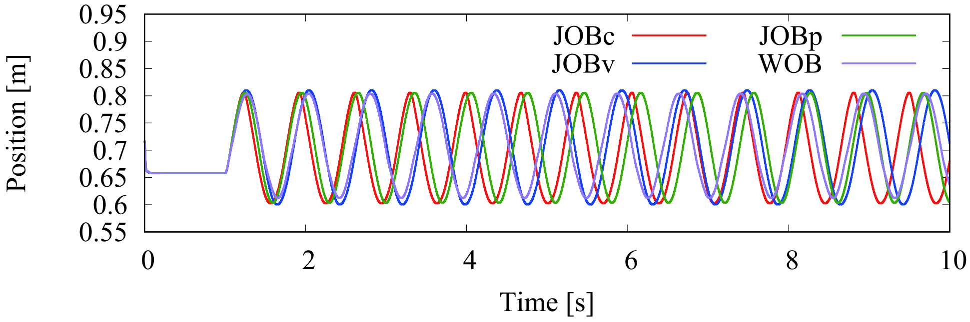

Fig. 3-16: Example of the simulation results in Chapter 3.

Table 3.3: Results of simulations 3-1: energy consumption and control error.

Controller Control method	 Gain	Control error TotalError [%]	Energy consumption EC [J]
JOBc	$g_{\text{dis}} = 25$	9.10	185.29
	$g_{\text{dis}} = 50$	14.26	201.07
	$g_{\text{dis}} = 100$	18.45	211.95
JOBv	$g_{\text{dis}} = 25$	6.17	151.27
	$g_{\text{dis}} = 50$	5.74	149.42
	$g_{\text{dis}} = 100$	5.59	149.36
JOBp	$g_{\text{dis}} = 25$	8.33	162.63
	$g_{\text{dis}} = 50$	10.43	167.85
	$g_{\text{dis}} = 100$	10.89	169.12
WOB	$g_{\text{dis}} = 25$	16.69	706.12
	$g_{\text{dis}} = 50$	8.92	707.19
	$g_{\text{dis}} = 100$	8.54	671.14

3.5.1 Energy Consumption versus Control Error

The respective control system is compared in terms of the energy consumption and the control error. Table 3.3 shows the result of the respective method and gain. The control error is large as a whole (more than 5 % in all results) owing to the error of the period rather than the error of the amplitude. Fig. 3-17 shows the best results of the respective observers. In Fig. 3-17, JOBv performs the best in terms of both the control error and the energy consumption. The control error is 5.59 %, and the energy consumption is 149.36 J. In Fig. 3-17, JOBp shows the intermediate performance between JOBv and JOBc in terms of both the control error and the energy consumption. The energy consumption of WOB is very high as 671.14 J. WOB has high robustness against the parameter variation. High robustness requires high

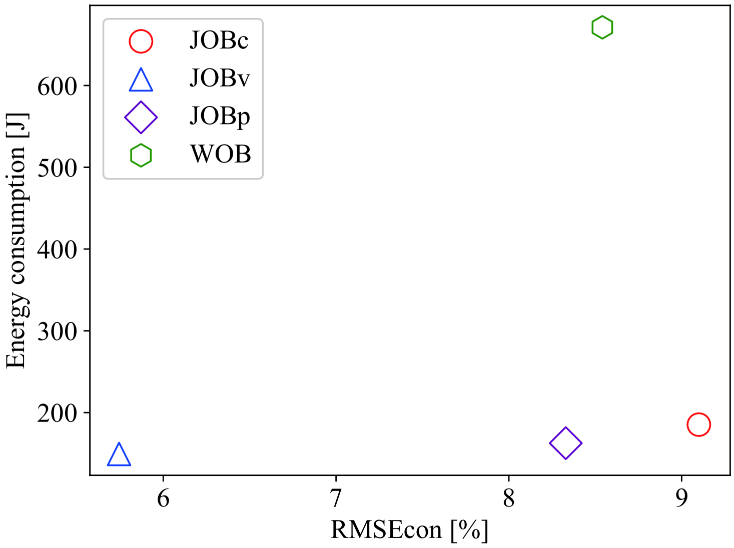

Fig. 3-17: Summary results of simulations 3-1: the best results of the respective observers.

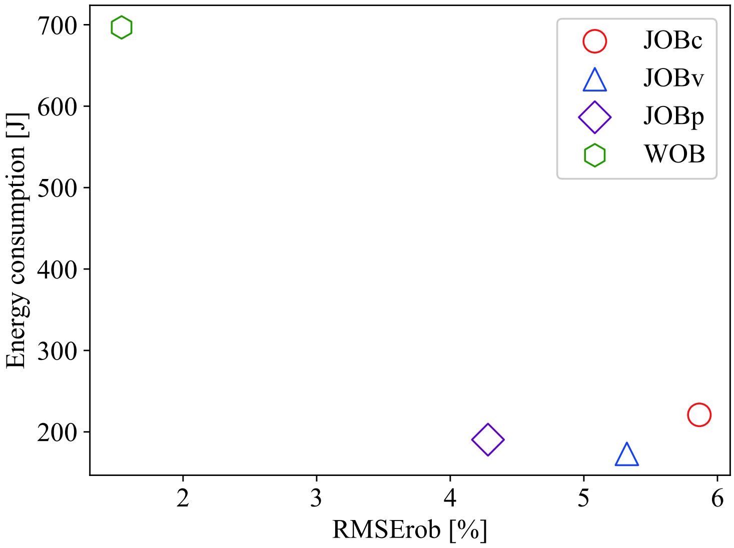

Fig. 3-18: Summary results of simulations 3-2: the best results of the respective observers.

energy consumption in return. The detail is shown and discussed in Subsection 3.5.2.

3.5.2 Energy Consumption versus Robustness to Parameter Variation

The results of simulations 3-2 are shown in Table 3.4. The best results of the respective observers are summarized in Fig. 3-18. WOB shows the high robustness. The error against the parameter variation is around 1.5 %. Instead of the high robustness, the high energy consumption is shown as around 700 J.

Table 3.4: Results of simulations 3-2: energy consumption and robustness.

Controller Control method	Gain	Robustness TotalRobustness [%]	Energy consumption EC [J]
JOBc	$g_{\mathrm{dis}} = 25$	6.12	204.20
	$g_{\mathrm{dis}} = 50$	5.86	220.93
	$g_{\mathrm{dis}} = 100$	5.79	236.77
JOBv	$g_{\mathrm{dis}} = 25$	5.63	173.51
	$g_{\mathrm{dis}} = 50$	5.32	173.01
	$g_{\mathrm{dis}} = 100$	5.20	173.14
JOBp	$g_{\mathrm{dis}} = 25$	4.57	187.32
	$g_{\mathrm{dis}} = 50$	4.28	190.44
	$g_{\mathrm{dis}} = 100$	4.32	190.51
WOB	$g_{\mathrm{dis}} = 25$	1.48	707.61
	$g_{\mathrm{dis}} = 50$	1.60	700.33
	$g_{\mathrm{dis}} = 100$	1.54	696.73

The structure of WOB shows that the system is nominalized as the desired dynamics by one more outer loop compared to JOB. JOBp shows the best robustness among JOBc, JOBv, and JOBp as 4.28 %. The energy consumption of JOBp is 190 J, and is between JOBv and JOBc as Fig. 3-18. The method of the minimum energy consumption is JOBv as 173 J. The robustness of JOBv is 5.32 %, and is worse than JOBp. The robustness and the control error have a trade-off.

In summary, the three indices (the energy consumption, the control error, and the robustness) have trade-off each other. In terms of the energy consumption and the control error, JOBv shows the best performance. JOBv employs the inertia of the real dynamics. Instead, the robustness of JOBv is not superior. In terms of only the robustness, WOB shows the best performance. In the structure of WOB, the dynamics are nominalized by one more outer loop. On the other hand, the energy consumption of WOB becomes very high. JOBp shows the intermediate performance between JOBv and WOB. While the nominal inertia of JOBp is set as the mass on the body as WOB, the control structure of JOBp is the same as JOBv. It is desirable that the observer is selected according to the specifications. In Chapters 4 and 5, JOBp is employed owing to the balanced performance.

3.6 Summary

This chapter described the mechanism and the control for applying the energy/phase control to a legged robot. The design philosophy of the mechanism is to make the dynamics similar to a spring-mass system. To realize a mass point at the body as much as possible, the parallel-link mechanism is employed. To realize a linear leg spring, the linear spring is set so that the spring is parallel to the leg length. The residual error of the dynamics is compensated by a disturbance observer. Four disturbance observers (JOBc, JOBv, JOBp, and WOB) were compared through the simulations under the legged mechanism. The comparison was conducted in terms of the three indices as Chapter2: the energy consumption, the control error, and the robustness. JOBv showed the best performance in terms of the energy consumption and the control error. WOB showed the best performance in the robustness. JOBp showed the balanced and intermediate performance between JOBv and WOB.

Chapter 4

Hopping-Height Control Based on Energy/Phase Control

4.1 Introduction

A hopping motion requires high power while the actuation power of motors is limited. It is desirable that the potential energy of a mechanical spring is utilized efficiently. The target problem of this chapter is energy-efficient hopping-height control of a one-leg hopping robot, especially utilizing the resonance of mechanical spring.

This section approaches the problem by applying the energy/phase control in Chapter 2 and the nominalizing method in Chapter 3. The nominalizing control in Chapter 3 enables to make the dynamics of a nonlinear legged robot as the dynamics of a linear simple harmonic oscillator. The energy/phase control in Chapter 2 enables the control of the mechanical energy utilizing the resonance of a harmonic oscillator. Section 4.2 discusses concretely applying the energy/phase control to the hopping height control. Section 4.3 deals with the compensation control for a hopping robot looking back on Chapter 3. In Section 4.4, simulations using a simple spring-mass hopping robot are conducted. In Section 4.5, experiments using a one-leg hopping robot with a mechanical spring are conducted. Section 4.6 concludes this chapter.

4.2 Hopping-Height Control by Energy/Phase Control

Fig. 4-1 shows the procedure in the stance phase of the hopping motion. z_{b} is the height of the body mass. A new phase variable θ is introduced for clear presentation of the phase in the hopping control.

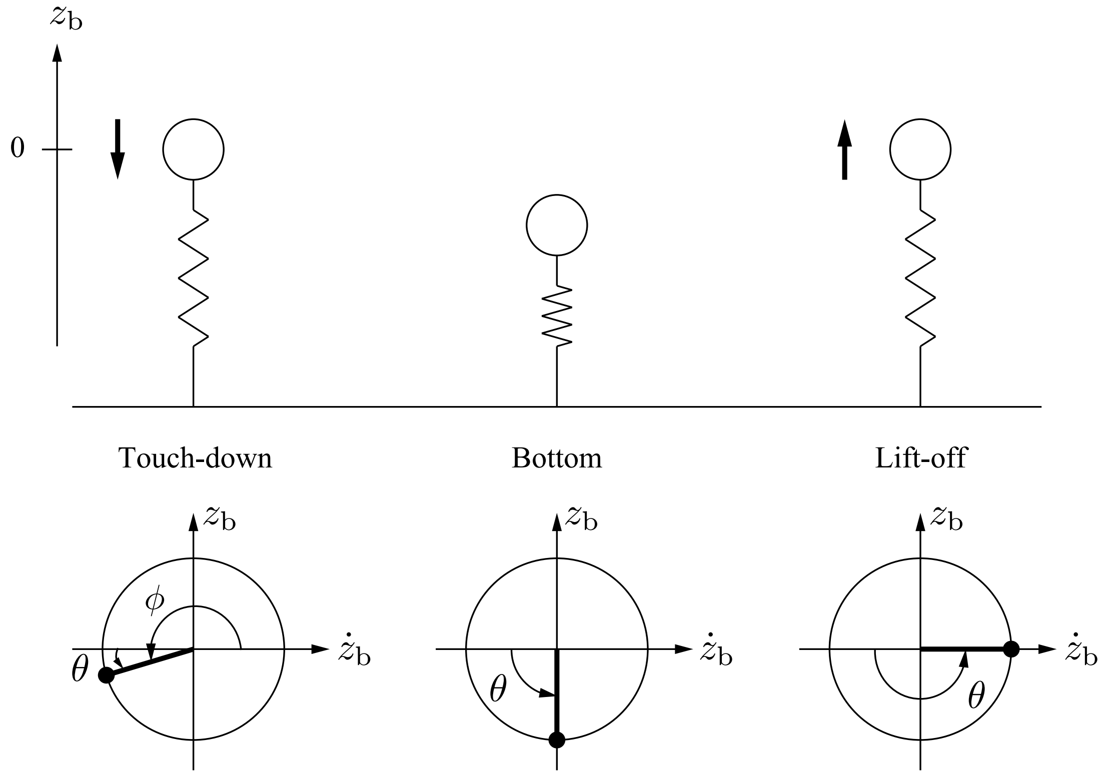

Fig. 4-1: Flow of hopping in stance phase.

The variable θ is defined as

$$\theta = \phi - \pi. \tag{4.1}$$

The phase variable θ moves from 0 to π in the stance phase while ϕ moves from π to 2π. θ is more clear to understand because the phase starts from 0 and ends at π. There are three main events in the stance phase as Fig. 4-1: touch down, bottom, and lift off. Touch down is the moment when the robot in the air touches the ground. At this moment, θ is near zero. From (2.16) and (4.1), the force reference becomes the negative maximum value at the touch down. The bottom is when the spring is compressed maximum and the mass velocity becomes zero. At this time, θ becomes $\frac{\pi}{2}$. From (2.16) and (4.1), the force reference is zero in this case. Liftoff is the moment when the robot flies from the ground. At liftoff, the velocity of the robot body becomes the maximum. At this moment, θ becomes π. From (2.16) and (4.1), the cosine becomes the positive maximum value at liftoff.

Energy/phase control for the hopping-height control is explained. The periodic flow of the control is shown in Fig. 4-2. Two control states are introduced: the stance phase and the flight phase. The stance

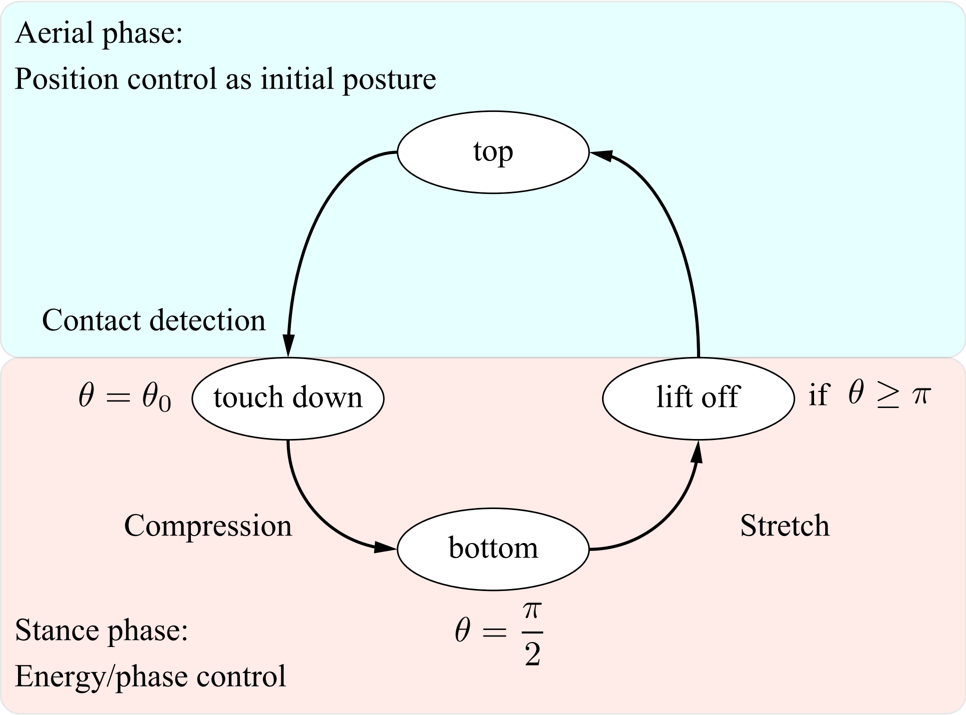

Fig. 4-2: State transition of the z-axis control in the hopping-height control.

phase is the phase on the ground, and the flight phase is the phase in the air. Fig. 4-3 shows the block diagrams of the control system for the hopping height control. Because the body has only vertical motion in this paper, the x-axis position of the tiptoe is always controlled as zero by position control in Fig. 4-3 (a). In Fig. 4-3 (a), $\boldsymbol{x}_{\mathrm{t}}$ denotes the position of the tiptoe. The “nominalized one mass system” block in Fig. 4-3 (a) is equal to the block that eliminates the virtual elastic force from the nominalized harmonic oscillator of Fig. 4-4. As for z axis, energy/phase control is implemented in the stance phase as Fig. 4-3 (b). The transition from the stance phase to the flight phase occurs when $\theta \geq \pi$. This means that the body height is higher than the initial height, which is the lift-off height. In the flight phase, position control is implemented to the x-axis and the z-axis as Fig. 4-3 (a). The position command is the initial posture of the legged robot. By this approach, the COG velocity is preserved, and the relative vibration between the body and the leg is not induced. When the contact to the ground is detected, the flight phase changes to the stance phase. In this experimental setup, contact detection is implemented using the body height. As mentioned above, the states and the controls are switched periodically.

The total block diagram of the hopping control at the stance phase is shown in Fig. 4-3. Fig. 4-3 (a) shows the control system of the x direction, which is the typical position control. $\boldsymbol{x}_{\mathrm{t}}^{\mathrm{cmd}}$ is the position

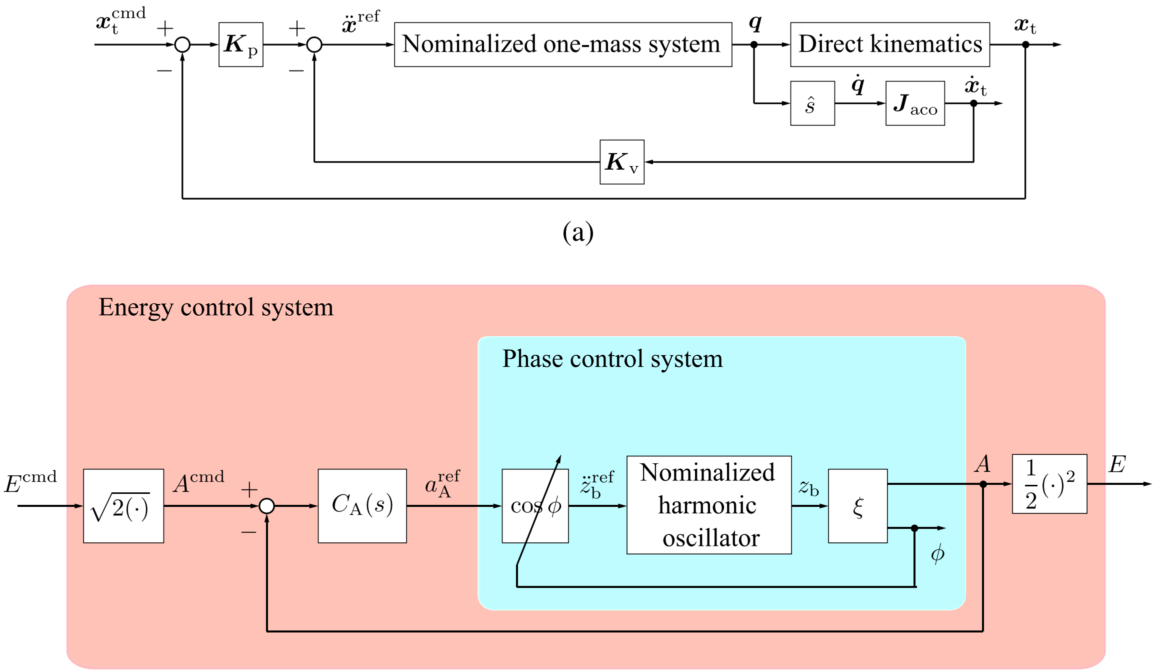

(a)

(b)

Fig. 4-3: Block diagram of the control systems: (a) position control, (b) energy/phase control.

command of the tiptoe in the base coordinate. Fig. 4-3 (b) shows the control system of the z direction, which is the block diagram of the energy/phase control. z_b is the height of the body, and $\ddot{z}_\mathrm{b}^\mathrm{ref}$ is the acceleration reference of the body in the z direction. The desired hopping height H^des is defined as the desired height from the balance of the position. The origin of the height for calculation of the energy is the balanced position. Because the robot lifts off at the balanced position, the potential energy at liftoff is zero. For the desired top height, the total desired energy is equal to the gravitational potential energy of H^des. The mechanical energy command per unit mass E^cmd is calculated using H^des as

$$E^\mathrm{cmd} = gH^\mathrm{des}, \tag{4.2}$$

where g is gravitational acceleration. From the E^cmd and (2.14), the amplitude command A^cmd is induced as

$$A^\mathrm{cmd} = \sqrt{2E^\mathrm{cmd}}. \tag{4.3}$$

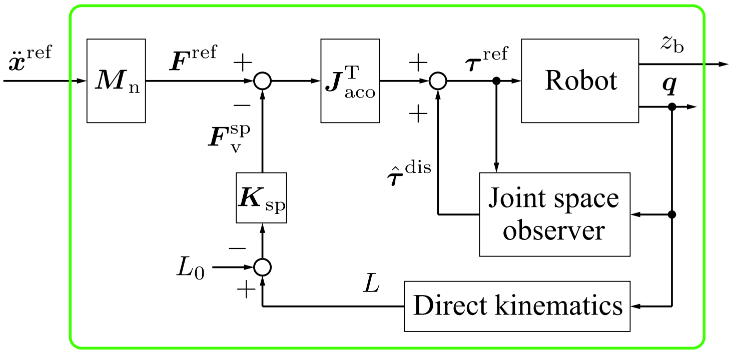

Fig. 4-4: Block diagram of a nominalized harmonic oscillator.

The mechanical energy per unit mass E and the amplitue A are derived respectively as

$$E = \frac{1}{2}(\dot{z}_{\mathrm{b}}^2 + \omega^2 z_{\mathrm{b}}^2) \tag{4.4}$$

$$A = \sqrt{2E} \tag{4.5}$$

The amplitude of the acceleration reference is derived by the equivalent energy controller as

$$a_{\mathrm{A}}^{\mathrm{ref}} = C_{\mathrm{A}}(A^{\mathrm{cmd}} - A). \tag{4.6}$$

The acceleration reference is induced as the product of the amplitude and the phase. The force reference is calculated by multiplying the mass by the acceleration reference. The acceleration reference $\ddot{z}_{\mathrm{b}}^{\mathrm{ref}}$ and the force reference $F_{\mathrm{z}}^{\mathrm{ref}}$ are expressed as

$$\ddot{z}_{\mathrm{b}}^{\mathrm{ref}} = a_{\mathrm{A}}^{\mathrm{ref}} \cos\phi \tag{4.7}$$

$$F_{\mathrm{z}}^{\mathrm{ref}} = M_{\mathrm{n}} \ddot{z}_{\mathrm{b}}^{\mathrm{ref}}. \tag{4.8}$$

The phase ϕ is calculated from the complex number ξ.

4.3 Compensation Control for Nominalization to a Spring-Mass System

This section explains compensation control to nominalize the robot dynamics as the desired spring-mass system. In order to realize the ideal spring-mass characteristics, disturbance rejection including the mechanical spring is implemented firstly by using a joint space observer. The dynamics are expressed as a simple motion equation with the nominalized mass particle and the force reference. Second, nominalization to the desired spring-mass system is implemented by adding the desired elastic force. These

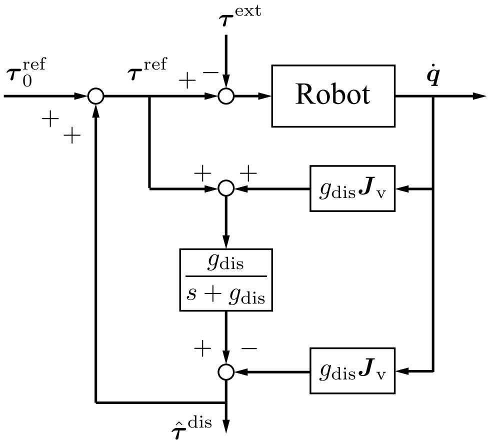

Fig. 4-5: Block diagram of a disturbance observer in joint space.

two steps can compensate the stiffness error and the damping of the mechanical spring, as well as the nonlinear terms.

4.3.1 Step 1: Disturbance Rejection and Nominalization to a One-Mass System

For the realization of the desired dynamics, the disturbance terms including the mechanical elastic force are rejected by a joint space observer firstly. The induced simple dynamics in the first step are composed of the nominalized mass particle and the force reference.

A joint space observer varies the inertia in joint space in order to make the mass in the workspace as the desired constant mass $\boldsymbol{M}_{\mathrm{n}}$. The variable inertia in joint space is calculated as

$$\boldsymbol{J}_{\mathrm{v}} = \boldsymbol{J}_{\mathrm{aco}}^{\mathrm{T}}\boldsymbol{M}_{\mathrm{n}}\boldsymbol{J}_{\mathrm{aco}}. \tag{4.9}$$

A block diagram of the joint space observer is shown in Fig. 4-5. g_{dis} is the cut-off frequency of the joint space observer, $\boldsymbol{\tau}^{ext}$ is the external torque, $\hat{\boldsymbol{\tau}}^{\mathrm{dis}}$ is the output torque of the joint space observer, and $\boldsymbol{\tau}_0^{\mathrm{ref}}$ is the torque reference before adding $\hat{\boldsymbol{\tau}}^{\mathrm{dis}}$. The output of the joint space observer is calculated as

$$\hat{\boldsymbol{\tau}}^{\mathrm{dis}} = \frac{g_{\mathrm{dis}}}{s+g_{\mathrm{dis}}}(\boldsymbol{\tau}^{\mathrm{ref}} + g_{\mathrm{dis}}\boldsymbol{J}_{\mathrm{v}}\dot{\boldsymbol{q}}) - g_{\mathrm{dis}}\boldsymbol{J}_{\mathrm{v}}\dot{\boldsymbol{q}}. \tag{4.10}$$

The dynamics under the joint space observer are induced. Firstly, the motion equation in joint space is transformed into the motion equation in the workspace. This paper assumes $\ddot{\boldsymbol{x}} \simeq \boldsymbol{J}_{\mathrm{aco}}\ddot{\boldsymbol{q}}$ and that the torque terms and the force terms satisfy the relation of statics as $\boldsymbol{F} = \boldsymbol{J}_{\mathrm{aco}}^{-\mathrm{T}}\boldsymbol{\tau}$. The motion equation in the workspace is

$$\boldsymbol{M}(\boldsymbol{q})\ddot{\boldsymbol{x}} + \boldsymbol{J}_{\mathrm{aco}}^{-\mathrm{T}}\boldsymbol{g}(\boldsymbol{q},\dot{\boldsymbol{q}}) + \boldsymbol{J}_{\mathrm{aco}}^{-\mathrm{T}}\boldsymbol{\tau}_{\mathrm{k}}(\boldsymbol{q}) = \boldsymbol{J}_{\mathrm{aco}}^{-\mathrm{T}}\boldsymbol{\tau}^{\mathrm{ref}} - \boldsymbol{J}_{\mathrm{aco}}^{-\mathrm{T}}\boldsymbol{\tau}^{\mathrm{fric}} + \boldsymbol{F}_e, \tag{4.11}$$

where $\boldsymbol{M}(q)$ is the equivalent mass matrix as

$$\boldsymbol{M}(\boldsymbol{q}) = \boldsymbol{J}_{\mathrm{aco}}^{-\mathrm{T}}(q)\boldsymbol{J}(\boldsymbol{q})\boldsymbol{J}_{\mathrm{aco}}^{-1}(\boldsymbol{q}). \tag{4.12}$$

$\boldsymbol{x} = [x_{\mathrm{b}}, z_{\mathrm{b}}]$ is the position of the body in the world coordinate at the stance phase. Because the body motion is constrained to the vertical axis, $\boldsymbol{x}$ is induced as $\boldsymbol{x} = [0, -\boldsymbol{x}_t]$. The dynamics under the joint space observer is derived using (4.11) as

$$\boldsymbol{M}_{\mathrm{n}}\ddot{\boldsymbol{x}} =\boldsymbol{F}^{\mathrm{ref}} - \boldsymbol{F}^{\mathrm{dis}} + \hat{\boldsymbol{F}}^{\mathrm{dis}} \tag{4.13}$$

$$\boldsymbol{F}^{\mathrm{ref}} =\boldsymbol{J}_{\mathrm{aco}}^{-\mathrm{T}}\boldsymbol{\tau}^{\mathrm{ref}} \tag{4.14}$$

$$\boldsymbol{F}^{\mathrm{dis}} =(\boldsymbol{M} - \boldsymbol{M}_{\mathrm{n}})\ddot{\boldsymbol{x}} + \boldsymbol{J}_{\mathrm{aco}}^{-\mathrm{T}}\boldsymbol{g}(\boldsymbol{q}, \dot{\boldsymbol{q}}) + \boldsymbol{J}_{\mathrm{aco}}^{-\mathrm{T}}\boldsymbol{\tau}^{\mathrm{fric}} + \boldsymbol{f}_{\mathrm{k}}(\boldsymbol{q}) + \boldsymbol{F}_{e}. \tag{4.15}$$

$$\hat{\boldsymbol{F}}^{\mathrm{dis}} =\frac{g_{\mathrm{dis}}}{s + g_{\mathrm{dis}}}\boldsymbol{F}^{\mathrm{dis}}. \tag{4.16}$$

Here, $\boldsymbol{f}_{\mathrm{k}}(\boldsymbol{q})$ is $\boldsymbol{J}_{\mathrm{aco}}^{-\mathrm{T}}\boldsymbol{\tau}_{\mathrm{k}}(\boldsymbol{q})$. $\hat{\boldsymbol{F}}^{\mathrm{dis}} = \boldsymbol{J}_{\mathrm{aco}}^{-\mathrm{T}}\hat{\boldsymbol{\tau}}^{\mathrm{dis}}$ is the estimated disturbance in the workspace.Because $\hat{\boldsymbol{F}}^{\mathrm{dis}} = \boldsymbol{F}^{\mathrm{dis}}$ is satified in the passband bandwidth, the dynamics under the passband bandwidth becomes

$$\boldsymbol{M}_{\mathrm{n}}\ddot{\boldsymbol{x}} =\boldsymbol{F}^{\mathrm{ref}}. \tag{4.17}$$

The disturbance terms are rejected, and the dynamics become a simple motion equation composed of the nominalized mass and the force reference.

4.3.2 Step 2: Nominalization to a Spring-Mass System

The dynamics are nominalized as the desired spring-mass system by adding the desired virtual elastic force $\boldsymbol{F}_{\mathrm{v}}^{\mathrm{sp}}$ to the force reference $\boldsymbol{F}^{\mathrm{ref}}$ in (4.17). The error of stiffness between the real and the desired spring can be compensated. The damping of the mechanical spring is also compensated. If there is no spring on the legged robot, the actuators have to generate the total additional input $\boldsymbol{F}_{\mathrm{v}}^{\mathrm{sp}}$ in the workspace. By introducing the mechanical spring, the additional input becomes the compensation value of the spring: the stiffness error and the mechanical damping.

The motion equation with the additional virtual elastic force becomes

$$\boldsymbol{M}_{\mathrm{n}}\ddot{\boldsymbol{x}} =\boldsymbol{F}^{\mathrm{ref}} - \boldsymbol{F}_{\mathrm{v}}^{\mathrm{sp}}. \tag{4.18}$$

Assuming that the x-axis position of the tiptoe is zero, the z-axis equation of (4.18) is

$$M_{\mathrm{n}}\ddot{z}_{\mathrm{b}} = F_{\mathrm{z}}^{\mathrm{ref}} - K_{\mathrm{sp}}z, \tag{4.19}$$

where z is the z-axis displacement from the equilibrium point, or the initial posture. $F_{\mathrm{z}}^{\mathrm{ref}}$ is the z-axis force reference. The dynamics are nominalized as the desired spring-mass system. Fig. 4-4 shows the total block diagram of the nominalization control to a spring-mass system.

The additional control input for the virtual elastic force is saved by introducing the mechanical spring. The additional required force in the z-axis comparing to the case without a spring $\Delta F_{\mathrm{z}}^{\mathrm{req}}$ is concretely expressed as

$$\Delta F_{\mathrm{z}}^{\mathrm{req}} = (K_{\mathrm{sp}}^{\mathrm{real}} z + D_{\mathrm{sp}}^{\mathrm{real}} \dot{z}) - K_{\mathrm{sp}} z = \Delta K_{\mathrm{sp}} z + D_{\mathrm{sp}}^{\mathrm{real}} \dot{z}, \tag{4.20}$$

where ΔK_{sp} is $K_{\mathrm{sp}}^{\mathrm{real}} - K_{\mathrm{sp}}$. If there is not the mechanical spring, the all of virtual elastic force becomes the required additional force reference. By introducing the mechanical spring, the required additional force becomes the sum of the stiffness error term and the damping term.

4.4 Simulations Using a Spring-Mass Hopping Robot

The simulations in the case of the desired spring-mass dynamics are conducted to compare with the experiments. The parameters are set as the experimental condition to realize the similar condition to the experiments. The dynamic model in the simulations assumes a simplified mass-spring model using the experimental parameters. Compensation control is not necessary for the simulations because the dynamics are the desired ones. Two simulations are conducted. The first is the energy/phase control with the constant energy command. The hopping height command is 0.10 m from the initial height. The second is the energy/phase control with the variable energy command. The hopping height command is varied in each hopping as 0.05, 0.10, 0.15, 0.10, 0.05, and 0 m from the initial height. Like the experiments, the energy/phase control starts after t=2.5 s.

Figs. 4-6 (a) and (b) show the simulation results of the energy/phase control with the constant energy command. From the position response in Fig. 4-6 (a), the constant hopping with the desired height is observed. As shown in the plots of the amplitude, the amplitude response follows the amplitude command. Fig. 4-6 (b) shows the phase diagram. The magnitude in the stance phase is constant, and the periodic orbit is observed. This implies that the constant hopping height is attained repeatedly.

Figs. 4-7 (a) and (b) show the simulation results of the energy/phase control with the variable energy command. In the same way as the first simulations, the control of the energy is attained, the desired hopping height is realized in each step. The variable hopping height is realized using the proposed method. The phase diagram of Fig. 4-7 (b) shows the layered trajectory as the desired.

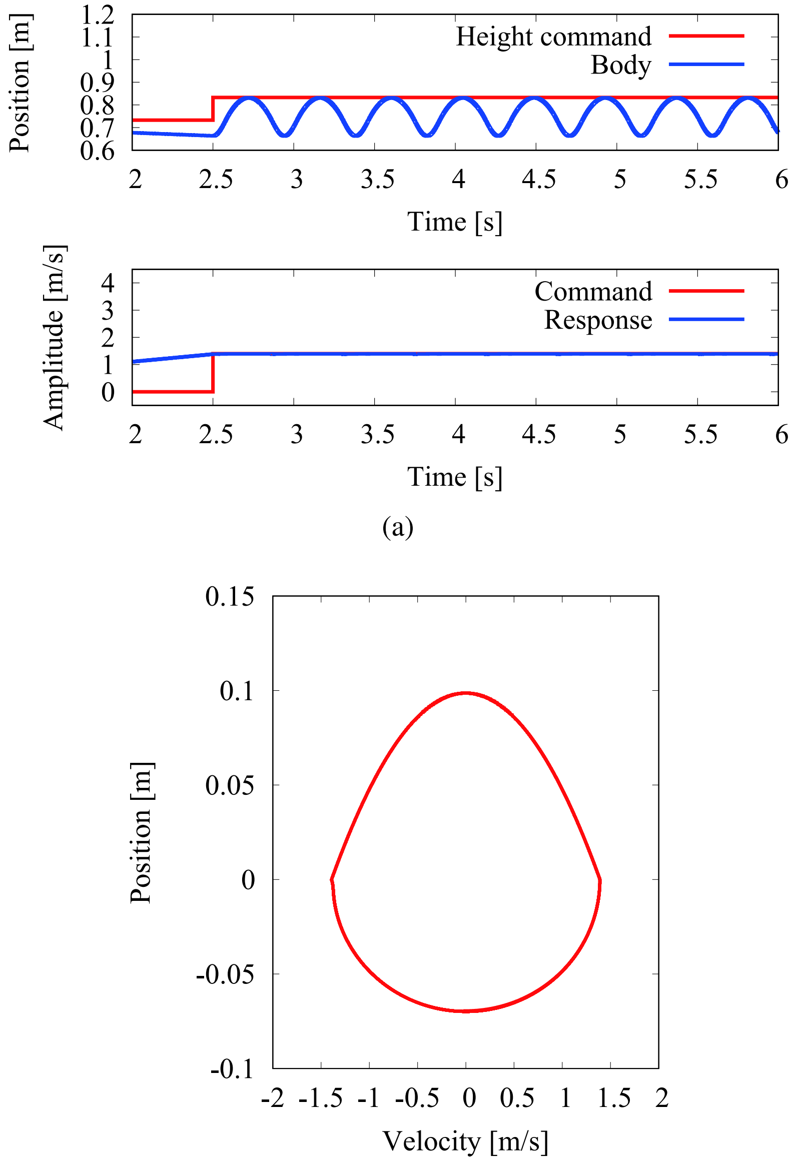

(a)

(b)

Fig. 4-6: Simulation results 1: energy/phase control with constant energy command.

4.5 Experiments

This section describes the experimental results of the proposed method. Firstly compensation controls are compared in free motions. Second, the experimental results of the proposed energy/phase control system are presented.

The experimental setup is shown in Fig. 4-8. The legged robot employs a parallel-link mechanism

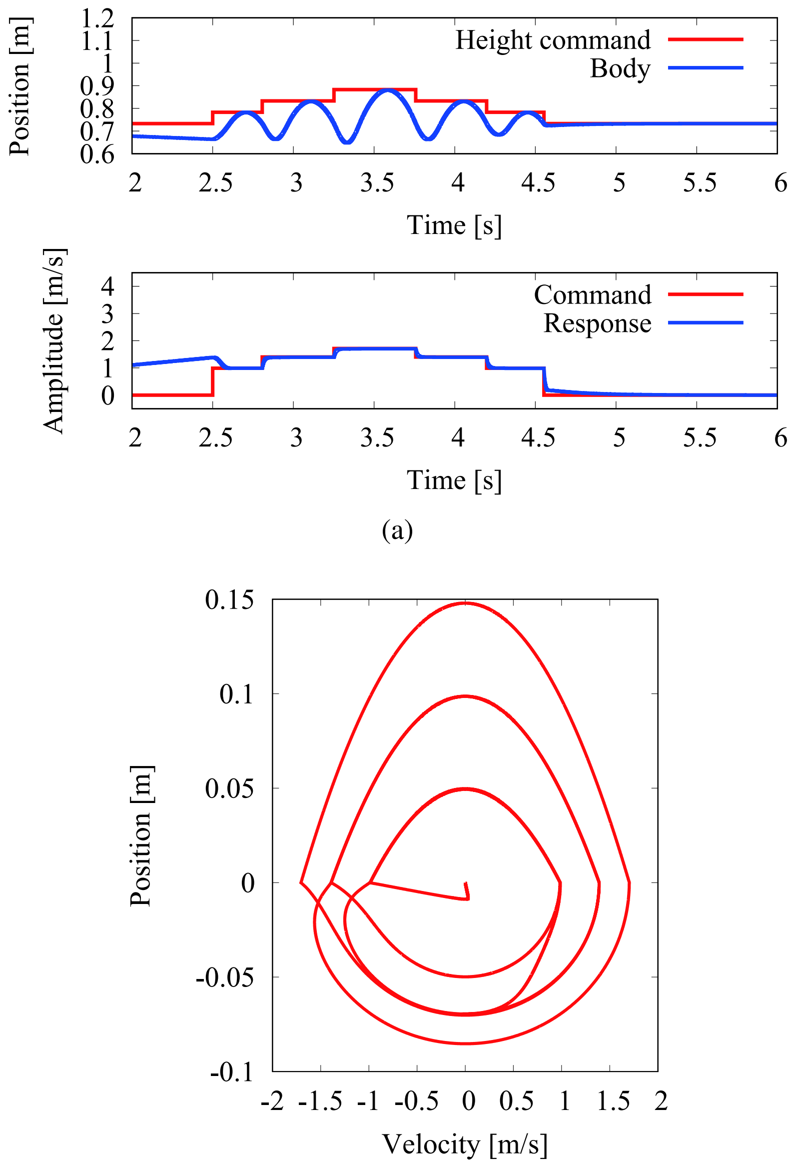

(a)

(b)

Fig. 4-7: Simulation results 2: energy/phase control with variable energy command.

with a linear leg spring. The model number of the spring is TY-21. The two actuators are placed opposite to each other. The model number of the motors is EC-i 40, 100W, 488607. As the option of the motors, the planetary gear head 6:1 is attached to each motor. The model number of the motor drivers is EPOS2 50/5. The output of the planetary gear head is connected to the harmonic gear head 21:1. The model number of the harmonic gear heads is HPG-14-21A. The total gear ratio from the motors to the output becomes 126:1. Although the total gear ratio G_r becomes high, the effect of the enlarged inertia is small

Table 4.1: Parameters of the experiments and the simulations for the hopping control.

Description	Parameter	Value
Total mass	m	6.40 kg
Stiffness of knee spring	K_{sp}	2535 N/m
Sampling time of control	T_{s}	0.150 ms
Balance height of body	L_0	0.733 m
Length of thigh and shin	l	0.45 m
Nominal torque constant	K_{tn}	0.091 Nm/A
Gear ratio of the motors	G	126
P gain of energy control	K_{p}	100
Angular frequency of phase control	ω	44.0 rad/s
Cut-off frequency of joint space observer	g_{dis}	50.0 rad/s

because of the low motor inertia J_{m}. The enlarged inertia is $J_{\mathrm{m}}G_{\mathrm{r}}^2 = 0.07\ \mathrm{kgm}^2$. On the other hand, the equivalent inertia of the nominal mass is $M_{\mathrm{n}}l^2 = 1.3\ \mathrm{kgm}^2$. Because the effect of the inertia is small, the modeling error is compensated without destabilization. The encoders are attached to the motor side of the motors. The joint angles q_1 and q_2 are calculated by dividing the measured encoder angles by the gear ratio. The model number of the encoders is MES-20-1024PE. The resolution is 1024 pulse/rotation. The encoder is also used for the measurement of the body height z_{b}. The encoder for the height measurement is attached to the top of the body. The body height z_{b} is calculated through $z_{\mathrm{b}} = z_{\mathrm{b}0} + 2l_0 \sin q_3$, where $z_{\mathrm{b}0}$ is the height of the top link for the measurement, l_0 is the link length for the measurement, q_3 is the joint angle of the encoder for the measurement. The controller is implemented using a PC with RTAI (Real Time Application Interface). The control period is 150 microseconds. The counter board is PCI-6201, and the DA board is PCI-3340. The resolution of the DA converter is 16 bit. The parameters of the experiments are shown in Table 4.1. The P gain of the energy control is tuned by observing the energy response compared to the energy command.

4.5.1 Experimental Results of Free Motion under the Compensation Controls

For experimental comparison of the compensation control, the free motions under the conventional and the proposed compensation controls are compared. After bending the leg, the acceleration reference is set at zero, and the free motion is tested. After the body position returns to the initial in the free

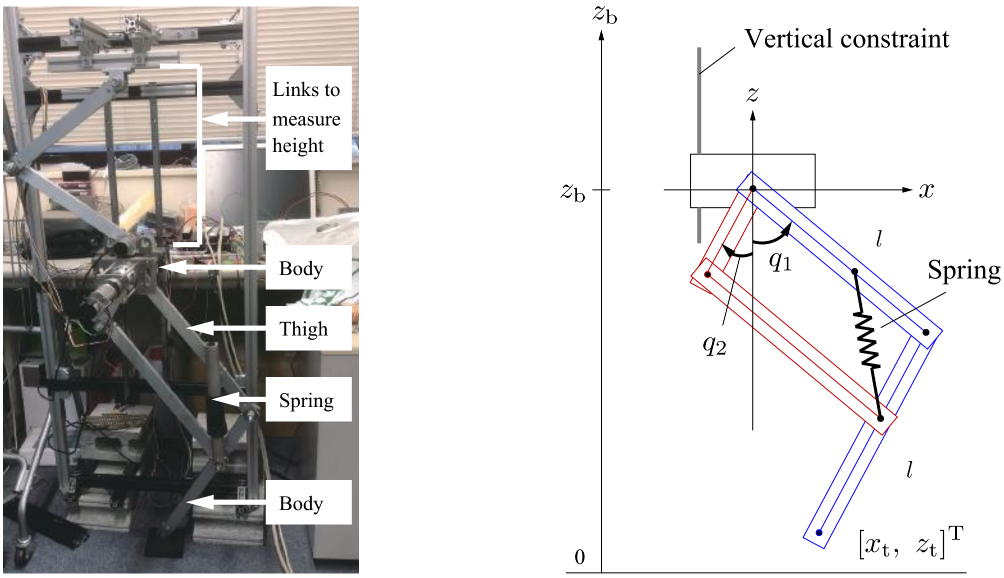

(a) (b)

Fig. 4-8: Experimental setup: (a) photo, (b) illustration of the robot.

motion, the leg is fixed by position control as the aerial phase of the hopping strategy. The four methods are tested for comparison. The first is setting zero current. The test of zero current implies the behavior without compensation control. The second is the proposed joint space observer with constant mass in the workspace (JOBp). The third is the conventional joint space observer with constant inertia (JOBc). The fourth is the conventional workspace observer (WOB).

Fig. 4-9 shows the experimental comparison of each method. In the case of the zero current, the body position does not reach the initial position. It is found out that the real leg stiffness of the robot has high friction. Compared to the real dynamics, the position responses of the compensation controls reach the initial position, and hopping motions are realized. The theoretical hopping height is 0.129 m from the initial height. Because the initial height is 0.743 m, the nearest response to the theory is the case of JOBp.

4.5.2 Experimental Results of Hopping Height Control

Two experiments are conducted in this subsection. The first is the energy/phase control with the constant energy command, or the constant hopping-height command. The hopping height command is 0.10 m from the initial height. The second is the energy/phase control with the variable energy command, or the variable hopping-height command. The hopping height command is varied in each hopping as 0.05, 0.10, 0.15, 0.10, 0.05, and 0 m from the initial height. At the initial period of the experiments

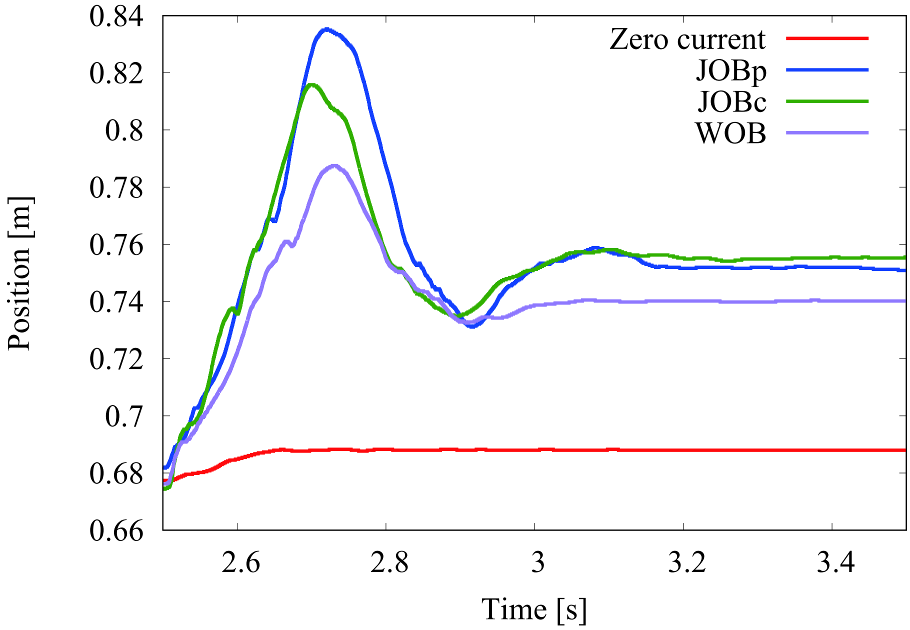

Fig. 4-9: Experimental results of free motion under the compensation controls.

(t=0–2.5 s), the leg is bent by the position control to store the energy and to make $\cos\phi$ as zero. After t=2.5 s, each control starts. In the experiments, the vibration amplitude response during the aerial phase is set held. The cut-off frequency of disturbance observer in the lower layer is tuned firstly observing the stability of the response. It is necessary that the cut-off frequency exceeds the resonance frequency to realize the nominal harmonic oscillator. The P gain of the energy control in the intermediate layer is tuned next observing the energy response compared to the energy command.

The experimental results of the energy/phase control with the constant energy command are expressed as Fig. 4-10 (a) and (b). The motion before 2.5 s is in the initial period: the body position goes down by bending the leg, and the potential energy of the spring is stored. After 2.5 s, the energy/phase control starts. The hopping height reaches the hopping command although the first hopping exceeds the desired height. The amplitude response also follows the amplitude command. The output of the proposed joint space observer becomes high around the touchdown and the liftoff. The phase diagram is drawn as Fig. 4-10 (b). Low pass filters (20 rad/s) are used to the position and the velocity responses for the clear interpretation. Fig. 4-10 (b) shows that the state repeats a certain trajectory. This implies that the constant hopping-height control is attained repeatedly by the constant-command energy/phase control.

The experimental results of the energy/phase control with variable energy command are expressed as

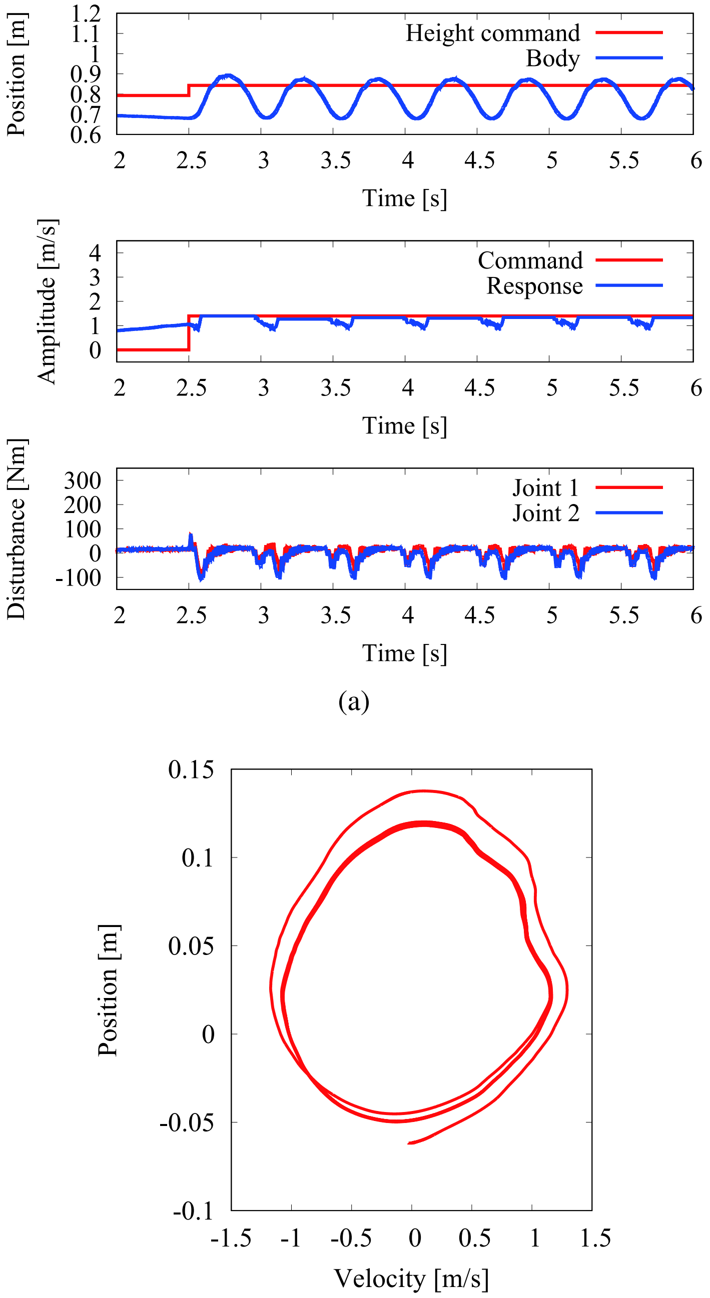

(a)

(b)

Fig. 4-10: Experimental results 1: energy/phase control with constant energy command.

Fig. 4-11 (a) and (b). The second hopping and later attain the hopping height near the height command while the height of the first hopping exceeds the command. The amplitude response follows the variable amplitude command. In the phase diagram as Fig. 4-11 (b), the layered trajectory is observed. This

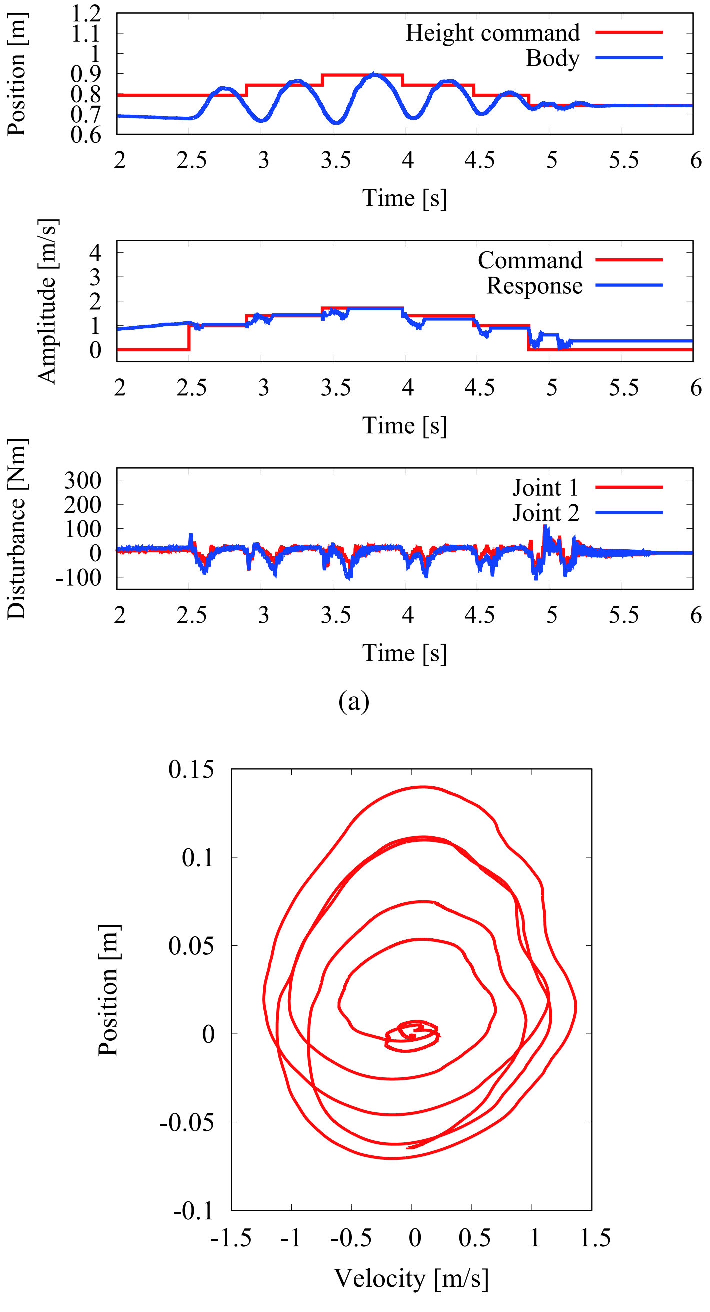

(a)

(b)

Fig. 4-11: Experimental results 2: energy/phase control with variable energy command.

result is reasonable because the step-wise energy command realizes the different one-cycle trajectories with different amplitude, or energy.

Compared to the ideal simulations, the trajectories in the phase diagrams are not smooth. The ex-

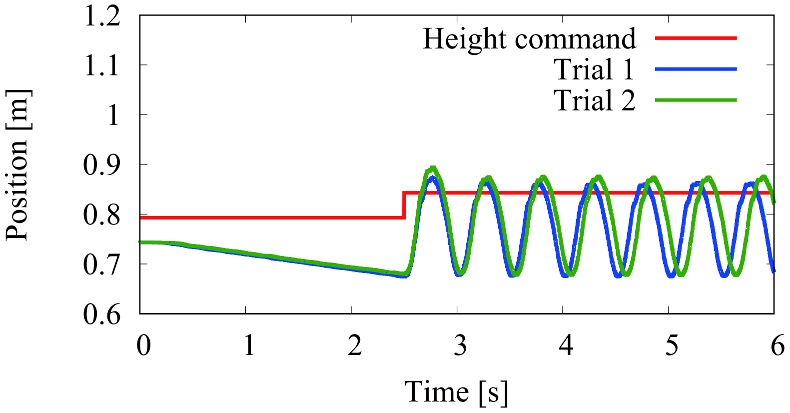

Fig. 4-12: Several results of experiments 1: position response of the constant hopping-height control.

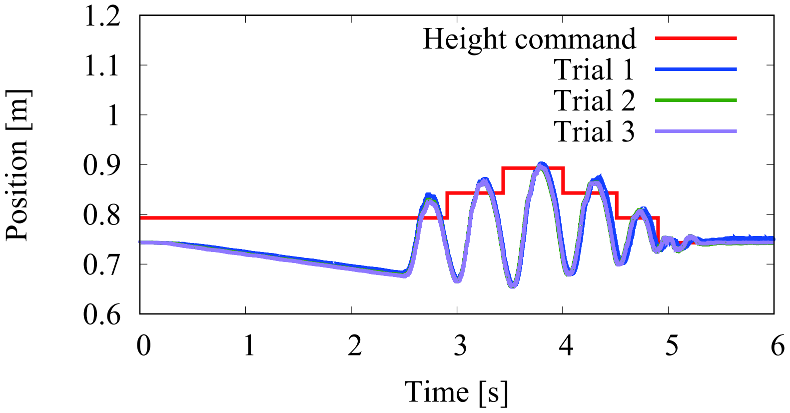

Fig. 4-13: Several results of experiments 2: position response of the variable hopping-height control.

periments have modeling errors and unknown disturbances such as friction. The proposed control has limitations. First, the disturbance observer works properly only under the bandwidth. Second, the disturbance to the body in the aerial phase cannot be compensated because the control at the aerial phase is the position control as the initial posture.

The several trials of the experimental results are compared. Figs. 4-12 and 4-13 show the several experimental results of the constant hopping and the variable hopping, respectively. It can be seen that the hopping heights are almost uniform in the respective results. While the small phase shifts of the position response are observed, the difference of the hopping heights is one factor. Because the higher hopping takes more time to land, the periods shift differently.

4.6 Summary

This chapter described extending the application of the energy/phase control to hopping-height control with a one-leg robot. This chapter firstly discussed the hopping-height control with a simple spring-mass robot applying the energy/phase control. The energy is controlled in the stance phase so that the mechanical energy becomes the potential energy at the desired height. The simulations with a simple spring-mass robot were conducted. The constant height hopping and the variable height hopping were realized. Applying the nominalizing control in Chapter 3, the experiments using a one-leg robot with a mechanical spring were also conducted. The constant height hopping and the variable height hopping were confirmed experimentally.

Chapter 5

Biped Walking Control Based on Energy/Phase Control

5.1 Introduction

Energy-efficient biped walking is an important problem because a battery on the robot has a limitation of energy. Even if the difference in energy efficiency per one step is small, the energy consumption of the total steps makes a large difference. This chapter deals with energy-efficient biped walking control.

The approach of this chapter is the oscillation of a linear inverted pendulum by the energy/phase control. Biped walking control often employs a linear inverted pendulum model. The energy/phase control enables an energy-efficient oscillation. The energy/phase control for a linear inverted pendulum is induced using the duality of trigonometric functions and hyperbolic functions. Section 5.2 describes the model of the biped robot. In Section 5.3, the control system of the biped robot is explained. In Section 5.4, energy/phase control of a linear inverted pendulum is proposed. Section 5.5 deals with the induction of feasible walking commands. Simulations and experiments are conducted and shown in Sections 5.6 and 5.7, respectively. Finally, Section 5.8 concludes this chapter.

5.2 Energy/Phase Control of a Linear Inverted Pendulum

A linear inverted pendulum model is often used for biped walking control as Fig. 5-1. S is the stride of the walking. This section describes the proposed energy/phase control for a linear inverted pendulum. Energy and phase of the linear inverted pendulum are induced in Subsection 5.2.1. The motion equation

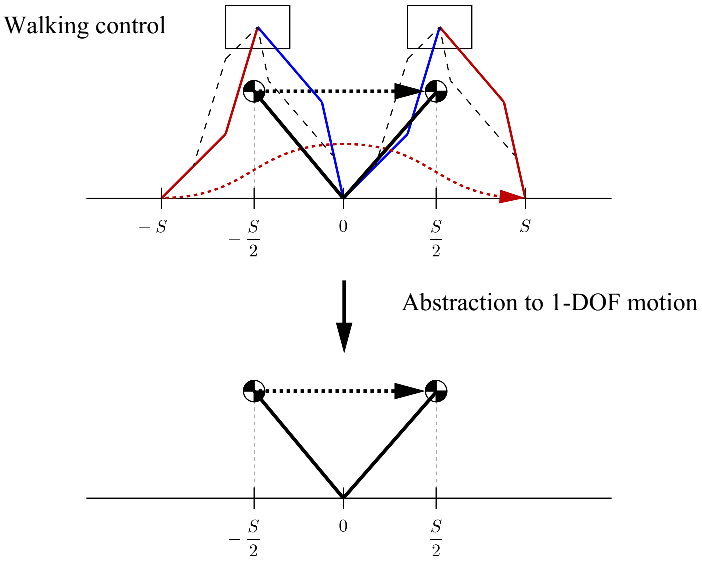

Fig. 5-1: Abstracted one-degree-of-freedom model of a biped walking robot.

of the linear inverted pendulum is transformed using the energy and the phase in Subsection 5.2.2. In Subsection 5.2.3, the energy/phase control is explained. Based on the motion equation of energy and phase, the dynamics under the energy/phase control is induced. Subsection 5.2.4 explains the simulations using the simple linear inverted pendulum.

5.2.1 Energy and Phase of Linear Inverted Pendulum

A linear inverted pendulum is often used as a simplified model of a biped walking robot. Energy and phase of the linear inverted pendulum are defined based on the motion equation. Especially, the energy of the linear inverted pendulum is called as “orbital energy” in biped walking.

The motion equation of the linear inverted pendulum is written using the body-mass position x, the body-mass height z, the control input in the acceleration dimension F, and the gravitational acceleration g as

$$\ddot{x} - \omega_{\mathrm{c}}^2 x = F, \tag{5.1}$$

$$\omega_{\mathrm{c}} = \sqrt{g/z}. \tag{5.2}$$

Here, ω_{c} is the equivalnet angular frequency of the linear inverted pendulum. Orbital energy is popularly used for a linear inverted pendulum model of a biped walking robot [103]. The orbital energy E is

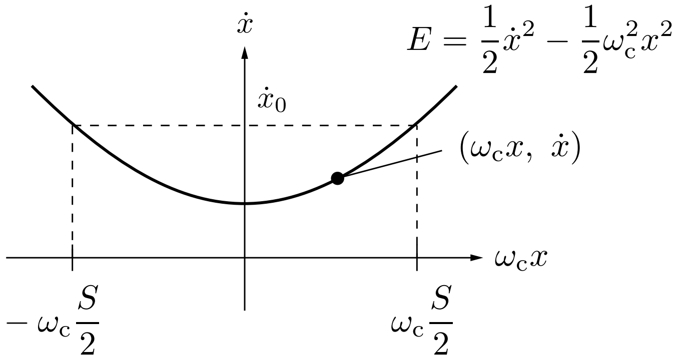

Fig. 5-2: Phase diagram of a linear inverted pendulum.

expressed using the angular frequency as

$$E = \frac{1}{2}\dot{x}^2 - \frac{1}{2}\omega_c^2 x^2. \tag{5.3}$$

Different from the mechanical energy of a harmonic oscillator, the sign of the potential energy term in the orbital energy is negative. Referring the work by Kajita et al. [114], $E > 0$ is necessary for that the biped body goes through the point $x = 0$. $E = 0$ reporesents the equilibrium state ($x = 0$ and $\dot{x} = 0$). When $E < 0$, the biped body cannot pass the point $x = 0$. The equation of the orbital energy (5.3) can be transformed to a normal form of a hyperbolic function as

$$\frac{\dot{x}^2}{2E} - \frac{(\omega_c x)^2}{2E} = 1. \tag{5.4}$$

Using characteristic of the normal form of a hyperbolic function, $\dot{x}$ and $\omega_c x$ can be expressed in terms of the parametric representation. The parametric reprensentation of $(\dot{x}, \omega_c x)$ is written using phase parameter ϕ as

$$(\dot{x}, \omega_c x) = (\sqrt{2E}\cosh\phi, \sqrt{2E}\sinh\phi). \tag{5.5}$$

In order to use the phase for control, it is necessary to calculate the value of the phase. The phase ϕ can be calculated using $(\dot{x}, \omega_c x)$ as

$$\begin{aligned}\phi &= \operatorname{atanh}(\tanh\phi) = \operatorname{atanh}\left(\frac{\sinh\phi}{\cosh\phi}\right) \\ &= \operatorname{atanh}\left(\frac{\omega_c x}{\dot{x}}\right).\end{aligned} \tag{5.6}$$

5.2.2 Dynamics in terms of Energy and Phass

The motion equation of a linear inverted pendulum is transformed using the energy E and the phase ϕ.

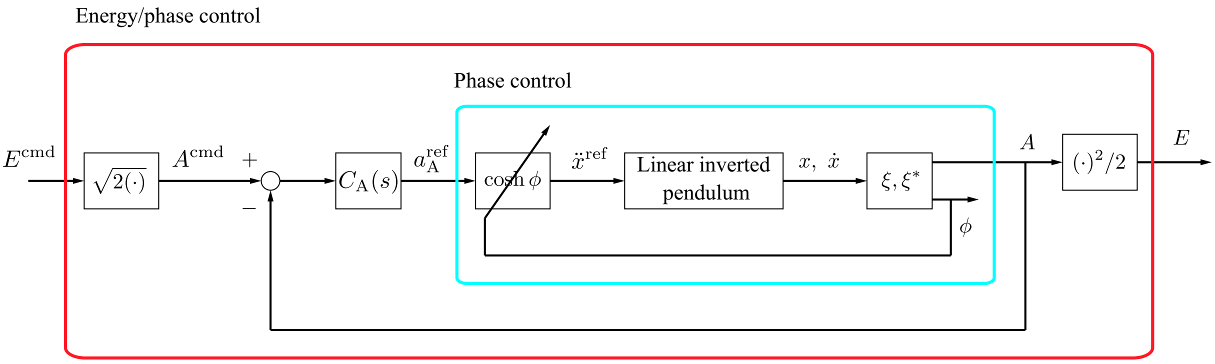

Fig. 5-3: Block diagram of the energy/phase control for a linear inverted pendulum.

The motion equation (5.1) is transformed using $\xi = \dot{x} + j\omega x$ and $\xi^* = \dot{x} - j\omega x$ as

$$\frac{d}{dt}\left(\frac{\xi + \xi^*}{2}\right) - \omega\frac{\xi - \xi^*}{2j} = F. \tag{5.7}$$

The motion equation is expressed based on (ξ, ξ^*) from $(\dot{x}, \omega_{\mathrm{c}} x)$. The relation between $(\xi,\ \xi^*)$ and $(E,\ \phi)$ is induced using (5.5) as

$$\xi = \dot{x} + j\omega x = \sqrt{2E}(\cosh\phi + j\sinh\phi) \tag{5.8}$$

$$\xi^* = \dot{x} - j\omega x = \sqrt{2E}(\cosh\phi - j\sinh\phi), \tag{5.9}$$

Substituting the relation (5.8) and (5.9) to the transformed motion equation (5.7), the motion equation in terms of energy and phase is obtained as

$$\frac{d}{dt}\left(\sqrt{2E}\cosh\phi\right) - \omega\sqrt{2E}\sinh\phi = F. \tag{5.10}$$

5.2.3 Energy/Phass Control

This subsection describes the proposed energy/phase control for hyperbolic oscillation. The energy/phase control is composed of the energy control and the phase control. The total block diagram is shown in Fig. 5-3. The energy control is in the outer loop, and the phase control is in the inner loop. First, the dynamics under the phase control are induced. Next, the whole energy/phase control system is described.

Dynamics under Phase Control

The phase control oscillates a linear inverted pendulum in response to the phase of the body. Concretely, the phase of the hyperbolic control input is determined so as to synchronize with the phase of the

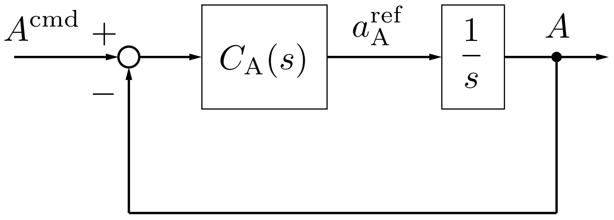

Fig. 5-4: Block diagram of energy control for a linear inverted pendulum.

body. The control input of the phase control is expressed in the form of an equation as

$$F = a_{\mathrm{A}}^{\mathrm{ref}} \cosh\phi. \tag{5.11}$$

$a_{\mathrm{A}}^{\mathrm{ref}}$ is the actuation amplitude of the energy/phase control. For a simple expression of the dynamics, an energy equivalent variable $A(t)$ is introduced as

$$A(t) = \sqrt{2E(t)}. \tag{5.12}$$

Also, the phase ϕ can be expressed as

$$\phi = \omega_{\mathrm{c}} t + \phi_0, \tag{5.13}$$

where ϕ_0 is the initial phase.

Substituting these variables F, A, and ϕ ((5.11), (5.12) and (5.13)) to the dynamics of (5.1), the dynamics under the phase control is expressed as

$$\begin{aligned} \frac{d}{dt}\left(A(t)\cosh(\omega_{\mathrm{c}}t+\phi_0)\right) - \omega A(t)\sinh(\omega_{\mathrm{c}}t+\phi_0) \\ = a_{\mathrm{A}}^{\mathrm{ref}} \cosh(\omega_{\mathrm{c}}t+\phi_0). \end{aligned} \tag{5.14}$$

Trasforming (5.14), the dynamics under the phase control is simplified as

$$\dot{A}(t) = a_{\mathrm{A}}^{\mathrm{ref}}. \tag{5.15}$$

The derivative of the energy equivalent variable is equal to the amplitude of the control input. The dynamics under the phase control are expressed as a simple equation.

Energy/Phase Control System

In the outer loop of the energy/energy control, the energy is controlled by tuning the amplitude of the control input $a_{\mathrm{A}}^{\mathrm{ref}}$. Even if $a_{\mathrm{A}}^{\mathrm{ref}}$ is time-variant, the dynamics (5.15) can be induced in the same manner.

The dynamics of energy control can be expressed in Laplace space as

$$A(s) = \frac{1}{s} a_{\mathrm{A}}^{\mathrm{ref}}(s). \tag{5.16}$$

Based on the dynamics (5.16), a feedback control system is designed. The block diagram of the energy control is drawn in Fig. 5-4. When P controller with gain K_{p} is assumed as

$$a_{\mathrm{A}}^{\mathrm{ref}} = K_{\mathrm{p}}(A^{\mathrm{cmd}} - A), \tag{5.17}$$

the input in implementation is expressed as

$$\ddot{x}^{ref} = K_{\mathrm{p}}(A^{\mathrm{cmd}} - A)\cos\phi. \tag{5.18}$$

The transfer function from the energy-equivalent command A^{cmd} to the output A becomes a first-order lag system as

$$\frac{A}{A^{\mathrm{cmd}}} = \frac{K_{\mathrm{p}}}{s + K_{\mathrm{p}}}. \tag{5.19}$$

From the transfer function, it can be said that the cut-off frequency of the response is equal to the proportional gain K_{p}. The higher the gain K_{p} is, the higher cut-off frequency the energy control can attain.

Table 5.1 summarizes the energy/phase control for a linear inverted pendulum in this Chapter and the energy/phase control for a harmonic oscillator in Chapter 2. Although the respective motion equation is different, especially the sign of the coefficient of x, the dynamics of energy become equal under the phase control.

The negative energy exists in the case of a linear inverted pendulum, different from a harmonic oscillator. The negative energy implies that the biped body cannot pass the point $x = 0$. Keeping the negative energy means that the body diverges to the netgative direction. Because the energy immediately after switching the stance leg is negative, it is desirable to increase the energy to more than zero as soon as possible. From this viewpoint, it is desirable to increase the energy gain. On the other hand, the higher gain tends to make the control system unstable owing to the limitation of the hardware. It is necessary to tune the adequate gain.

5.2.4 Phase Diagram

The energy/phase control is developed from the viewpoint of phase diagram. The phase diagram shows the motion in terms of the coordinate whose axes are the position and the velocity. Dynamics

Table 5.1: Duality of energy/phase control for a harmonic oscillator and a linear inverted pendulum.

Description	Harmonic oscillator	Linear inverted pendulum
Motion equation	$\ddot{x} + \omega^2 x = F$	$\ddot{x} - \omega_{\mathrm{c}}^2 x = F$
Angular frequency	$\omega = \sqrt{k/m}$	$\omega_{\mathrm{c}} = \sqrt{g/z}$
Energy	$E = \frac{1}{2}(\dot{x}^2 + \omega^2 x^2)$	$E = \frac{1}{2}(\dot{x}^2 - \omega_{\mathrm{c}}^2 x^2)$
Constant-energy surface	$\dot{x}^2 + \omega^2 x^2 = 2E$ (Circle)	$\frac{\dot{x}^2}{2E} - \frac{\omega_{\mathrm{c}}^2 x^2}{2E} = 1$ (Hyperbola)
Parameter expression of constant-energy surface	$(\dot{x}, \omega x) =$ $(\sqrt{2E}\cos\phi, \sqrt{2E}\sin\phi)$	$(\dot{x}, \omega_{\mathrm{c}} x) =$ $(\sqrt{2E}\cosh\phi, \sqrt{2E}\sinh\phi)$
Vibration phase	$\phi = \tan^{-1}(\omega x/\dot{x})$	$\phi = \tanh^{-1}(\omega_{\mathrm{c}} x/\dot{x})$
Vibration amplitude	$A = \sqrt{2E}$	$A = \sqrt{2E}$
Motion equation of energy and phase	$\frac{d}{dt}\left(\sqrt{2E}\cos\phi\right) + \omega\sqrt{2E}\sin\phi$ $= F$	$\frac{d}{dt}\left(\sqrt{2E}\cosh\phi\right) - \omega_{\mathrm{c}}\sqrt{2E}\sinh\phi$ $= F$
Control input of phase control	$F = a_{\mathrm{A}}^{\mathrm{ref}}\cos\phi$	$F = a_{\mathrm{A}}^{\mathrm{ref}}\cosh\phi$
Dynamics of amplitude under phase contorl	$\dot{A} = a_{\mathrm{A}}^{\mathrm{ref}}$	$\dot{A} = a_{\mathrm{A}}^{\mathrm{ref}}$
Control input of energy/phase contorl	$F = K_{\mathrm{p}}(A^{\mathrm{cmd}} - A)\cos\phi$	$F = K_{\mathrm{p}}(A^{\mathrm{cmd}} - A)\cosh\phi$

without and with the energy/phase control are visualized in terms of the position-velocity coordinate. Concretely, vector fields in the position-velocity coordinate are visualized. In the vector fields, the velocity vector at each grid point is drawn. By tracing the velocity vectors, the motion can be predicted. It is possible to judge whether the motion will stabilize or unstabilize.

Firstly, a vector field of a harmonic oscillator is discussed. The state (x, y) is defined concretely as $(x, \dot{x})$. The velocity vector (u, v) of the state (x, y) in a harmonic oscillator is expressed as

$$u = y \tag{5.20}$$

$$v = -\omega^2 x. \tag{5.21}$$

Using (5.20) and (5.21), the vector fields are drawn as Fig. 5-5. In Fig. 5-5, periodic motions are observed from the vectors. In the case of a linear inverted pendulum, the velocity vector becomes

$$u = y \tag{5.22}$$

$$v = \omega^2 x. \tag{5.23}$$

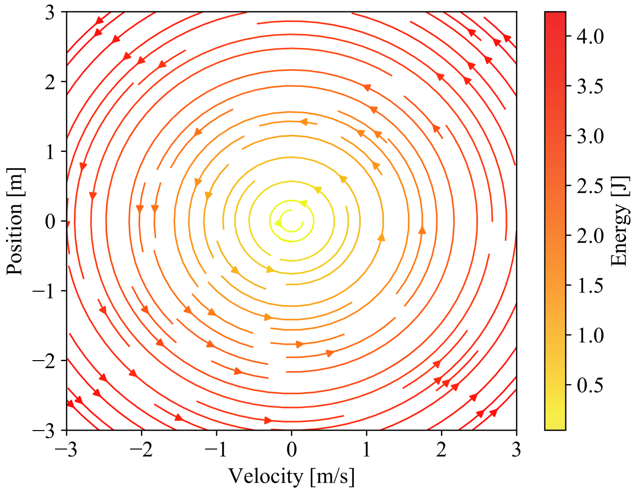

Fig. 5-5: Phase diagram of a harmonic oscillator.

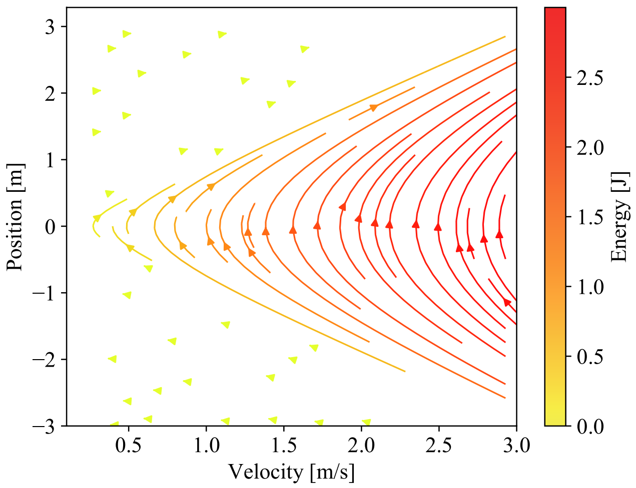

Fig. 5-6: Phase diagram of a linear inverted pendulum.

The vector fields are drawn from (5.22) and (5.23) as Fig. 5-6. Different from Fig. 5-5, the motion diverges if there are no additional limitations such as position limit or velocity limit. In the case of biped walking, the motion does not unstabilize because the position is limited in one walking phase.

Next, dynamics with energy/phase control is discussed. The vector fields of a harmonic oscillator with

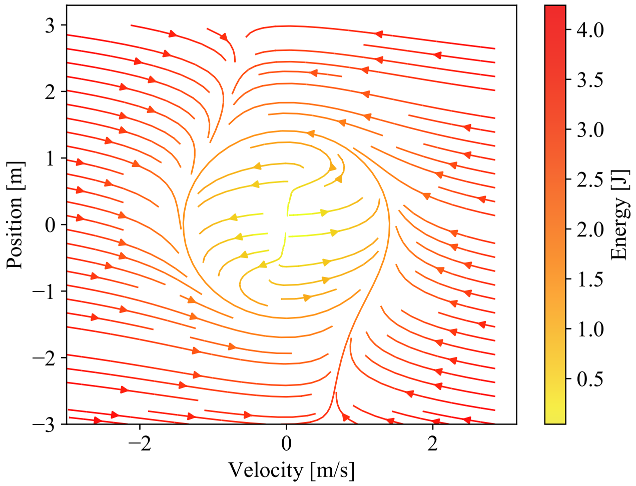

Fig. 5-7: Phase diagram of a harmonic oscillator with the energy/phase control.

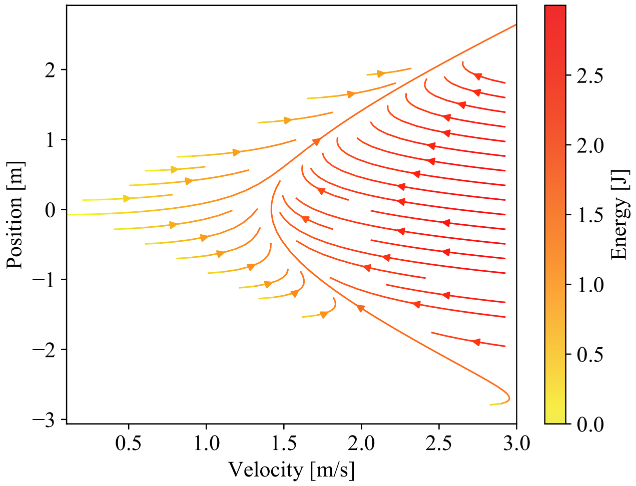

Fig. 5-8: Phase diagram of a linear inverted pendulum with the energy/phase control.

the energy/phase control are drawn using the velocity vecotr as

$$u = y \tag{5.24}$$

$$v = -\omega^2 x + K_{\mathrm{p}}(A^{\mathrm{cmd}} - A)\cos\phi. \tag{5.25}$$

The induced vector fields are shown in Fig. 5-7. The motion trajectory converges to the circular constant-energy surface. In the case of a linear inverted pendulum with the energy/phase control, the velocity

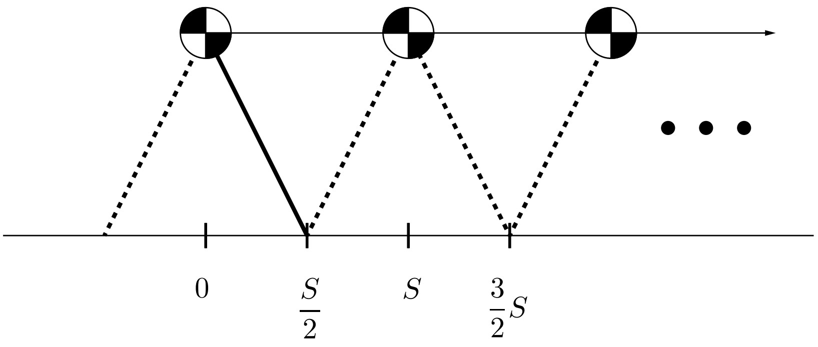

Fig. 5-9: Simulation setup: simplified walking model using a linear inverted pendulum.

vector is derived as

$$u = y \tag{5.26}$$

$$v = \omega^2 x + K_{\mathrm{p}}(A^{\mathrm{cmd}} - A)\cosh\phi. \tag{5.27}$$

The vector fields are shown in Fig. 5-8. In this case the motion trajectory converges to the hyperbolic constant-energy surface. It is confirmed that the energy/phase control attracts the motion to its dynamics with constant energy.

5.2.5 Simulations Using Simple Model

In order to confirm the appropriateness of the proposed energy/phase control, simulations using a simple inverted linear pendulum are conducted firstly.

Fig. 5-9 shows the setup of the simulations. The simulations assume the simplified walking model using a linear inverted pendulum. The initial position of the body mass is zero. If the body mass proceeds S [m], the position of stance leg x_{sp} is switched to the next step. The initial position of the stance tiptoe is $S/2$, and the step width is S. Using equations, the dynamics of the simple simulations is expressed as

$$\ddot{x} = \omega_{\mathrm{c}}^2(x - x_{\mathrm{sp}}) + F. \tag{5.28}$$

The stance tiptoe x_{sp} changes by S when $x - x_{\mathrm{sp}}$ is greater than $S/2$, and x_{sp} changes by $-S$ when $x - x_{\mathrm{sp}}$ is lower than $-S/2$,

Using the dynamics, two simulations are conducted. The first is constant-speed walking. The energy/phase control is implemented, and the energy command is set as a certain value. The energy command is determined so that the velocity at switching the legs is 1 m/s. The second is variable-speed

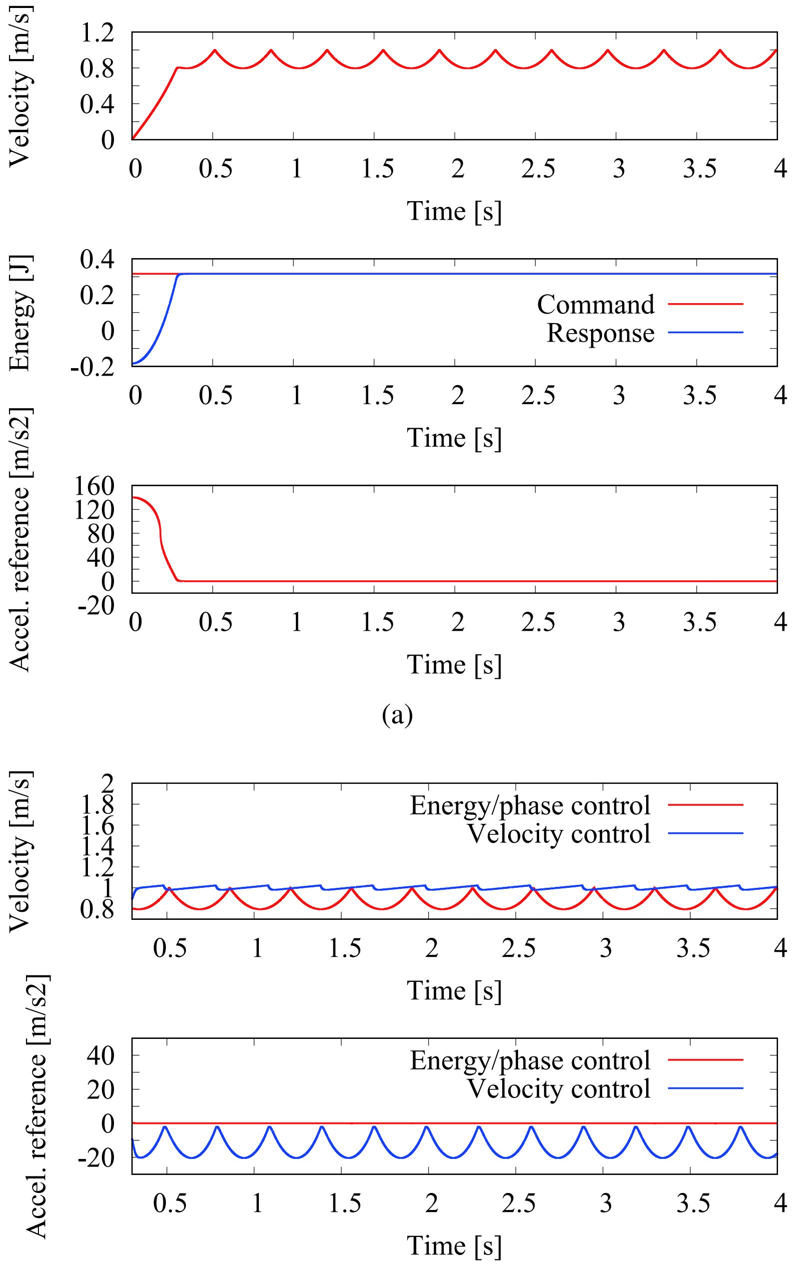

(a)

(b)

Fig. 5-10: Constant-command simulation results of energy/phase control using the linear inverted pendulum: (a) time-series responses, (b) comparison with velocity control

walking. The energy command is varied so that the velocity at switching the legs becomes 1.0, 1.2, and 1.4 m/s. The command is varied at the third, the fifth, and the seventh steps.

Fig. 5-10 shows the simulation results of energy/phase control using the simple linear inverted pendu-

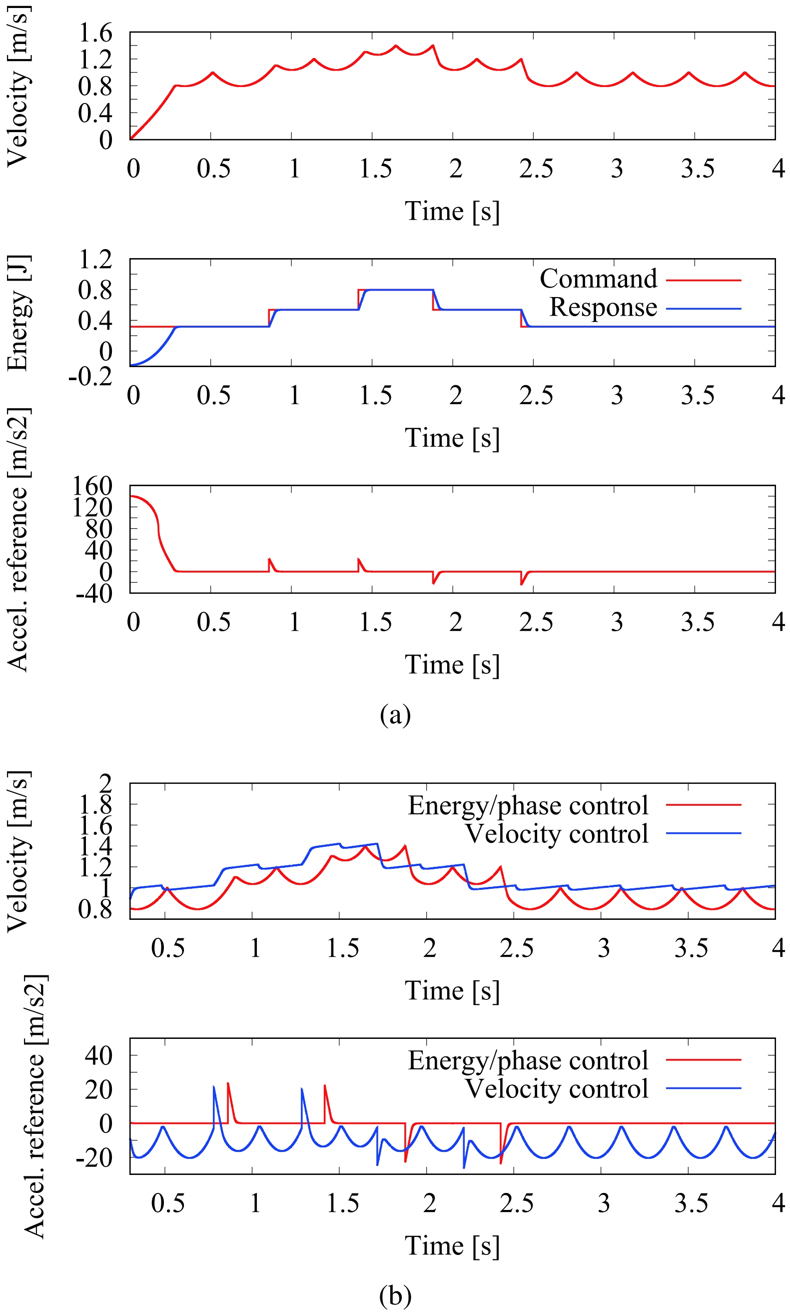

(a)

(b)

Fig. 5-11: Stepwise-command simulation results of energy/phase control using the linear inverted pendulum: (a) time-series responses, (b) comparison with velocity control

lum, especially the constant-speed walking. Fig. 5-10 (a) shows the time-series results of the constant-speed walking. The position response is the response of the body mass in the support coordinate. The position and the velocity change periodically, which indicates that periodic constant-speed walking is attained. The energy response follows the energy command. Fig. 5-10 (b) shows the phase diagram of the constant-speed walking. The trajectory converges to the one hyperbolic trajectory. This result also denotes that periodic walking is attained. The results of the energy consumption and the current consumptions are as follows. The energy consumptions of the conventional velocity control and the proposed energy/phaes control are 27.24 mWh and 2.91 mWh, respectively. The current consumptions of the velocity control and the energy/phaes control are 3.55 mAh and 0.86 mAh, respectively. The proposed energy/phase control is more efficient in terms of both the energy consumption and the current consumption.

Fig. 5-11 presents the results of the variable-speed walking. The energy command and response reflect the change of the desired speed and its response. The energy response follows the staircase energy command. The velocity response also shows the staircase change. Fig. 5-11 (b) is the phase diagram of the variable-speed walking. The three-step trajectory is observed. The respective velocity at switching shows 1.0, 1.2, and 1.4 m/s as the desired walking speed. The results of the energy consumption and the current consumptions are as follows. The energy consumptions of the velocity control and the energy/phaes control are 33.17 mWh and 8.46 mWh, respectively. The current consumptions of the velocity control and the energy/phaes control are 3.87 mAh and 1.39 mAh, respectively. The variable-speed control by the proposed energy/phase control is also more efficient in terms of both the energy consumption and the current consumption.

Figs. 5-12 (a) and (b) show the phase diagrams of the energy/phase control of the constant-speed walking and the variable-speed walking. Fig. 5-12 (a) shows the steady hyperbolic trajectory, and indicates that the periodic constant-speed walking is attained. Fig. 5-12 (b) shows the layered hyperbolic trajectory, and indicates that the variable-speed walking is attained.

5.3 Model of Biped Robot

A parallel-link biped robot is assumed for verification of the proposed method. The merit of a parallel-link legged robot is that the weight concentrates on the body. The dynamics become similar to the one of a linear inverted pendulum.

Fig. 5-13 shows the initial condition of the biped simulations and experiments. Although Fig. 5-13 (a) is an image of the actual COG, it is assumed that the mass is concentrated at the origin of the base as Fig. 5-13 (b). The first reason is that the actual COG is near the body because the heavy components

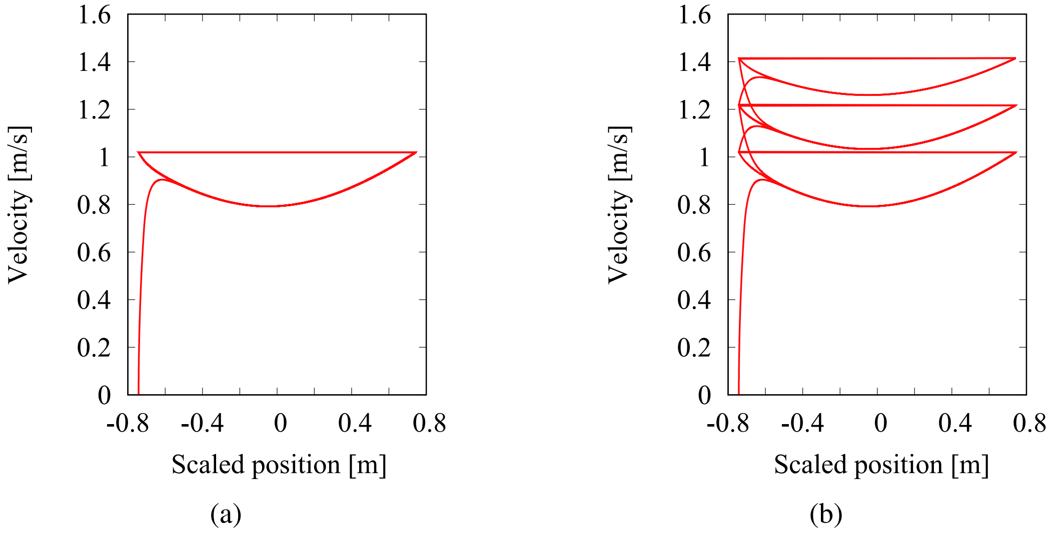

Fig. 5-12: Phase diagrams of energy/phase control using the linear inverted pendulum: (a) constant-speed walking, (b) variable-speed walking.

are located on the body in the parallel-link mechanism. The second reason is that the control system in Chapter 3 nominalizes the dynamics as a body-mass system, and the dynamics error is compensated. In Fig. 5-13, the right leg is drawn using the red lines, and the left leg is drawn using the blue lines. S is the stride length, and Z_{c} is the height of the concentrated mass. The position of the body $(x_{\mathrm{b}},\ z_{\mathrm{b}})$ in Fig. 5-13 (a) is determined to satisfy that

- the concentrated mass is initially located $(0, Z_{\mathrm{c}})$,
- the left tiptoe is located at $(\frac{S}{2}, 0)$ and the right tiptoe is located at $(-\frac{S}{2}, 0)$.

The position of the body $(x_{\mathrm{b}},\ z_{\mathrm{b}})$ in Fig. 5-13 (b) is induced from the kinematic relations of Fig. 5-13 (b).

Next, the kinematics and the dynamics are explained.

5.3.1 Kinematics

Fig. 5-14 illustrates the kinematics of the left leg. The degree of freedom of the motion is 2D, and the body is located at $(x_{\mathrm{b}}, z_{\mathrm{b}})$ in the world coordinate. The parallel-link leg is composed of the four links. The angle of the bar 1 is q_1, and the angle of the bar 3 is q_2. The tiptoe position of the left leg in the

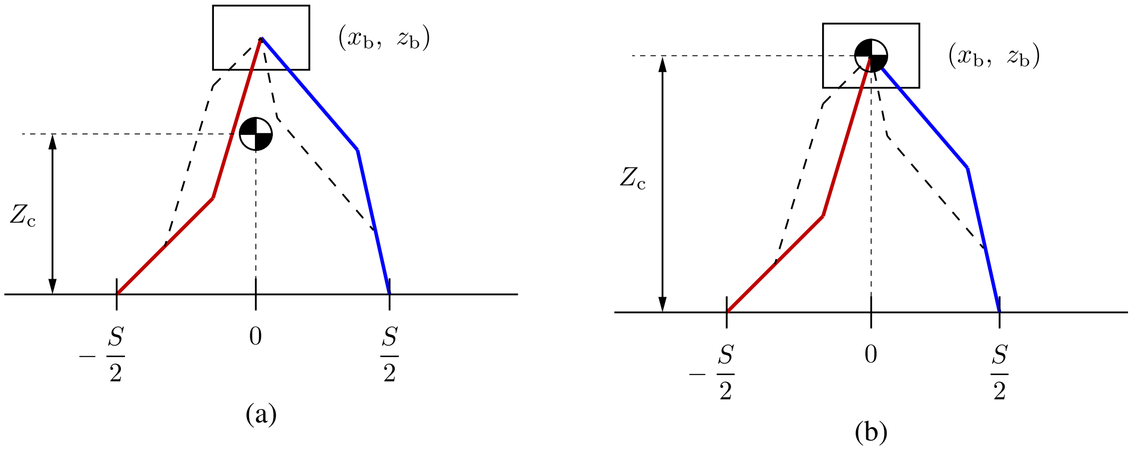

Fig. 5-13: Initial condition: (a) the actual COG, (b) the approximated COG.

world coordinate ${}^{\rm w}\boldsymbol{x}_{\rm tL} = ({}^{\rm w}x_{\rm tL}, {}^{\rm w}z_{\rm tL})$ is calculated as

$$ {}^{\rm w}x_{\rm tL} = x_{\rm b} + l_1 \sin(q_1) - l_2 \sin(q_2) \tag{5.29}$$

$$ {}^{\rm w}z_{\rm tL} = z_{\rm b} - l_1 \cos(q_1) - l_2 \cos(q_2). \tag{5.30}$$

In the same manner, the tiptoe position of the right leg ${}^{\rm w}\boldsymbol{x}_{\rm tR}$ can be calculated using q_3 and q_4. In the case of the right leg, the angle of the bar 1 is q_3, and the angle of the bar 3 is q_4.

Using the generalized position vector $\boldsymbol{q}_{\rm e} = (\boldsymbol{x}_{\rm b},\ \boldsymbol{q})$, where $\boldsymbol{x}_{\rm b} = (x_{\rm b},\ z_{\rm b})$ and $\boldsymbol{q}_{\rm b} = (q_1,\ q_2,\ q_3,\ q_4)$, the Jacobian matrix of each tiptoe in the world coordinate $\boldsymbol{J}_{\rm acoLw}$ and $\boldsymbol{J}_{\rm acoRw}$ can be calculated as

$$ \boldsymbol{J}_{\rm acoLw} = \frac{\partial^{\rm w}\boldsymbol{x}_{\rm tL}}{\partial \boldsymbol{q}_{\rm e}} \tag{5.31}$$

$$ \boldsymbol{J}_{\rm acoRw} = \frac{\partial^{\rm w}\boldsymbol{x}_{\rm tR}}{\partial \boldsymbol{q}_{\rm e}}. \tag{5.32}$$

5.3.2 Dynamics

The dynamics of the robot is induced from Lagrange motion equation. Assuming that $\mathcal{L}$ is Lagrangian, and $\boldsymbol{\tau}^{\rm ref} = (\tau_1^{\rm ref},\ \tau_2^{\rm ref},\ \tau_3^{\rm ref},\ \tau_4^{\rm ref})$ is the vector of the torque reference, the Lagrange motion equation is concretely written as

$$ \frac{d}{dt}\left(\frac{\partial \mathcal{L}}{\partial \dot{\boldsymbol{q}}_{\rm e}}\right) - \frac{\partial \mathcal{L}}{\partial \boldsymbol{q}_{\rm e}} = \boldsymbol{\tau}^{\rm ref} + \boldsymbol{J}_{\rm acow}\boldsymbol{F}^{\rm ext}, \tag{5.33}$$

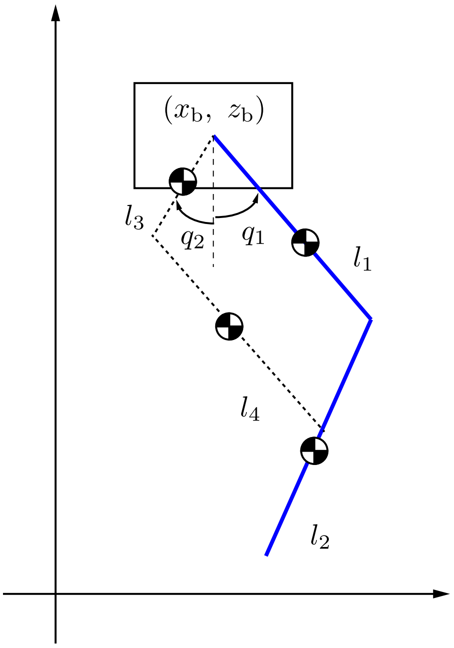

Fig. 5-14: Kinematics of the left leg.

where $\boldsymbol{J}_{\mathrm{acow}}$ is the Jacobian matrix in the world coordinate. The induced motion equation is a floating-base motion equation as

$$\begin{bmatrix} \boldsymbol{H}_{\mathrm{b}} & \boldsymbol{H}_{\mathrm{bm}} \\ \boldsymbol{H}_{\mathrm{bm}} & \boldsymbol{H}_{\mathrm{m}} \end{bmatrix} \begin{bmatrix} \ddot{\boldsymbol{x}}_{\mathrm{b}} \\ \ddot{\boldsymbol{q}} \end{bmatrix} + \begin{bmatrix} \boldsymbol{g}_{\mathrm{b}} \\ \boldsymbol{g}_{\mathrm{m}} \end{bmatrix} = \begin{bmatrix} 0 \\ \boldsymbol{\tau}^{\mathrm{ref}} \end{bmatrix} + \boldsymbol{J}_{\mathrm{acoL}}^{T} \boldsymbol{F}_{\mathrm{eL}} + \boldsymbol{J}_{\mathrm{acoR}}^{T} \boldsymbol{F}_{\mathrm{eR}}. \tag{5.34}$$

Here, $\boldsymbol{H}$ is the inertia matrix. The subscript b means the base, the subscript m means the motor-side angle, and the subscript bm means the interference term of the base and the motor-side angle. $\boldsymbol{g}$ is the vector of the nonlinear term. $\boldsymbol{F}_{\mathrm{eL}}$ and $\boldsymbol{F}_{\mathrm{eR}}$ are the reaction force from the environment to the left leg and the right leg.

5.4 Control System for Biped Robot

This section describes the control system to apply the proposed energy/phase control to a biped robot. The control system is constructed based on the controls of the body and the swing leg.

Fig. 5-15 shows the whole block diagram based on the body and the swing leg. The detail is explained as follows.

Direct Kinematics

The direct kinematics in the control system is calculated based on the base coordinate. The tiptoe position of the left leg in the base coordinate $\boldsymbol{x}_{\mathrm{tL}} = (x_{\mathrm{tL}}, z_{\mathrm{tL}})$ is calculated as

$$x_{\mathrm{tL}} = l_1 \sin(q_1) - l_2 \sin(q_2) \tag{5.35}$$

$$z_{\mathrm{tL}} = -l_1 \cos(q_1) - l_2 \cos(q_2). \tag{5.36}$$

The tiptoe position of the right leg $\boldsymbol{x}_{\mathrm{tR}}$ can be calculated using q_3 and q_4 in the same manner. The Jacobian matrix of each tiptoe in the base coordinate $\boldsymbol{J}_{\mathrm{acoL}}$ and $\boldsymbol{J}_{\mathrm{acoR}}$ can be calculated using the joint angle vector $\boldsymbol{q} = (q_1,\ q_2,\ q_3,\ q_4)$ as

$$\boldsymbol{J}_{\mathrm{acoL}} = \frac{\partial \boldsymbol{x}_{\mathrm{tL}}}{\partial \boldsymbol{q}} \tag{5.37}$$

$$\boldsymbol{J}_{\mathrm{acoR}} = \frac{\partial \boldsymbol{x}_{\mathrm{tR}}}{\partial \boldsymbol{q}}. \tag{5.38}$$

The velocity of the tiptoes in the base coordinate is calculated using the Jacobian matrices as $\dot{\boldsymbol{x}}_{\mathrm{tL}} = \boldsymbol{J}_{\mathrm{acoL}}\boldsymbol{q}$ and $\dot{\boldsymbol{x}}_{\mathrm{tR}} = \boldsymbol{J}_{\mathrm{acoR}}\boldsymbol{q}$. The position and velocity of the support-leg tiptoe and the swing-leg tiptoe are induced in response to the right or left stance as

$$[\boldsymbol{x}_{\mathrm{sp}}, \dot{\boldsymbol{x}}_{\mathrm{sp}}, \boldsymbol{x}_{\mathrm{sw}}, \dot{\boldsymbol{x}}_{\mathrm{sw}}] = \begin{cases} [\boldsymbol{x}_{\mathrm{tL}}, \dot{\boldsymbol{x}}_{\mathrm{tL}}, \boldsymbol{x}_{\mathrm{tR}}, \dot{\boldsymbol{x}}_{\mathrm{tR}}] & \text{(if right stance)} \\ [\boldsymbol{x}_{\mathrm{tR}}, \dot{\boldsymbol{x}}_{\mathrm{tR}}, \boldsymbol{x}_{\mathrm{tL}}, \dot{\boldsymbol{x}}_{\mathrm{tL}}] & \text{(if left stance).} \end{cases} \tag{5.39}$$

Support-Leg Control System

The energy response is induceed based on the horizontal body position and velocity in the support coordinate ${}^{\mathrm{sp}}x_{\mathrm{b}}, {}^{\mathrm{sp}}\dot{x}_{\mathrm{b}}$. The energy response E are calculated as

$$E = \frac{1}{2}({}^{\mathrm{sp}}\dot{x}_{\mathrm{b}}^2 - \omega_{\mathrm{c}}^2\, {}^{\mathrm{sp}}x_{\mathrm{b}}^2). \tag{5.40}$$

Trasforming the energy variables to the equivalent energy variables through $A = \sqrt{2E}$, the equivalent energy controller is implemented using energy control gain C_{e} as

$$a_{\mathrm{A}}^{\mathrm{ref}} = C_{\mathrm{e}}(A^{\mathrm{cmd}} - A). \tag{5.41}$$

The acceleration reference of the body control input in the x axis $\ddot{x}_{\mathrm{sp}}^{\mathrm{ref}}$ is calculated by

$$\ddot{x}_{\mathrm{sp}}^{\mathrm{ref}} = a_{\mathrm{A}}^{\mathrm{ref}} \cosh(\phi) + \frac{g}{Z_{\mathrm{c}}}\, {}^{\mathrm{sp}}x_{\mathrm{b}}. \tag{5.42}$$

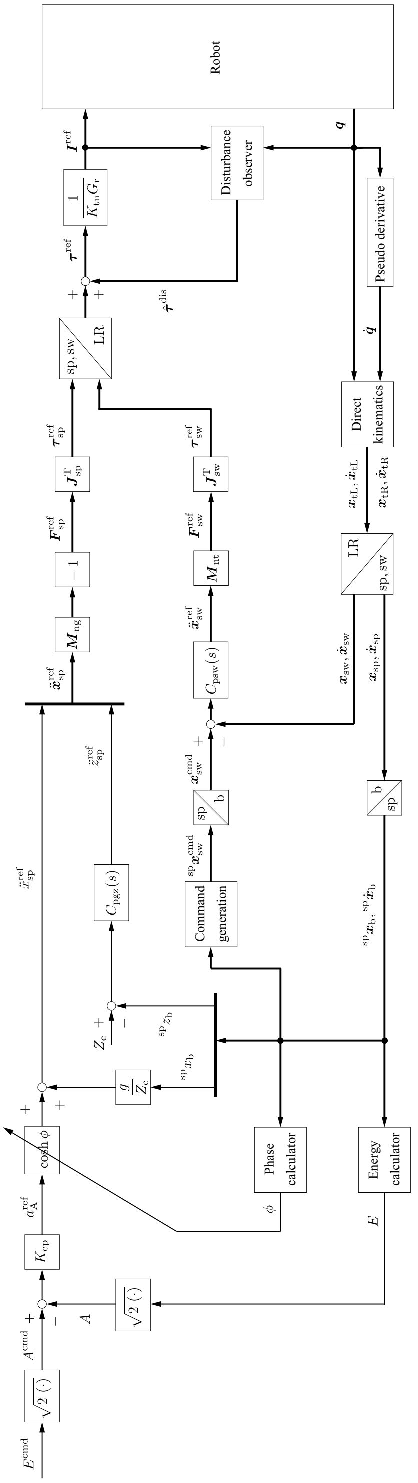

Fig. 5-15: The whole block diagram: body and swing-leg control.

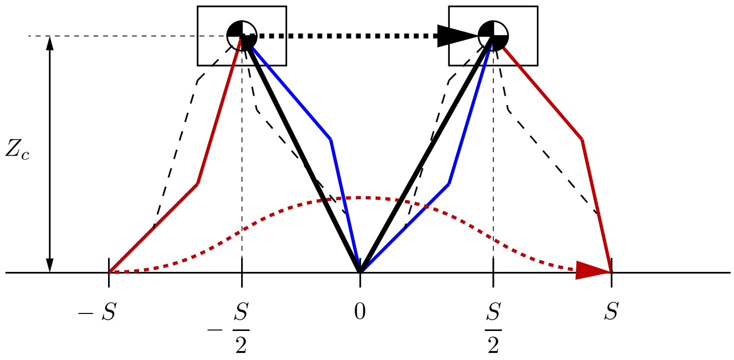

Fig. 5-16: Trajectory of the biped walking control.

The acceleration reference of the body control input in the z axis $\ddot{z}_{\mathrm{sp}}^{\mathrm{ref}}$ is determined by the position control as

$$\ddot{z}_{\mathrm{sp}}^{\mathrm{ref}} = C_{\mathrm{pz}}(s)(Z_{\mathrm{c}} - {}^{\mathrm{sp}}z_{\mathrm{b}}), \tag{5.43}$$

where the position command of the body in the z axis is Z_{c}. $C_{\mathrm{pz}}(s)$ is the controller gain. The acceleration references $\ddot{x}_{\mathrm{sp}}^{\mathrm{ref}}$ and $\ddot{z}_{\mathrm{sp}}^{\mathrm{ref}}$ are summarized as the vector $\ddot{\boldsymbol{x}}_{\mathrm{sp}}^{\mathrm{ref}}$. Because of law of action and reaction, the force reference $\boldsymbol{F}_{\mathrm{sp}}^{\mathrm{ref}}$ is expressed as

$$\boldsymbol{F}_{\mathrm{sp}}^{\mathrm{ref}} = -\boldsymbol{M}_{\mathrm{ng}}\ddot{\boldsymbol{x}}_{\mathrm{sp}}^{\mathrm{ref}}. \tag{5.44}$$

Swing-Leg Control System

The swing-leg trajectory command is determined by the body position in the support coordinate ${}^{\mathrm{sp}}x_{\mathrm{b}}$ as Fig. 5-16. By this trajectory generation, the horizontal body position becomes the main variable of the biped walking control. For simplification, the sinusoidal trajectory is employed as

$$ {}^{\mathrm{sp}}x_{\mathrm{t}}^{\mathrm{cmd}} = 2\,{}^{\mathrm{sp}}x_{\mathrm{b}} \tag{5.45}$$

$$ {}^{\mathrm{sp}}z_{\mathrm{t}}^{\mathrm{cmd}} = \frac{H_{\mathrm{t}}}{2}\left(1 + \cos\left(2\pi\frac{{}^{\mathrm{sp}}x_{\mathrm{b}}}{S}\right)\right). \tag{5.46}$$

After transforming the coordinate of the tiptoe command from the support-leg coordinate to the base coordinate, the tiptoe position control is implemented. The acceleration reference $\ddot{\boldsymbol{x}}_{\mathrm{t}}^{\mathrm{ref}}$ as the control output is calculated using position gain $\boldsymbol{C}_{\mathrm{p}}(s)$ as

$$\ddot{\boldsymbol{x}}_{\mathrm{t}}^{\mathrm{ref}} = \boldsymbol{C}_{\mathrm{p}}(s)(\boldsymbol{x}_{\mathrm{t}}^{\mathrm{cmd}} - \boldsymbol{x}_{\mathrm{t}}). \tag{5.47}$$

Because the mass in the workspace is set as constant M_{tn} by the joint-space observer, the force reference $\boldsymbol{F}_{\mathrm{t}}^{\mathrm{ref}}$ is expressed as

$$\boldsymbol{F}_{\mathrm{t}}^{\mathrm{ref}} = M_{\mathrm{tn}}\ddot{\boldsymbol{x}}_{\mathrm{t}}^{\mathrm{ref}}. \tag{5.48}$$

It is possible to attain the more accurate control by considering the derivative of Jacobian matrix as $\boldsymbol{F}_{\mathrm{t}}^{\mathrm{ref}} = M_{\mathrm{tn}}(\ddot{\boldsymbol{x}}_{\mathrm{t}}^{\mathrm{ref}} - \dot{\boldsymbol{J}}_{\mathrm{aco}}\dot{\boldsymbol{q}})$.

Force-Torque Conversion

The relation of torque and force in statics is utilized for the conversion from the force reference to the torque reference. The relation of the tiptoe force reference $(\boldsymbol{F}_{\mathrm{sp}}^{\mathrm{ref}}, \boldsymbol{F}_{\mathrm{sw}}^{\mathrm{ref}})$ and the torque reference is written as

$$\begin{bmatrix} \boldsymbol{\tau}_{\mathrm{sp}}^{\mathrm{ref}} \\ \boldsymbol{\tau}_{\mathrm{sw}}^{\mathrm{ref}} \end{bmatrix} = \begin{bmatrix} \boldsymbol{J}_{\mathrm{sp}}^{\mathrm{T}}\boldsymbol{F}_{\mathrm{sp}}^{\mathrm{ref}} \\ \boldsymbol{J}_{\mathrm{sw}}^{\mathrm{T}}\boldsymbol{F}_{\mathrm{sw}}^{\mathrm{ref}} \end{bmatrix}. \tag{5.49}$$

The torque reference of each actuator is finally induced as

$$[\boldsymbol{\tau}_{\mathrm{L}}^{\mathrm{ref}}, \boldsymbol{\tau}_{\mathrm{R}}^{\mathrm{ref}}] = \begin{cases} [\boldsymbol{\tau}_{\mathrm{sp}}^{\mathrm{ref}}, \boldsymbol{\tau}_{\mathrm{sw}}^{\mathrm{ref}}] & \text{(if right stance)} \\ [\boldsymbol{\tau}_{\mathrm{sw}}^{\mathrm{ref}}, \boldsymbol{\tau}_{\mathrm{sp}}^{\mathrm{ref}}] & \text{(if left stance)} \end{cases} \tag{5.50}$$

In the control system based on the body and the swing leg, force-torque conversion becomes simpler because the control systems of the left leg and the right leg are independent.

5.5 Feasible Walking Command Generation Based on Walking Stability

Command generation is important as well as the control system design for realizing the function. This section describes the feasible command generation based on analyses of walking stability.

5.5.1 Analysis of Walking Based on Phase Diagram

Conventionally, Zaytsev et al. [102] analyzed walking stability based on a phase diagram using a simple linear inverted pendulum. The available area is induced by subtracting the unavailable area which expresses the constraints. This section analyzes the walking stability considering the implementation constraints of the proposed control method.

The foundation of this analysis is the vector field of the linear inverted pendulum as Fig. 5-6. The following constraints 1 and 2 limit the area, and the feasible motion region is induced. Constraint 1 is the actuation limitation of the body mass. Constraint 2 is the bandwidth of the swing-leg control.

Constraint 1: Actuation Limit of the Body Mass

In the implementation, there is a limitation in the actuation force of the body mass, or the actuation acceleration of the body mass. Because of the limitation of the actuation and the energy conservation law, the area of the state variables (the position and the velocity) are limited.

Necessary Condition of Constraint 1: Energy Conservation in the Case of the Maximum Energy Injection The maximum energy at the next step $E_{n+1}^{\max}$ is realized when the maximum actuation acceleration $|\ddot{x}^{\mathrm{ref}}|_{\max}$ is input constantly. $E_{n+1}^{\max}$ is concretely induced as

$$E_{n+1}^{\max} = E_n + |\ddot{x}^{\mathrm{ref}}|_{\max} S. \tag{5.51}$$

Here, E_n is the energy at the n th step, and S is the stride of the body mass in one stance. Considering the energy at the zero positon is $E = \frac{1}{2}\dot{x}^2$, the maximum velocity at the $(n+1)$th step is expressed as

$$\dot{x}_{n+1}^{\mathrm{cmd,max}} = \sqrt{\dot{x}_n^2 + 2|\ddot{x}^{\mathrm{ref}}|_{\max} S}. \tag{5.52}$$

Conservative Condition of Constraint 1: Actuation without Saturation It is ideal that saturation of actuation does not occur. Because the required actuaion at the beginning the phase is the largest in case of no large disturbance, the maximum acceptable control erorr of energy is induced as

$$|\Delta E|_{\max} = \frac{|\ddot{x}^{\mathrm{ref}}|_{\max}}{K_p \cosh |\phi|_{\max}}, \tag{5.53}$$

where ΔE is concretely expressed as

$$\Delta E = E^{\mathrm{cmd}} - E^{res} = \frac{1}{2}(\dot{x}_{n+1}^{\mathrm{cmd}\ 2} - \dot{x}_n^2). \tag{5.54}$$

Therefore, the maximum acceptable velocity command is induced using (5.53) and (5.54) as

$$\dot{x}_{n+1}^{\mathrm{cmd,max}} = \sqrt{\dot{x}_n^2 + 2|\Delta E|_{\max}}. \tag{5.55}$$

Constraint 2: Bandwidth of the Swing-Leg Control

The swing-leg position control has a limitation of bandwidth. The limitain of the control bandwidth determines the maximum feasible velocity. For simplicity, it is assumed that velocity of the body mass is constant. From the relation of $\frac{2\pi}{S/V_{\mathrm{x}}} = \omega$, the maximum feasible velocity becomes

$$\dot{x}_{\max}^{\mathrm{cmd}} = \frac{\omega_{\mathrm{ctl}}^{\max} S}{2\pi}. \tag{5.56}$$

Here, the bandwidth of swing-leg control $\omega_{\mathrm{ctl}}^{\max}$ is identified through experiments or analysis.

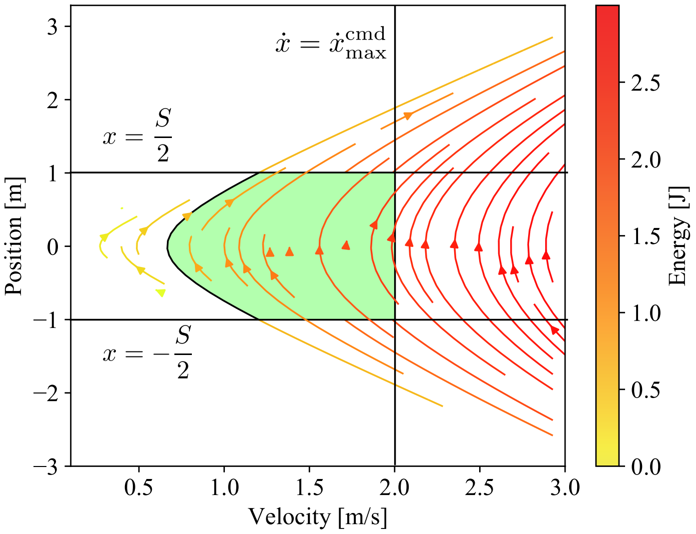

Fig. 5-17: Controllable region in phase diagram.

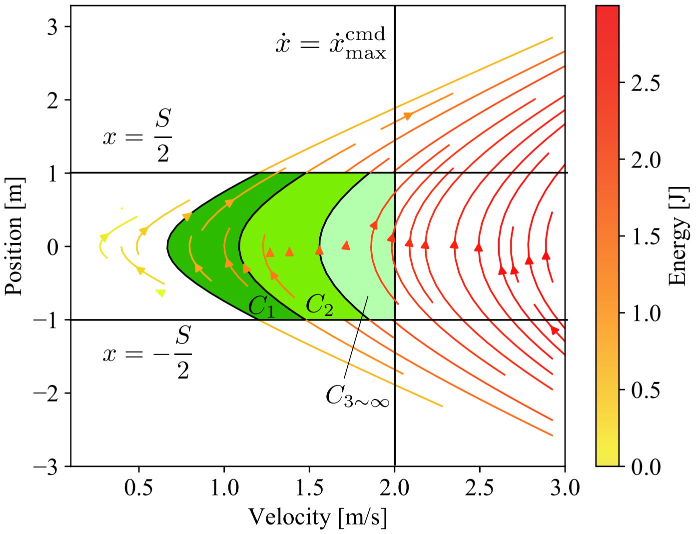

Fig. 5-18: Stepped controllable region in phase diagram.

Controllable Region

From the foundational vector field and the constraints 1 and 2, the controllable region is induced as Fig. 5-17. The green are in Fig. 5-17 shows the controllable region. The boundaries are induced from

Table 5.2: Parameters of the simulations for the biped walking control.

Description	Parameter	Value
Total mass	m	26.6 kg
Weight of the body	m_{b}	15.0 kg
Weight of the one leg	m_l	5.8 kg
Sampling time of control	T_s	0.100 ms
Length of thigh and shin	l	0.45 m
Nominal torque constant	K_{tn}	0.091 Nm/A
Gear ratio of the motors	G	1:126
Walking stride	S	0.30 m
Maximum height of swing leg	H_{t}	0.10 m
COG height	Z_{c}	0.60 m
Angular frequency of phase control	ω	$\sqrt{g/Z_{\mathrm{c}}}$
P gain of energy control	K_{ep}	100
P gain of position control	K_{p}	10000
D gain of position control	K_{d}	200
Cut-off frequency of joint space observer	g_{dis}	50.0 rad/s
Cut-off frequency of pseudo derivative	g_{pd}	120.0 rad/s
Environment stiffness	K_{env}	30000 N/m
Environment viscosity	D_{env}	2000 Ns/m

(5.51) or (5.53). The controllable region can be categorized in terms of the necessary step number as Fig. 5-18. C_i shows the controllable region in i steps. By referring to Fig. 5-18, the necessary step number and the command design can be shown.

5.6 Biped Simulations

Simulation of biped walking is conducted based on the proposed energy/phase control. The initial condition is the same as the one explained in Fig. 5-13 of Section 5.3: the body is at $(0,\ Z_{\mathrm{c}})$, the left tiptoe is at $(\frac{S}{2},\ 0)$, and the right tiptoe is at $(\frac{S}{2},\ 0)$. The respective velocity is zero. Constant speed walking and variable speed walking are simulated. In the respective walking simulations, the conventional velocity control and the proposed energy/phase control are compared. The desired velocity

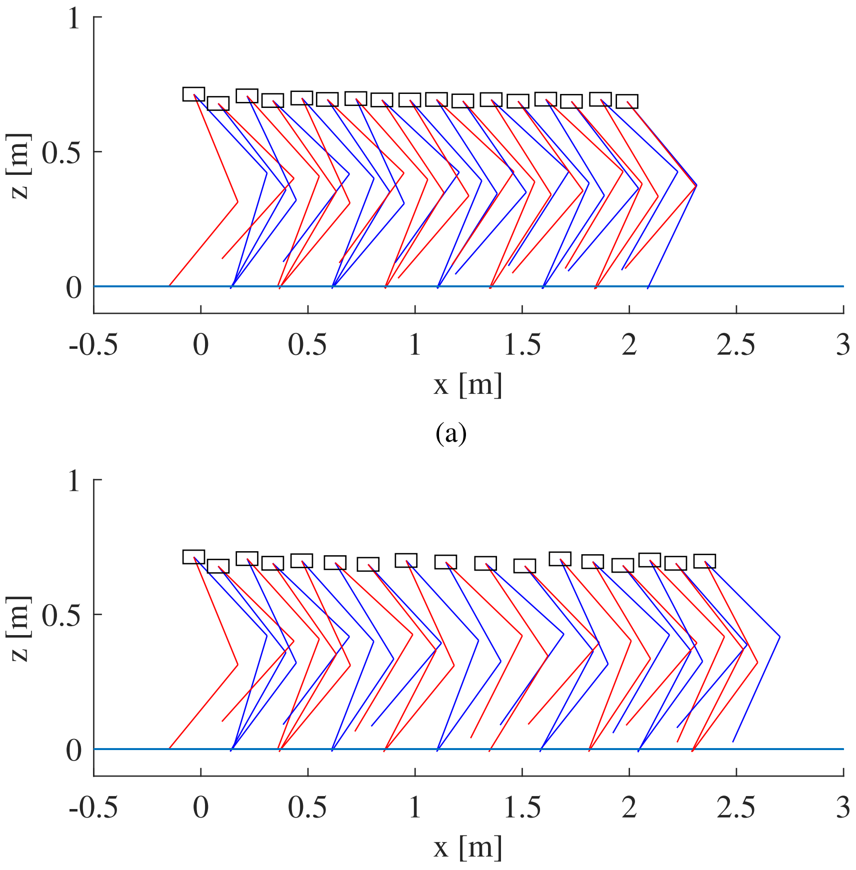

(a)

(b)

Fig. 5-19: Stick picture of the simulation results: (a) constant-speed walking, (b) variable-speed walking.

of the conventional method is set as $V_{\mathrm{x}}^{\mathrm{cmd}}$ 0.222 m/s (= 0.8 km/h). The desired velocity at the stance change of the proposed method is set as $V_{\mathrm{x}} = 0.611$ m/s. These desired velocities are induced so that the respective periods become equal. The walking periods of the conventional method τ_{c} and the proposed method τ_{p} are calculated

$$\tau_{\mathrm{c}} = S/V_{\mathrm{x}}^{\mathrm{cmd}} \tag{5.57}$$

$$\tau_{\mathrm{p}} = T_{\mathrm{c}}\mathrm{ln}\frac{S/2 + T_{\mathrm{c}}V_{\mathrm{x}}}{-S/2 + T_{\mathrm{c}}V_{\mathrm{x}}}. \tag{5.58}$$

Fig. 5-19 is the stick pictures of the simulation results. Fig. 5-19 (a) shows the results with the constant command. The walking is attained, and the body moves with a constant width. It is revealed that the constant walking is attained. Fig. 5-19 (b) shows the resluts with the variable command. The walking is attained, and the body moves with different widths. It is shown that the variable walking is

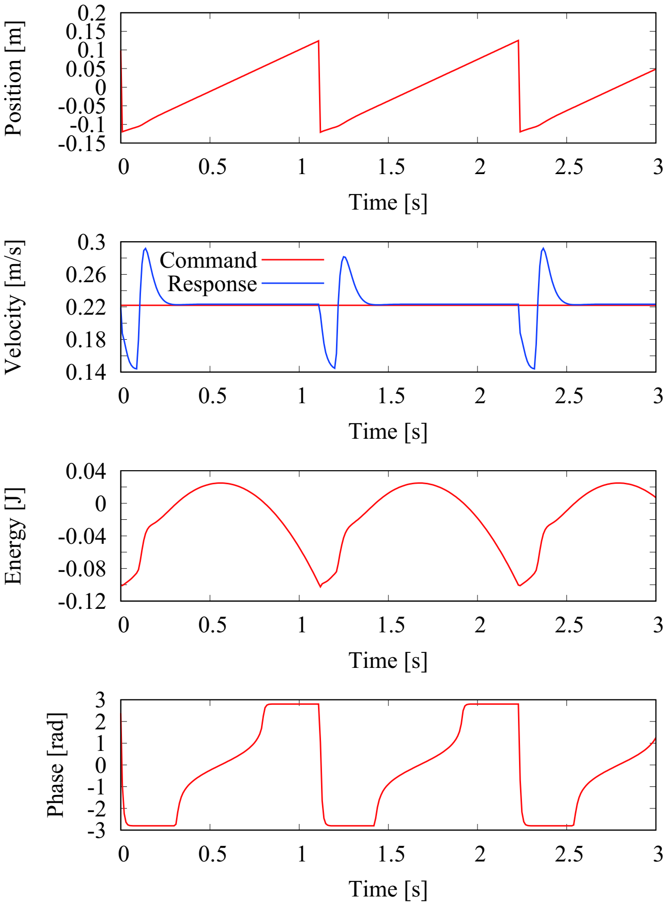

Fig. 5-20: Simulation results of the conventional velocity control with constant command.

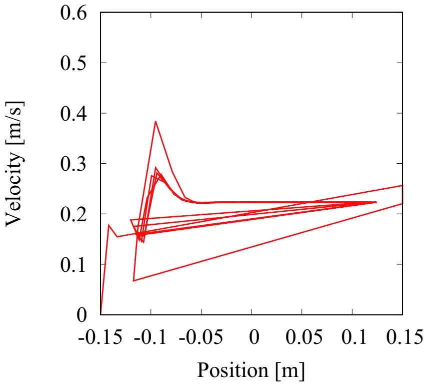

Fig. 5-21: Phase diagram of the conventional velocity control with constant command.

attained.

The times-series results of the constant walking simulations are shown in Figs. 5-20 and 5-22. Fig.

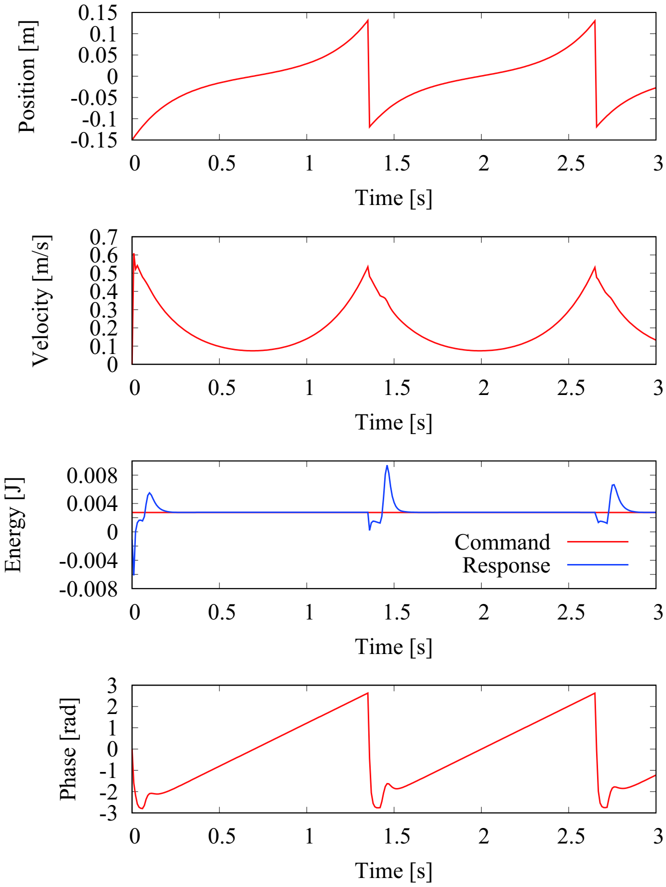

Fig. 5-22: Simulation results of the proposed energy/phase control with constant command.

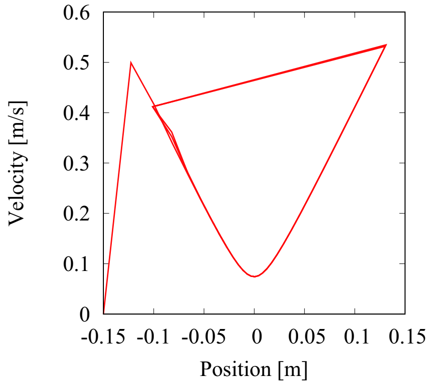

Fig. 5-23: Phase diagram of the proposed energy/phase with constant command.

5-20 is the results of the conventional velocity control. The velocity response is constant as the desired velocity. Because the velocity is constant, the orbital energy is not constant. Fig. 5-22 shows the results

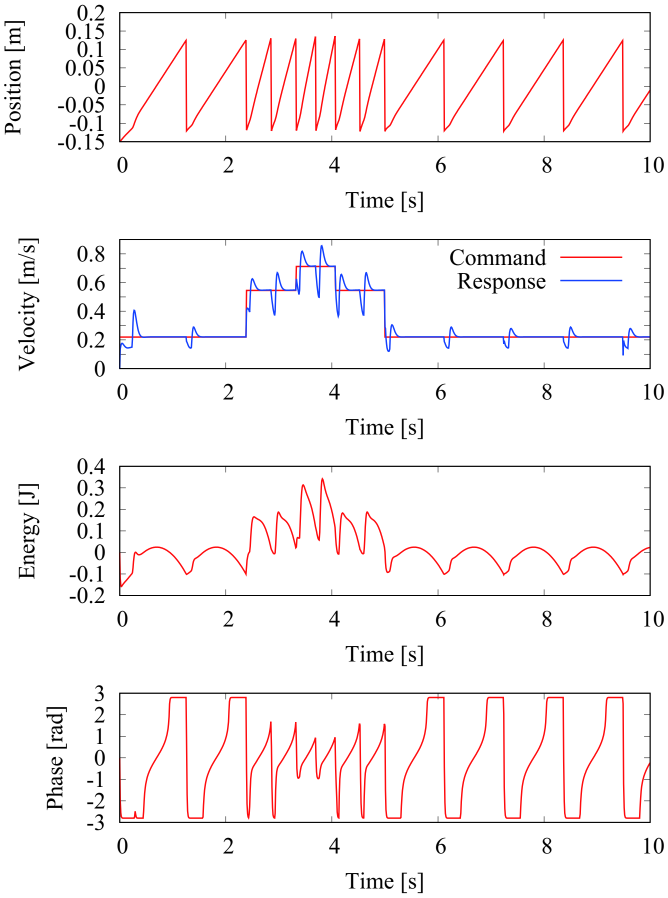

Fig. 5-24: Simulation results of the conventional velocity control with variable command.

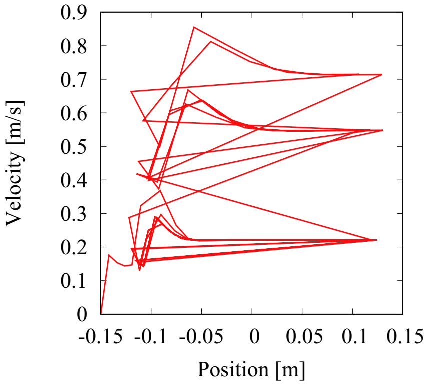

Fig. 5-25: Phase diagram of the conventional velocity control with variable command.

of the proposed energy/phase control. The curves of the position and the velocity are hyperbolic. The energy response is constant as the energy command. The phase changes with constant velocity. The

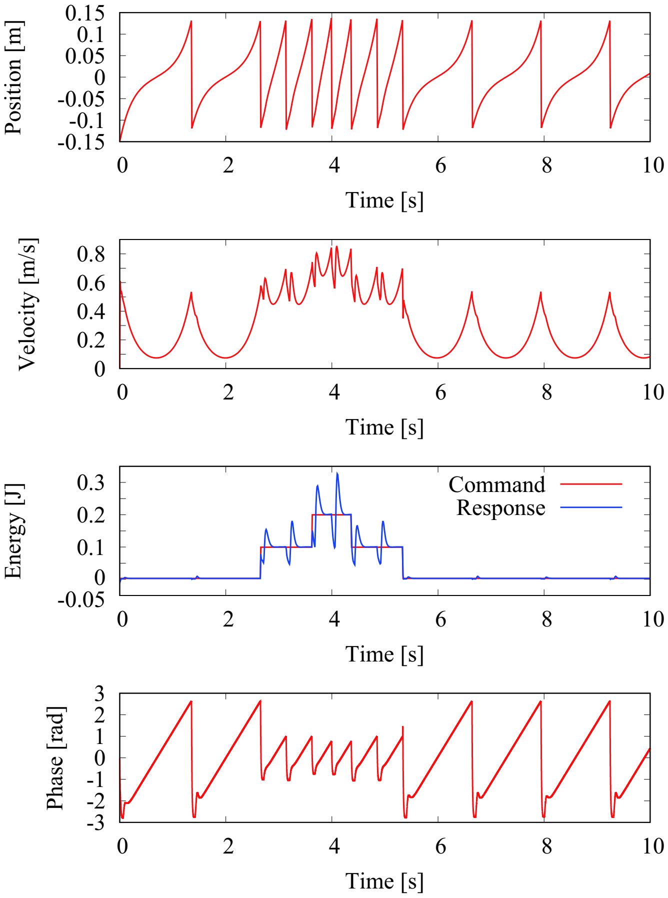

Fig. 5-26: Simulation results of the proposed energy/phase control with variable command.

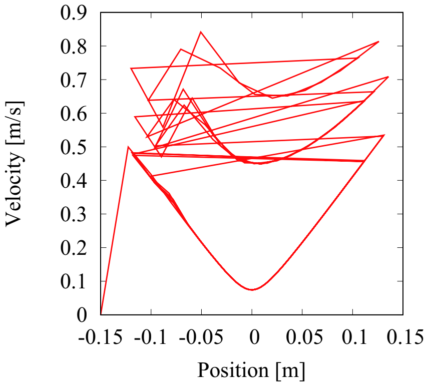

Fig. 5-27: Phase diagram of the proposed energy/phase with variable command.

energy consumption of the conventional method and the proposed method are 119.85 mWh and 77.44 mWh. The energy consumption of the proposed method is lower than the conventional method. The current consumption of the conventional method and the proposed method are 33.10 mAh and 19.80 mAh, respectively. The current consumption of the proposed method is also lower.

The times-series results of the variable walking simulations are shown in Figs. 5-24 and 5-26. Fig. 5-24 shows the simulation results of the conventional velocity control. The velocity command varies in step wise. The velocity response converges to the command after each touchdown. Because the velocity converges to the constant value, the orbital energy is not constant. Fig. 5-26 shows the results of the proposed energy/phase control. The energy command is set as the step wise. The energy response converges to the energy command in each step. The higher the energy command is, the shorter the period is. This is reasonable because the stride is constant and the velocity is higher. The widths of the phase change are also different while the phase changes with constant velocity. The energy consumption of the conventional method and the proposed method are 367.39 mWh and 398.00 mWh. The energy consumption of the proposed method is a little higher than the conventional method. The current consumption of the conventional method and the proposed method are 71.73 mAh and 71.4 mAh, respectively. The current consumption of the proposed method is a little lower.

Compared to the ideal simulations, the superiority of the proposed method in the biped simulations becomes weakened in terms of the energy efficiency. The control in the biped simulations requires the additional energy and current for nominalizing the dynamics. Even though, the simulation results of the constant biped walking show the superiority of the proposed method clearly.

5.7 Additional Analyses

To confirm the applicability of the proposed method, additional simulations are conducted. The damping friction and the different mass distribution are focused. Impact force from the ground is already considered in the biped simulations. The ground is modeled as a spring-damper system.

Also, the relation between model mismatch and the energy consumption change is analyzed.

5.7.1 Damping Friction

The biped walking considering the gear damping is conducted. The damping coefficient of the gears is 4.3 Nm/(rad/s). The biped walking with the same damping coefficient, the twice and the three-times damping coefficients are simulated.

Fig. 5-28 shows the simulation results of the biped walking with geared damper. In the respective

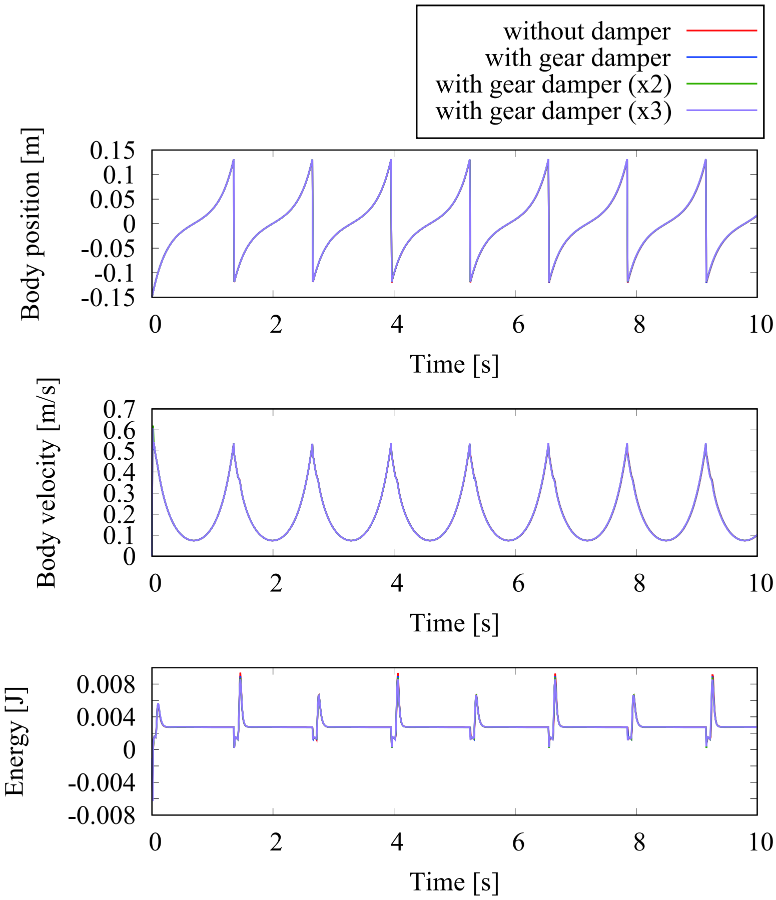

Fig. 5-28: Results of the biped simulaitons with damper.

cases, the damping disturbances are compensated, and the desired energy is realized after the impact. The position and the velocity responses are also consistent regardless of the damping. The biped walking control system includes a disturbance observer in the inner loop, which suppresses the damping disturbance.

5.7.2 Mass Distribution

Three patterns of the mass distribution are considered. Case 1 is the parameters used in Section 5.6. Case 2 assumes that the leg bars are lighter-weight, and case 3 assumes that the leg bars are heavier. The concrete parameters are shown in Table 5.3. Mass of the leg bar is set as 1.0 kg in case 2, and 2.0 kg in case 3. The constant biped walking is simulated for the comparison.

The simulation results are shown in Fig. 5-29. The body position, the velocity, and the energy are

Table 5.3: Parameters of the simulations with different mass.

Item	Case1	Case2	Case3
Body mass m_b	15.0 kg	15.0 kg	15.0 kg
Mass of bar 1 m_1	1.5 kg	1.0 kg	2.0 kg
Mass of bar 2 m_2	1.4 kg	1.0 kg	2.0 kg
Mass of bar 3 m_3	1.5 kg	1.0 kg	2.0 kg
Mass of bar 4 m_4	1.4 kg	1.0 kg	2.0 kg

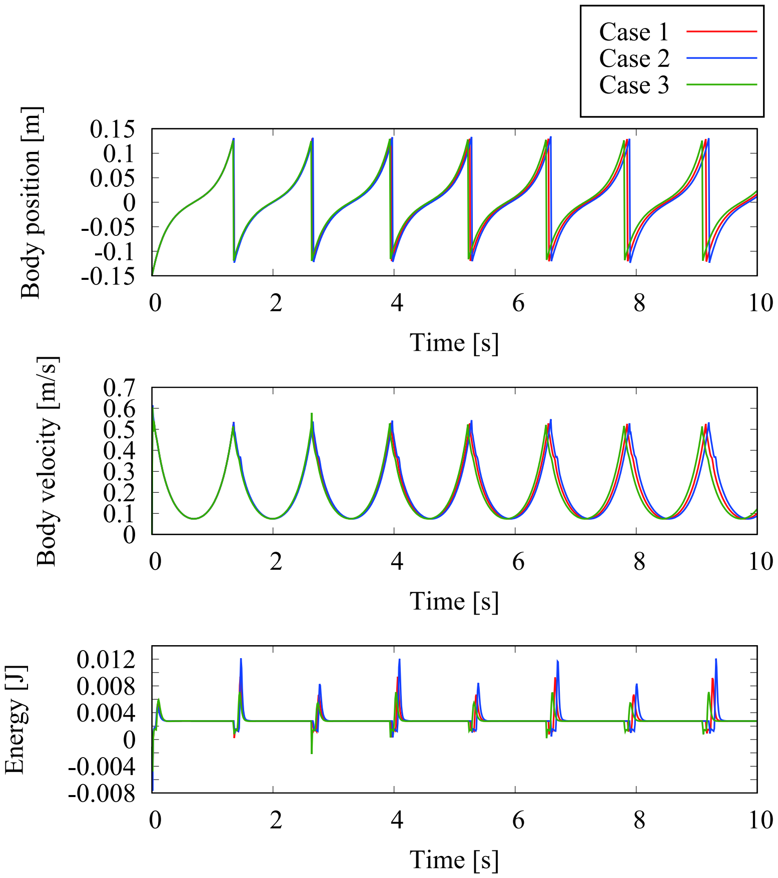

Fig. 5-29: Results of the biped simulaitons with different mass distribution.

plotted. The respective position and velocity response shows the similar periodic shape, and attains periodic walking. The small shifts are observed in the position and the velocity response. The shifts are owing to that the contact detection is implemented by a certain common threshold of the reaction force and that the reaction force changes in response to the weight of the robot. The heavier case (case 3) has the earlier changes of the states, and the lighter case (case 2) has the latter changes of the states.

5.7.3 Model Mismatch and Energy Consumption Change

The relation of the model mismatch and the energy consumption change is analyzed. The motion equation of the biped robot in the support coordinate can be expressed as

$$\boldsymbol{M}^{\mathrm{sp}}(\boldsymbol{q})\ddot{\boldsymbol{q}} + \boldsymbol{g}^{\mathrm{sp}}(\boldsymbol{q},\dot{\boldsymbol{q}}) = \boldsymbol{\tau}^{\mathrm{ref}} + \boldsymbol{\tau}^{\mathrm{ext}}, \tag{5.59}$$

where $\boldsymbol{M}^{\mathrm{sp}}$ and $\boldsymbol{g}^{\mathrm{sp}}$ are the mass matrix and the other terms in the support coordinate. $\boldsymbol{\tau}^{\mathrm{ref}}$ and $\boldsymbol{\tau}^{\mathrm{ext}}$ are the reference torque and the external torque by the environment.

The nominalized dynamics of the biped robot in the support coordinate can be expressed as

$$\boldsymbol{M}^{\mathrm{sp}}_{\mathrm{n}}(\boldsymbol{q})\ddot{\boldsymbol{q}} + \boldsymbol{g}^{\mathrm{sp}}_{\mathrm{n}}(\boldsymbol{q},\dot{\boldsymbol{q}}) = \boldsymbol{\tau}^{\mathrm{ref}} - \boldsymbol{\tau}^{\mathrm{cmp}} + \boldsymbol{\tau}^{\mathrm{ext}}_{\mathrm{n}}. \tag{5.60}$$

The subscript n means nominal. $\boldsymbol{\tau}^{\mathrm{cmp}}$ is the additional torque for the compensation. Assuming the external torque is equivalent whether the nominalization is implemented or not, the additional compensation torque is induced using (5.59) and (5.60) as

$$\boldsymbol{\tau}^{\mathrm{cmp}} = (\boldsymbol{M}^{\mathrm{sp}}(\boldsymbol{q}) - \boldsymbol{M}^{\mathrm{sp}}_{\mathrm{n}}(\boldsymbol{q}))\ddot{\boldsymbol{q}} + \boldsymbol{g}^{\mathrm{sp}}(\boldsymbol{q},\dot{\boldsymbol{q}}) - \boldsymbol{g}^{\mathrm{sp}}_{\mathrm{n}}(\boldsymbol{q},\dot{\boldsymbol{q}}). \tag{5.61}$$

(5.61) implies that the additonal compensation torque is equal to the torque of the dynamics error between the real and the nominal. When $\boldsymbol{P}$ and $\boldsymbol{P}_{\mathrm{n}}$ are defined as the torque by the real dynamics and the nominal dyanamics as

$$\boldsymbol{P} = \boldsymbol{M}^{\mathrm{sp}}(\boldsymbol{q})\ddot{\boldsymbol{q}} + \boldsymbol{g}^{\mathrm{sp}}(\boldsymbol{q},\dot{\boldsymbol{q}}) \tag{5.62}$$

$$\boldsymbol{P}_{\mathrm{n}} = \boldsymbol{M}^{\mathrm{sp}}_{\mathrm{n}}(\boldsymbol{q})\ddot{\boldsymbol{q}} + \boldsymbol{g}^{\mathrm{sp}}_{\mathrm{n}}(\boldsymbol{q},\dot{\boldsymbol{q}}), \tag{5.63}$$

the compensation torque becomes

$$\boldsymbol{\tau}^{\mathrm{cmp}} = \boldsymbol{P} - \boldsymbol{P}_{n} := \Delta\boldsymbol{P}. \tag{5.64}$$

Here, $\Delta\boldsymbol{P}$ is the torque of the dynamics error between the real and the nominal. Because the energy is the integral of the product of the torque and the velocity, the energy consumption change is induced as

$$\Delta E = \int \boldsymbol{\tau}^{\mathrm{cmp}} \cdot \dot{\boldsymbol{x}} dt \tag{5.65}$$

$$= \int \Delta\boldsymbol{P} \cdot \dot{\boldsymbol{x}} dt. \tag{5.66}$$

Table 5.4: The theoretical prediction and the simulation results of the energy consumption change.

Item	Theoretical prediction	Simulation results
Adding the gear damper	-5.80 J	-3.54 J
Adding the gear damper (x2)	15.13 J	17.71 J
Adding the gear damper (x3)	40.52 J	46.66 J
Change of mass distribution from case 1 to case 2	98.41 J	95.94 J
Change of mass distribution from case 1 to case 3	-79.80 J	-80.08 J

In short, the energy consumption change is calculated as the integral of the product of the dynamics error torque and the velocity.

Based on the theory, the energy consumption change by adding the gear damper and changing the mass distribution is analyzed. Energy consumptions of the previous constant speed walking simulations and each case are compared. The results of the energy consumption change are summarized in Table 5.4. It is found that the theoretical prediction and the simulation results show the close values in the respective cases.

5.8 Experiments

5.8.1 Experimental Setup

To verify the proposed walking control, experiments are conducted. Fig. 5-30 shows the photos of the biped robot for the experiments. The robot body is constrained so that the body can realize horizontal and vertical motion. The parallel-link legs are realized by setting the geared motors facing each other as the one-leg hopping robot in Section 4. The encoders are also set on the motor sides. While contact detection is necessary for the state change, the contact detection is implemented based on the reaction force by the disturbance observer.

Two control methods are compared using the biped robot: the conventional velocity control and the proposed energy/phase control. Each response and energy consumption are compared.

5.8.2 Experimental Results

Fig. 5-31 shows the experimental results of the conventional velocity control. The velocity control controls the velocity as constant. Although there are some errors at 0.5 s and at the change point of the support leg, the velocity response converges to the desired value. Because the velocity is constant, the

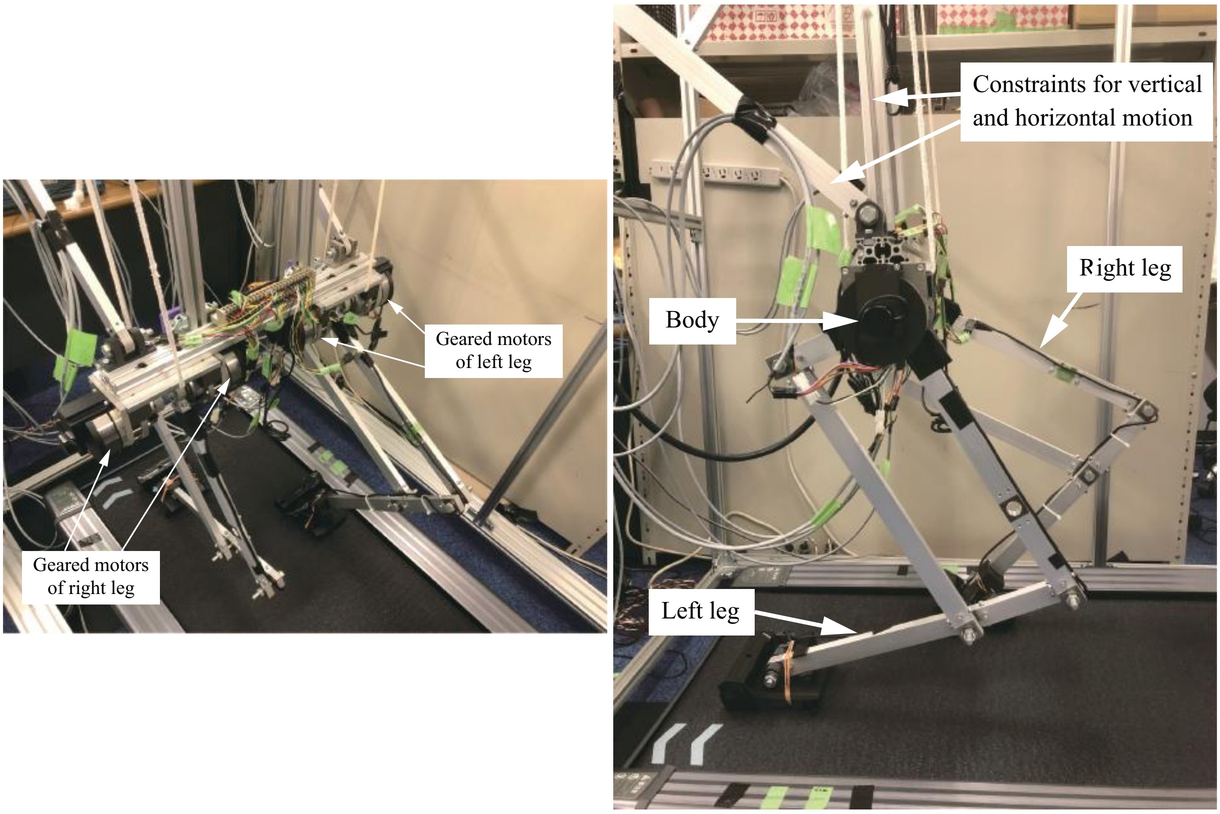

Fig. 5-30: Setup of the biped experiments.

Table 5.5: Parameters of the experiments for the biped walking control.

Description	Parameter	Value
Total mass	M	17.1 kg
Sampling time of control	T_{s}	0.100 ms
Height of body	Z_{c}	0.6 m
Stride of body	S	0.3 m
Length of thigh and shin	l	0.45 m
Nominal torque constant	K_{tn}	0.231 Nm/A
Gear ratio of the motors	G	50
P gain of energy control	K_{ep}	5

orbital energy is not constant.

Fig. 5-33 shows the experimental results of the proposed energy/phase control. The energy/phase control controls the orbital energy, not the velocity. While the velocity is not constant, the energy is controlled as constant. Although there are errors at the change of the support leg, the errors stabilize by the proposed control. The phase proceeds at the respective support period. The upper bound and the

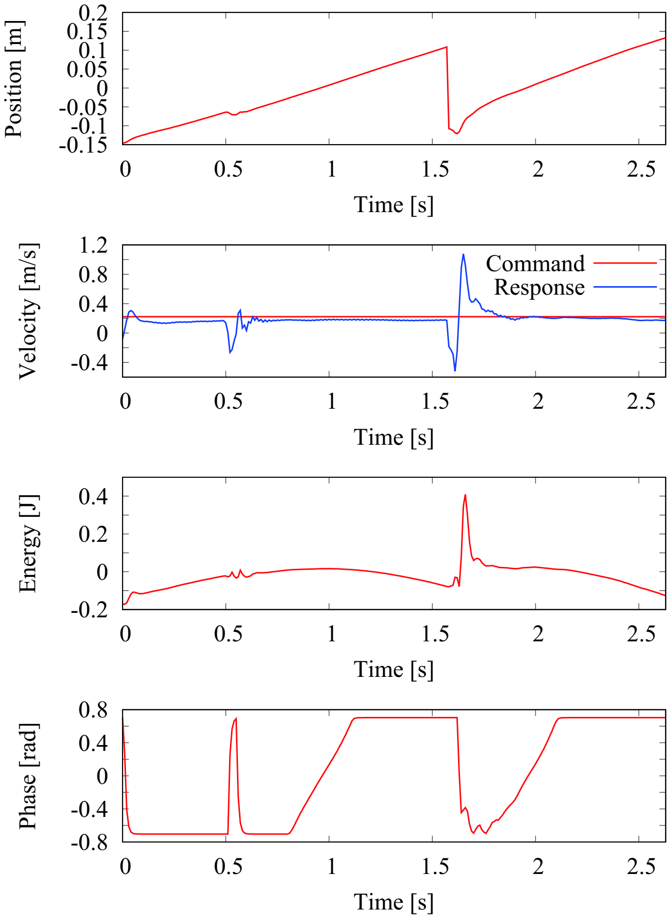

Fig. 5-31: Experimental results of the conventional velocity control.

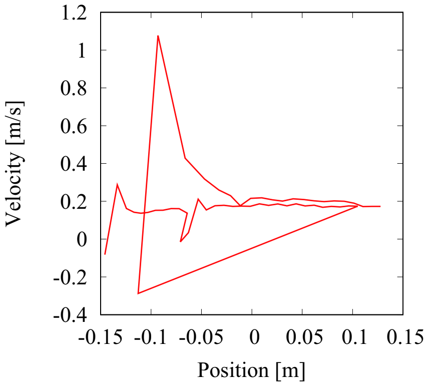

Fig. 5-32: Phase diagram of the conventional velocity control in the experimental results.

lower bound of the phase are set for the prevention of destabilization.

Figs. 5-32 and 5-34 show the phase diagram of the velocity control and the energy/phase control.

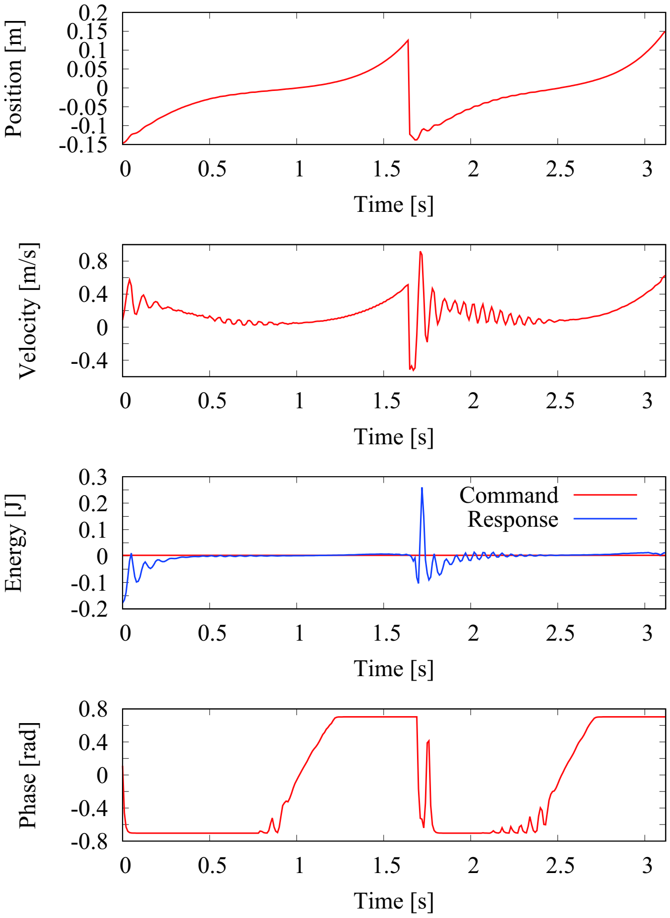

Fig. 5-33: Experimental results of the proposed energy/phase control.

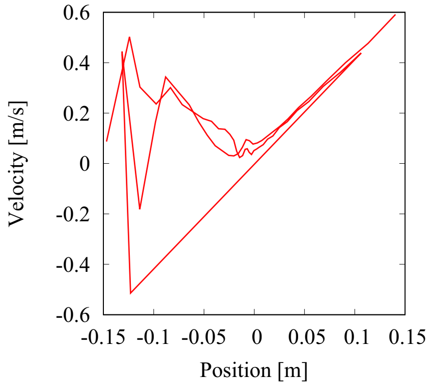

Fig. 5-34: Phase diagram of the proposed energy/phase in the experimental results.

In Fig. 5-32, the horizontal line is observed. This is reasonable because the velocity control keeps the velocity constant. In Fig. 5-34, the hyperbolic curve is observed. This is reasonable because the

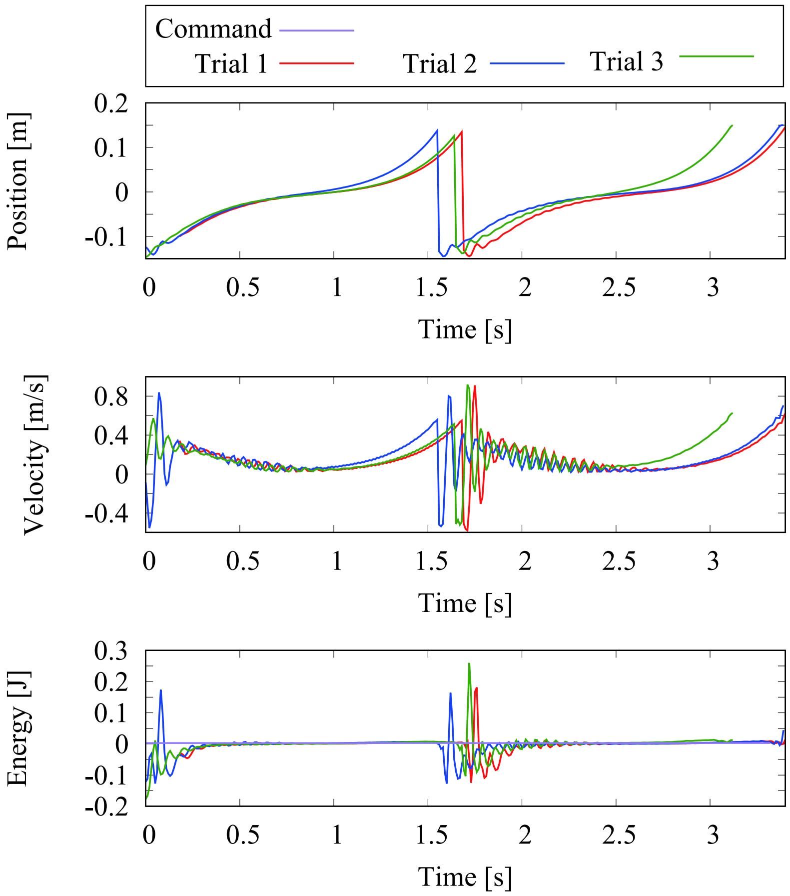

Fig. 5-35: Several results of the biped walking experiments using the energy/phase control.

energy/phase control keeps the energy constant, and the trajectory becomes a hyperbolic function.

The energy consumptions of the conventional velocity control and the proposed energy/phase control are 12.25 mWh and 9.83 mWh, respectively. The current consumptions of the velocity control and the energy/phase control are 1.74 mAh and 1.70 mAh, repsectively. The both energy and current consumptions of the proposed method are superior in this trial.

The several trials of the biped walking experimental results are compared. Fig. 5-35 and Table 5.6 show the several results of the biped walking experiments using the energy/phase control. The averages of the energy consumption of the conventional method and the proposed method are 12.19 mWh and 10.98 mWh, respectively. Although the energy consumption results of the proposed method are lower, the values are close. Because the step change is determined by the sensorless contact force estimation in the experiments, the step length is not equal. As an index of the energy consumption considering the

Table 5.6: Results of the energy consumption, the step distance, and CoT in the biped walking experiments.

Item	Energy consumption	two-step distance	CoT
Conventional method, trial 1	12.27 mWh	0.49 m	0.53
Conventional method, trial 2	10.64 mWh	0.50 m	0.46
Conventional method, trial 3	13.65 mWh	0.47 m	0.63
Proposed method, trial 1	12.08 mWh	0.53 m	0.49
Proposed method, trial 2	11.17 mWh	0.55 m	0.44
Proposed method, trial 3	9.83 mWh	0.55 m	0.39

step distance, cost of transport (CoT) is popular in legged robots. CoT is calculated by E/mgd, where E, m, g, and d are the energy consumption, the mass, the gravitational acceleration, and the distance. CoT is proportional to the ratio the energy consumption to the walking distance. The CoT average of the conventional method and the proposed method are 0.54 and 0.44, respectively. Low CoT implies a low energy cost for transport. However, the performance difference in the experimental results is not as remarkable as the simulation results. It is assumed that the dynamics error between the experimental setup and the nominal system is larger than the simulations. Another demerit of the proposed method is that the control system sometimes diverges to the negative direction under the environment where the energy control gain cannot be high enough. The reason is that the energy immediately after switching the stance leg is negative, and that the negative energy leads to divergence to the negative direction.

5.9 Summary

This chapter dealt with the biped walking control utilizing the dynamics of the linear inverted pendulum. The energy/phase control was proposed as an oscillation method of an inverted pendulum. The phase control simplifies the dynamics by synchronizing the oscillation phase to the phase of the linear inverted pendulum. The dynamics under the phase control is simplified using the energy-equivalent variables, and the dynamics become an integral element. Energy control is constructed based on the energy dynamics. The appropriateness of the proposed method was confirmed by the simulations using a linear inverted pendulum.

It was also confirmed that the proposed method works properly for a biped walking robot. In the biped control, the simultaneous control of the body and the swing leg was employed. The feasible command generation was induced from the walking stability and the energy conservation law. The simulations and the experiments of a biped robot were conducted.

In the additional analyses, the simulations with the gear damping and the simulations with different mass distributions were conducted. The relationship between the model mismatch and the energy consumption were also inducted, and compared with the simulation results.

Chapter 6

Conclusions

This dissertation proposed energy/phase control for realizing both the energy-efficient oscillation and the energy control. By utilizing the dynamics of the oscillator of the plant, efficient oscillation is realized. The energy/phase control was induced in the following three steps. Firstly, the energy and the phase of the oscillator were defined, and the dynamics using the energy and the phase were induced. Second, the phase control was implemented in the inner loop for energy-efficient oscillation. The phase control determines the actuation phase by synchronizing with the vibration phase. Third, the energy control was constructed in the outer loop for the control of energy. The energy control determines the actuation amplitude by feedback control of energy. The control input of the energy/phase control was determined as the product of the actuation amplitude by the energy control and the actuation phase by the phase control. Because the control input of the energy/phase control is determined by the product, the necessary number of the control input is one. The one control input realizes both the energy-efficient oscillation and the energy control.

In Chapter 2, the energy/phase control under the dynamics of a harmonic oscillator was proposed. It was shown that the energy/phase control enables both the energy-efficient oscillation and the energy control with the one input. The behavior of the energy/phase control under the dynamics of a harmonic oscillator was induced theoretically. For the verification, the simulations of the energy/phase control with the dynamics of a harmonic oscillator were conducted. The two cases were tested: the constant energy command and the stepwise energy command. In both cases, it was confirmed that the energy/phase control attains the energy control and the oscillation adequately. The theoretical analyses were conducted from the three viewpoints: stability, energy efficiency, and robustness. Compared to the conventional energy control, the proposed energy/phase control has the advantage in terms of the energy efficiency. The proposed energy/phase control oscillates only the resonant frequency component while the conventional energy control oscillates all frequency components. In return, the conventional energy control has the merit as for the robustness. The comparative simulations were also conducted for verification. As the analytical results, the simulation results also showed that the advantages of the proposed energy/phase control and the conventional energy control are the energy efficiency and the robustness, respectively. It was also confirmed that adding a disturbance observer enables to increase the robustness of the proposed energy/phase control.

Chapter 3 described the nominalization methods to the desired simple dynamics for applying the energy/phase control to a legged robot. The approach is an integrated design of mechanics and control. As for mechanics, the parallel link mechanism with the linear spring was employed to realize similar dynamics to a harmonic oscillator. Because the parallel link mechanism concentrates the weight mainly on the body, the dynamics become similar to the body mass. The linear spring generates the elastic force as the desired harmonic oscillator. The merit of the proposed mechanism was confirmed analytically compared to a serial link mechanism and a rotary spring. As for control, the nominalization control using acceleration control based on disturbance observers was discussed. The four disturbance observers are considered and compared: joint-space observer with constant inertia (JOBc), joint-space observer with variable inertia (JOBv), joint-space observer with constant mass in the workspace (JOBp), and workspace observer (WOB). The comparative simulations were conducted under the legged robot and the energy/phase control in the outer loop. It was confirmed that JOBv has superiority in terms of the control error and the energy consumption, and that WOB has superiority as for the robustness in return for the energy consumption. JOBp showed the intermediate performance between JOBv and WOB.

Chapter 4 dealt with hopping height control utilizing the energy/phase control and the nominalization method in Chapters 2 and 3. The energy/phase control under the nominalization control was implemented at the stance phase. The control at the aerial phase is the position control to keep the leg posture. The simulations under the ideal spring-mass hopping robot were conducted to verify the hopping strategy. The constant height hopping was achieved by the constant energy command as the desired height. The variable height hopping was attained by the variable energy command as desired. The experiments with the one-leg robot were conducted. The constant-height hopping and the variable-height hopping were realized as desired.

In Chapter 5, the energy/phase control is applied to a biped walking robot. The energy/phase control of a harmonic oscillator was extended to the energy/phase control of a linear inverted pendulum. The energy and the phase of a linear inverted pendulum were newly defined, and the energy/phase control for a linear inverted pendulum was constructed. The duality of the energy/phase control for a harmonic oscillator and a linear inverted pendulum was also summarized. The simulations under the ideal linear inverted pendulum were conducted to verify the energy/phase control for a linear inverted pendulum. The constant-speed and the variable-speed walking were achieved. A biped walking control system was constructed to apply to biped walking. The horizontal body motion was controlled by the energy/phase control. The vertical body motion was the position control to keep the body height. The swing leg motion was designed based on hybrid zero dynamics to realize stable walking. Feasible command generation about the energy command was also discussed. The feasible energy command was generated based on the two constraints: the actuation limit of the body mass and the bandwidth of the swing-leg control. The simulations with the biped robot were conducted. The constant-speed and the variable-speed walking were achieved as the simulations with the ideal linear inverted pendulum. Compared to the conventional constant velocity control, the proposed energy/phase control realized lower energy and current consumption in the constant-speed walking. The biped control was implemented in the experimental biped robot. The constant-speed walking experiments were conducted. The energy/phase control attained lower energy and current consumption compared to the conventional method.

This dissertation firstly solved both realization of the energy-efficient oscillation and the energy control under a known harmonic oscillator without disturbance. While the advantage of the proposed method is low energy consumption, the proposed method is weak against parameter variation. To the problem of the weakness against parameter variation, it is possible to increase the robustness by introducing a disturbance observer. There is a trade-off between the energy consumption and the robustness. The energy consumption change under a disturbance observer is analyzed, and it is mainly calculated by integrating the power of the product of the modeling error oriented torque (force) and velocity. The magnitude of the compensation torque by a disturbance observer can be tuned by the cut-off frequency of a disturbance observer. While low compensation torque by the low cut-off frequency can mitigate the large increase of energy consumption, the bandwidth of the nominalized dynamics is limited.

The proposed energy/phase control is extended for a linear inverted pendulum as well as a harmonic oscillator in order to apply the proposed method to a biped walking control. Duality of the energy/phase control for a linear inverted pendulum and a harmonic oscillator is summarized in the form of a table. The main difference between a linear inverted pendulum and a harmonic oscillator is that a linear inverted pendulum can have the negative energy, which means that the biped walking cannot go to the next step. It is necessary to increase the energy P gain in order to realize the positive energy as soon as possible.

In addition, this dissertation dealt with the problems with damping and impact as popular disturbances in legged robots. It was shown that damping can be suppressed by a disturbance observer or an energy PI controller. While it is impossible to suppress the high-frequency impact by a disturbance observer, the energy response can converge to the command value after impacts even with only a P controller. The convergence speed is determined by the P gain, and the P gain is the time constant of the energy control. The P gain can be tuned considering the relation of the desired convergence speed and the time constant.

There exist remaining issues to be solved as future works. Future works are described referring the framework of this dissertation in Fig. 1-3.

The goal of the upper layer is the generation of the energy command. Although it is simple for hopping and walking to induce the energy command, it is difficult for some motions to calculate the energy command. It is difficult for such motions to apply the proposed energy/phase control. Integration of the energy/phase control and other control is also a remaining issue. Also, not considering the angular momentum is one of the limitations of the proposed method. Like Takenaka's work [115], some biped control methods decompose the controls of upper-body translation and rotation, respectively. If such a decomposed control is employed, it is possible that the proposed method is applied in the translation direction and another control is applied in the rotation direction.

The goal of the intermediate layer is the control of the energy with efficiency under an oscillator. Although it was shown that the proposed method can deal with the damping and the short-term impact force, it is difficult to deal with the case of adding high-frequency disturbance continuously and the case that large unknown disturbance is added by such as soft ground. Another issue is that the proposed method for a linear inverted pendulum has negative energy just after switching the stance leg, which sometimes makes the walking fail in the experiments. It is also an issue to obtain the energy and the phase with few noise components and without lag.

The goals of the lower layer are the acceleration control, the nominalization to the oscillator, and the stabilization control. As the above discussion, the limit of the lower layer affects the intermediate layer. Performance improvement of the nominalization control and the stabilization control contributes to extending applications of the proposed energy/phase control. While Chapter 5 employed a simple HZD for the stabilization control of the biped robot, another stabilization control can be applied. If a more stable stabilization control is employed, it is expected to realize more stable walking with efficiency. It is necessary to consider that the new stabilization control is located in the lower layer and does not interfere with the intermediate layer control.

Except for legged motion control, the proposed method has a possibility to be applied to other fields such as electrical systems. This is because the core of the proposal is for a harmonic oscillator in general.

References

[1] S. Sanji, “Case study in application and solution development of commercial robot: Current trends and future direction,” *Transactions of the Institute of Systems, Control and Information Engineers*, vol. 64, no. 11, pp. 442–447, 2020.

[2] T. Ganesharajah, N. G. Hall, and C. Sriskandarajah, “Design and operational issues in AGV-served manufacturing systems,” *Annals of Operations Research*, vol. 76, pp. 109–154, 1998.

[3] M. Zhong, Y. Yang, Y. Dessouky, and O. Postolache, “Multi-AGV scheduling for conflict-free path planning in automated container terminals,” *Computers and Industrial Engineering*, vol. 142, p. 106371, 2020.

[4] S. Riazi, K. Bengtsson, and B. Lennartson, “Energy optimization of large-scale AGV systems,” *IEEE Transactions on Automation Science and Engineering*, vol. 18, no. 2, pp. 638–649, 2021.

[5] S. S. Kim, J. Kim, F. Badu-Baiden, M. Giroux, and Y. Choi, “Preference for robot service or human service in hotels? Impacts of the COVID-19 pandemic,” *International Journal of Hospitality Management*, vol. 93, p. 102795, 2021.

[6] R. C. Luo, T. Y. Lin, and K. L. Su, “Multisensor based security robot system for intelligent building,” *Robotics and Autonomous Systems*, vol. 57, no. 3, pp. 330–338, 2009.

[7] C. A. My, S. S. Makhanov, N. A. Van, and V. M. Duc, “Modeling and computation of real-time applied torques and non-holonomic constraint forces/moment, and optimal design of wheels for an autonomous security robot tracking a moving target,” *Mathematics and Computers in Simulation*, vol. 170, pp. 300–315, 2020.

[8] M. Guettari, I. Gharbi, and S. Hamza, “UVC disinfection robot,” *Environmental Science and Pollution Research*, pp. 1–6, 2020.

[9] E. Guizzo, “By leaps and bounds: An exclusive look at how boston dynamics is redefining robot agility,” *IEEE Spectrum*, vol. 56, no. 12, pp. 34–39, 2019.

[10] G. A. Castillo, B. Weng, W. Zhang, and A. Hereid, “Robust feedback motion policy design using reinforcement learning on a 3D digit bipedal robot,” *arXiv preprint arXiv:2103.15309*, 2021.

[11] A. Paolillo, P. Gergondet, A. Cherubini, M. Vendittelli, and A. Kheddar, “Autonomous car driving by a humanoid robot,” *Journal of Field Robotics*, vol. 35, no. 2, pp. 169–186, 2018.

[12] Y. Gong, R. Hartley, X. Da, A. Hereid, O. Harib, J.-K. Huang, and J. Grizzle, “Feedback control of a cassie bipedal robot: Walking, standing, and riding a segway,” *2019 American Control Conference (ACC)*, pp. 4559–4566, 2019.

[13] C. L. Fernando, M. Furukawa, T. Kurogi, S. Kamuro, K. Sato, K. Minamizawa, and S. Tachi, “Design of TELESAR V for transferring bodily consciousness in telexistence,” *2012 IEEE/RSJ International Conference on Intelligent Robots and Systems (IROS)*, pp. 5112–5118, 2012.

[14] T. Nozaki and S. Hangai, “Telexistence and real haptics –fusion of humans and machines opens a new avenue–,” *Journal of the Robotics Society of Japan*, vol. 36, no. 10, pp. 668–672, 2018.

[15] K. Nagase and S. Katsura, “Feedback control of floor reaction force based on force-reflecting-type multilateral control,” *IEEJ Transactions on Industry Applications*, vol. 130, no. 3, pp. 351–359, 2010.

[16] D. K. Prasanga, “Advanced approaches in biped robot control for haptics applications,” Ph.D. dissertation, 2019.

[17] D. K. Prasanga, K. Tanida, K. Ohnishi, and T. Murakami, “Simultaneous bipedal locomotion based on haptics for teleoperation,” *Advanced Robotics*, vol. 33, no. 15-16, pp. 824–839, 2019.

[18] M. A. Sharbafi, K. Radkhah, O. von Stryk, and A. Seyfarth, “Hopping control for the musculoskeletal bipedal robot: BioBiped,” *2014 IEEE/RSJ International Conference on Intelligent Robots and Systems (IROS)*, pp. 4868–4875, 2014.

[19] T. Uchiyama, M. Kaneko, and Y. Kunii, “Academic roadmap of robotics from the viewpoint of engineering – what will happen in 2050?” *Advanced Robotics*, vol. 23, no. 11, pp. 1499–1503, 2009.

[20] K. Ogata, *Modern control engineering*. Prentice hall, 2010.

[21] Y. Kim and T. Singh, “Minimum energy control of a unicycle model robot,” *Journal of Dynamic Systems, Measurement, and Control*, vol. 143, no. 10, pp. 1–10, 2021.

[22] T. Mizoguchi, T. Nozaki, and K. Ohnishi, “A method to derive on time mechanical power factor,” *2014 IEEE International Conference on Industrial Technology (ICIT)*, pp. 73–78, 2014.

[23] S. Osada, T. Shimono, T. Mizoguchi, and K. Ohnishi, “Active motion evaluation by mechanical power factor analysis based on specific frequency component,” *IEEJ Journal of Industry Applications*, vol. 7, no. 3, pp. 244–249, 2018.

[24] K. Natori, “Mechanical power factor as performance index of bilateral teleoperation systems,” *2014 IEEE 13th International Workshop on Advanced Motion Control (AMC)*, no. 1, pp. 764–769, 2014.

[25] A. De and D. E. Koditschek, “Parallel composition of templates for tail-energized planar hopping,” *2015 IEEE International Conference on Robotics and Automation (ICRA)*, pp. 4562–4569, 2015.

[26] A. De and D. E. Koditschek, “Vertical hopper compositions for preflexive and feedback-stabilized quadrupedal bounding, pacing, pronking, and trotting,” *International Journal of Robotics Research*, vol. 37, no. 7, pp. 743–778, 2018.

[27] T. Kusaka, “Simultaneus realization of power assist and skill assist based on energy control and its application to semi-active assist mechanism,” Ph.D. dissertation, 2014.

[28] T. Kusaka, T. Tanaka, S. Kaneko, and H. Kajiwara, “Analysis of power assist effect during skill assist for periodic motions under use of semi-active assist mechanisms,” *2012 IEEE/RSJ International Conference on Intelligent Robots and Systems (IROS)*, pp. 758–763, 2012.

[29] T. Kusaka, T. Tanaka, and H. Kajiwara, “Skill assist efficiency control for periodical tasks based on phase difference limitation method of assist force under use of semi-active assist mechanisms,” *Journal of the Robotics Society of Japan*, vol. 32, no. 2, pp. 198–206, 2014.

[30] H. Kajiwara, “Hopping height control of hopping robot by periodic input control,” *Transactions of the Society of Instrument and Control Engineers*, vol. 49, no. 5, pp. 537–546, 2013.

[31] P. Terry and K. Byl, “A higher order partial feedback linearization based method for controlling an underactuated hopping robot with a compliant leg,” *53rd IEEE Conference on Decision and Control (CDC)*, pp. 2971–2978, 2014.

[32] K. Ohnishi, “Robust motion control by disturbance observer,” *Journal of the Robotics Society of Japan*, vol. 11, no. 4, pp. 486–493, 1993.

[33] K. Ohnishi, M. Shibata, and T. Murakami, “Motion control for advanced mechatronics,” *IEEE/ASME Transactions on Mechatronics*, vol. 1, no. 1, pp. 56–67, 1996.

[34] A. Šabanović and K. Ohnishi, *Motion control systems*. John Wiley & Sons, 2011.

[35] T. Murakami and K. Ohnishi, “A study of stability and workspace decoupling control based on robust control in multi-degrees-of-freedom robot,” *IEEJ Transactions on Industry Applications*, vol. 113, no. 5, pp. 639–646, 1993.

[36] N. Togashi, T. Yamashita, T. Shimono, N. Motoi, and N. Oda, “Verification of motion control method with estimated equivalent mass based on workspace observer,” *IEEJ Transactions on Industry Applications*, vol. 134, no. 2, pp. 115–126, 2014.

[37] N. Togashi, “Research on design of equivalent mass matrix for motion control based on workspace observer,” Ph.D. dissertation, 2016.

[38] C. Desoer and Y.-T. Wang, “On the generalized nyquist stability criterion,” *IEEE Transactions on Automatic Control*, vol. 25, no. 2, pp. 187–196, 1980.

[39] N. Hogan, “Impedance control: An approach to manipulation: Part I– Theory,” *Journal of Dynamic Systems, Measurement and Control, Transactions of the ASME*, vol. 107, no. 1, pp. 1–7, 1985.

[40] N. Hogan, “Impedance control: An approach to manipulation: Part II– Implementation,” *Journal of Dynamic Systems, Measurement and Control, Transactions of the ASME*, vol. 107, no. 1, pp. 8–16, 1985.

[41] N. Hogan, “Impedance control: An approach to manipulation: Part III– Applications,” *Journal of Dynamic Systems, Measurement and Control, Transactions of the ASME*, vol. 107, no. 1, pp. 17–24, 1985.

[42] N. Nishikawa, Y. Fujimoto, T. Murakami, and K. Ohnishi, “Variable compliance control for 3 dimensional biped robot considering environmental fluctuations,” *IEEJ Transactions on Industry Applications*, vol. 119, no. 12, pp. 1507–1514, 1999.

[43] S. Katsura and K. Ohnishi, “Human cooperative wheelchair for haptic interaction based on dual compliance control,” *IEEE Transactions on Industrial Electronics*, vol. 51, no. 1, pp. 221–228, 2004.

[44] A. Sayyad, B. Seth, and P. Seshu, “Single-legged hopping robotics research - A review,” *Robotica*, vol. 25, no. 5, pp. 587–613, 2007.

[45] K. Matsuoka, “A model of repetitive hopping movements in man,” in *5 th World Congress of Theory of Machines and Mechanisms*, vol. 2, 1979, pp. 1168–1171.

[46] M. H. Raibert, “Hopping in legged systems– Modeling and simulation for the two-dimensional one-legged case,” *IEEE Transactions on Systems, Man, and Cybernetics*, no. 3, pp. 451–463, 1984.

[47] M. H. Raibert, *Legged robots that balance*. MIT press, 1986.

[48] R. Blickhan, “The spring-mass model for running and hopping,” *Journal of biomechanics*, vol. 22, no. 11-12, pp. 1217–1227, 1989.

[49] O. H. Okubo, E. Nakano, and M. Handa, “Design of a jumping machine using self-energizing spring,” in *1996 IEEE/RSJ International Conference on Intelligent Robots and Systems (IROS)*, vol. 1, 1996, pp. 186–191.

[50] S.-H. Hyon and T. Mita, “Development of a biologically inspired hopping robot–“Kenken”,” in *2002 IEEE International Conference on Robotics and Automation (ICRA)*, vol. 4, 2002, pp. 3984–3991.

[51] J. W. Hurst, “The electric cable differential leg: a novel design approach for walking and running,” *International Journal of Humanoid Robotics*, vol. 8, no. 02, pp. 301–321, 2011.

[52] J. W. Grizzle, J. Hurst, B. Morris, H.-W. Park, and K. Sreenath, “MABEL, a new robotic bipedal walker and runner,” in *2009 American Control Conference*, 2009, pp. 2030–2036.

[53] K. Sreenath, H.-W. Park, I. Poulakakis, and J. W. Grizzle, “Embedding active force control within the compliant hybrid zero dynamics to achieve stable, fast running on MABEL,” *The International Journal of Robotics Research*, vol. 32, no. 3, pp. 324–345, 2013.

[54] M. Reis and F. Iida, “An energy-efficient hopping robot based on free vibration of a curved beam,” *IEEE/ASME Transactions on Mechatronics*, vol. 19, no. 1, pp. 300–311, 2014.

[55] M. H. Raibert, H. B. Brown Jr, and M. Chepponis, “Experiments in balance with a 3D one-legged hopping machine,” *The International Journal of Robotics Research*, vol. 3, no. 2, pp. 75–92, 1984.

[56] M. Raibert, M. Chepponis, and H. Brown, “Running on four legs as though they were one,” *IEEE Journal on Robotics and Automation*, vol. 2, no. 2, pp. 70–82, 1986.

[57] M. Ahmadi and M. Buehler, “Controlled passive dynamic running experiments with the ARL-Monopod II,” *IEEE Transactions on Robotics*, vol. 22, no. 5, pp. 974–986, 2006.

[58] M. Ishikawa, A. Neki, J. I. Imura, and S. Hara, “Energy preserving control of a hopping robot based on hybrid port-controlled Hamiltonian modeling,” *SICE 2003 Annual Conference*, vol. 2, pp. 1136–1141, 2003.

[59] S.-H. Hyon and T. Emura, "Energy-preserving control of a passive one-legged running," *Advanced Robotics*, vol. 18, no. 4, pp. 357–381, 2004.

[60] S. Kajita, K. Harada, E. Yoshida, H. Hirukawa, and K. Yokoi, *Humanoid robots*. Ohmsha, 2020.

[61] I. Kato, "Development of WABOT 1," *Biomechanism*, vol. 2, pp. 173–214, 1973.

[62] S. Sugano and I. Kato, "WABOT-2: Autonomous robot with dexterous finger-arm–Finger-arm coordination control in keyboard performance," *1987 IEEE International Conference on Robotics and Automation (ICRA)*, vol. 4, pp. 90–97, 1987.

[63] K. Hirai, M. Hirose, Y. Haikawa, and T. Takenaka, "The development of honda humanoid robot," *1998 IEEE International Conference on Robotics and Automation (ICRA)*, vol. 2, pp. 1321–1326, 1998.

[64] Y. Sakagami, R. Watanabe, C. Aoyama, S. Matsunaga, N. Higaki, and K. Fujimura, "The intelligent ASIMO: System overview and integration," *2002 IEEE/RSJ international Conference on Intelligent Robots and Systems (IROS)*, vol. 3, pp. 2478–2483, 2002.

[65] T. Takenaka, T. Matsumoto, and T. Yoshiike, "Real time motion generation and control for biped robot-1 st report: Walking gait pattern generation," *2009 IEEE/RSJ International Conference on Intelligent Robots and Systems (IROS)*, pp. 1084–1091, 2009.

[66] T. Takenaka, T. Matsumoto, T. Yoshiike, and S. Shirokura, "Real time motion generation and control for biped robot-2 nd report: Running gait pattern generation," *2009 IEEE/RSJ International Conference on Intelligent Robots and Systems (IROS)*, pp. 1092–1099, 2009.

[67] T. Takenaka, T. Matsumoto, and T. Yoshiike, "Real time motion generation and control for biped robot-3 rd report: Dynamics error compensation," *2009 IEEE/RSJ International Conference on Intelligent Robots and Systems (IROS)*, pp. 1594–1600, 2009.

[68] T. Takenaka, T. Matsumoto, T. Yoshiike, T. Hasegawa, S. Shirokura, H. Kaneko, and A. Orita, "Real time motion generation and control for biped robot-4 th report: Integrated balance control," *2009 IEEE/RSJ International Conference on Intelligent Robots and Systems (IROS)*, pp. 1601–1608, 2009.

[69] S. Shigemi, A. Goswami, and P. Vadakkepat, "ASIMO and humanoid robot research at Honda," *Humanoid robotics: A reference*, vol. 55, p. 90, 2018.

[70] T. Isozumi, K. Akachi, M. Hirata, K. Kaneko, S. Kajita, and H. Hirukawa, "Development of humanoid robot "HRP-2"," *Journal of the Robotics Society of Japan*, vol. 22, no. 8, pp. 1004–1012, 2004.

[71] K. Kaneko, K. Harada, F. Kanehiro, G. Miyamori, and K. Akachi, “Humanoid robot HRP-3,” *2008 IEEE/RSJ International Conference on Intelligent Robots and Systems (IROS)*, pp. 2471–2478, 2008.

[72] K. Kaneko, H. Kaminaga, T. Sakaguchi, S. Kajita, M. Morisawa, I. Kumagai, and F. Kanehiro, “Humanoid robot HRP-5P: An electrically actuated humanoid robot with high-power and wide-range joints,” *IEEE Robotics and Automation Letters*, vol. 4, no. 2, pp. 1431–1438, 2019.

[73] Y. Ishiguro, T. Makabe, Y. Nagamatsu, Y. Kojio, K. Kojima, F. Sugai, Y. Kakiuchi, K. Okada, and M. Inaba, “Bilateral humanoid teleoperation system using whole-body exoskeleton cockpit TABLIS,” *IEEE Robotics and Automation Letters*, vol. 5, no. 4, pp. 6419–6426, 2020.

[74] K. Kojima, Y. Kojio, T. Ishikawa, F. Sugai, Y. Kakiuchi, K. Okada, and M. Inaba, “Drive-rrain design in JAXON3-P and realization of jump motions: Impact mitigation and force control performance for dynamic motions,” *2020 IEEE/RSJ International Conference on Intelligent Robots and Systems (IROS)*, pp. 3747–3753, 2020.

[75] K. Kojima, Y. Kojio, T. Ishikawa, F. Sugai, Y. Kakiuchi, K. Okada, and M. Inaba, “Design method for weight saving based on joint drive force and frame stiffness and realization of jump motions by a lightweight and high-power humanoid JAXON3-P,” *Journal of the Robotics Society of Japan*, vol. 38, no. 10, pp. 975–984, 2020.

[76] I.-W. Park, J.-Y. Kim, J. Lee, and J.-H. Oh, “Mechanical design of the humanoid robot platform, HUBO,” *Advanced Robotics*, vol. 21, no. 11, pp. 1305–1322, 2007.

[77] I.-W. Park, J.-Y. Kim, J. Lee, and J.-H. Oh, “Online free walking trajectory generation for biped humanoid robot KHR-3 (HUBO),” *2006 IEEE International Conference on Robotics and Automation (ICRA)*, pp. 1231–1236, 2006.

[78] M. Zucker, S. Joo, M. X. Grey, C. Rasmussen, E. Huang, M. Stilman, and A. Bobick, “A general-purpose system for teleoperation of the DRC-HUBO humanoid robot,” *Journal of Field Robotics*, vol. 32, no. 3, pp. 336–351, 2015.

[79] G. Nelson, A. Saunders, N. Neville, B. Swilling, J. Bondaryk, D. Billings, C. Lee, R. Playter, and M. Raibert, “Petman: A humanoid robot for testing chemical protective clothing,” *Journal of the Robotics Society of Japan*, vol. 30, no. 4, pp. 372–377, 2012.

[80] M. Raibert, K. Blankespoor, G. Nelson, and R. Playter, “Bigdog, the rough-terrain quadruped robot,” *IFAC Proceedings Volumes*, vol. 41, no. 2, pp. 10 822–10 825, 2008.

[81] S. Kuindersma, R. Deits, M. Fallon, A. Valenzuela, H. Dai, F. Permenter, T. Koolen, P. Marion, and R. Tedrake, “Optimization-based locomotion planning, estimation, and control design for the atlas humanoid robot,” *Autonomous robots*, vol. 40, no. 3, pp. 429–455, 2016.

[82] K. Sreenath, H.-W. Park, I. Poulakakis, and J. W. Grizzle, “A compliant hybrid zero dynamics controller for stable, efficient and fast bipedal walking on MABEL,” *The International Journal of Robotics Research*, vol. 30, no. 9, pp. 1170–1193, 2011.

[83] A. Ramezani, J. W. Hurst, K. Akbari Hamed, and J. W. Grizzle, “Performance analysis and feedback control of ATRIAS, a three-dimensional bipedal robot,” *Journal of Dynamic Systems, Measurement, and Control*, vol. 136, no. 2, p. 021012, 2014.

[84] C. Hubicki, A. Abate, P. Clary, S. Rezazadeh, M. Jones, A. Peekema, J. Van Why, R. Domres, A. Wu, W. Martin *et al.*, “Walking and running with passive compliance: Lessons from engineering: A live demonstration of the ATRIAS biped,” *IEEE Robotics & Automation Magazine*, vol. 25, no. 3, pp. 23–39, 2018.

[85] J. Reher, W.-L. Ma, and A. D. Ames, “Dynamic walking with compliance on a cassie bipedal robot,” *2019 18th European Control Conference (ECC)*, pp. 2589–2595, 2019.

[86] Y. Gong, R. Hartley, X. Da, A. Hereid, O. Harib, J.-K. Huang, and J. Grizzle, “Feedback control of a Cassie bipedal robot: Walking, standing, and riding a segway,” *2019 American Control Conference (ACC)*, pp. 4559–4566, 2019.

[87] T. Apgar, P. Clary, K. Green, A. Fern, and J. W. Hurst, “Fast online trajectory optimization for the bipedal robot Cassie,” *Robotics: Science and Systems*, vol. 101, p. 14, 2018.

[88] S. N. Yadukumar, M. Pasupuleti, and A. D. Ames, “Human-inspired underactuated bipedal robotic walking with amber on flat-ground, up-slope and uneven terrain,” *2012 IEEE/RSJ International Conference on Intelligent Robots and Systems (IROS)*, pp. 2478–2483, 2012.

[89] A. D. Ames, “Human-inspired control of bipedal walking robots,” *IEEE Transactions on Automatic Control*, vol. 59, no. 5, pp. 1115–1130, 2014.

[90] H.-H. Zhao, W.-L. Ma, A. D. Ames, and M. B. Zeagler, “Human-inspired multi-contact locomotion with amber2,” *2014 ACM/IEEE International Conference on Cyber-Physical Systems (ICCPS)*, pp. 199–210, 2014.

[91] J. Reher, E. A. Cousineau, A. Hereid, C. M. Hubicki, and A. D. Ames, “Realizing dynamic and efficient bipedal locomotion on the humanoid robot DURUS,” *2016 IEEE International Conference on Robotics and Automation (ICRA)*, pp. 1794–1801, 2016.

[92] A. E. Martin, D. C. Post, and J. P. Schmiedeler, "Design and experimental implementation of a hybrid zero dynamics-based controller for planar bipeds with curved feet," *The International Journal of Robotics Research*, vol. 33, no. 7, pp. 988–1005, 2014.

[93] A. E. Martin and J. P. Schmiedeler, "Predicting human walking gaits with a simple planar model," *Journal of biomechanics*, vol. 47, no. 6, pp. 1416–1421, 2014.

[94] C. Hubicki, A. Abate, P. Clary, S. Rezazadeh, M. Jones, A. Peekema, J. V. Why, R. Domres, A. Wu, W. Martin, H. Geyer, and J. Hurst, "Walking and running with passive compliance," *IEEE Robotics & Automation Magazine*, vol. 25, pp. 23–39, 2018.

[95] S. Kajita, M. Morisawa, K. Miura, S. Nakaoka, K. Harada, K. Kaneko, F. Kanehiro, and K. Yokoi, "Biped walking stabilization based on linear inverted pendulum tracking," *2010 IEEE/RSJ International Conference on Intelligent Robots and Systems (IROS)*, pp. 4489–4496, 2010.

[96] T. Kamioka, H. Kaneko, M. Kuroda, C. Tanaka, S. Shirokura, M. Takeda, and T. Yoshiike, "Dynamic gait transition between walking, running and hopping for push recovery," *2017 IEEE-RAS 17th International Conference on Humanoid Robotics (Humanoids)*, pp. 1–8, 2017.

[97] E. R. Westervelt, J. W. Grizzle, C. Chevallereau, J. H. Choi, and B. Morris, *Feedback control of dynamic bipedal robot locomotion*. CRC Press, 2007.

[98] G. Garofalo, C. Ott, and A. Albu-Schäffer, "Walking control of fully actuated robots based on the bipedal SLIP model," *2012 IEEE International Conference on Robotics and Automation (ICRA)*, pp. 1456–1463, 2012.

[99] N. Scianca, D. De Simone, L. Lanari, and G. Oriolo, "MPC for humanoid gait generation: Stability and feasibility," *IEEE Transactions on Robotics*, vol. 36, no. 4, pp. 1171–1188, 2020.

[100] P.-B. Wieber, "Model predictive control for biped walking motion generation," *Journal of the Robotics Society of Japan*, vol. 32, no. 6, pp. 503–507, 2014.

[101] S. Faraji, S. Pouya, C. G. Atkeson, and A. J. Ijspeert, "Versatile and robust 3d walking with a simulated humanoid robot (atlas): A model predictive control approach," *2014 IEEE International Conference on Robotics and Automation (ICRA)*, pp. 1943–1950, 2014.

[102] P. Zaytsev, W. Wolfslag, and A. Ruina, "The boundaries of walking stability: viability and controllability of simple models," *IEEE Transactions on Robotics*, vol. 34, no. 2, pp. 336–352, 2018.

[103] S. Kajita, H. Hirukawa, K. Harada, and K. Yokoi, *Introduction to humanoid robotics*. Springer, 2014.

[104] S. Kajita, F. Kanehiro, K. Kaneko, K. Yokoi, and H. Hirukawa, “The 3D linear inverted pendulum mode: A simple modeling for a biped walking pattern generation,” *2001 IEEE/RSJ International Conference on Intelligent Robots and Systems (IROS)*, vol. 1, pp. 239–246, 2001.

[105] P. Kormushev, B. Ugurlu, S. Calinon, N. G. Tsagarakis, and D. G. Caldwell, “Bipedal walking energy minimization by reinforcement learning with evolving policy parameterization,” *2011 IEEE/RSJ International Conference on Intelligent Robots and Systems (IROS)*, pp. 318–324, 2011.

[106] J. Ding, C. Zhou, and X. Xiao, “Energy-efficient bipedal gait pattern generation via CoM acceleration optimization,” *2018 IEEE-RAS 19th International Conference on Humanoid Robotics (Humanoids)*, pp. 238–244, 2018.

[107] H.-K. Shin and B. K. Kim, “Energy-efficient gait planning and control for biped robots utilizing vertical body motion and allowable ZMP region,” *IEEE Transactions on Industrial Electronics*, vol. 62, no. 4, pp. 2277–2286, 2018.

[108] S. Arimoto and F. Miyazaki, “A hierarchical control scheme for biped robots,” *Journal of the Robotics Society of Japan*, vol. 1, no. 3, pp. 167–175, 1983.

[109] J. Luo, Y. Su, L. Ruan, Y. Zhao, D. Kim, L. Sentis, and C. Fu, “Robust bipedal locomotion based on a hierarchical control structure,” *Robotica*, vol. 37, no. 10, pp. 1750–1767, 2019.

[110] I. Sugiura and M. Suzuki, “Sensitivity analysis and optimum-design of automatic control systems with sensitivity consideration,” *Journal of the Society of Instrument and Control Engineers*, vol. 8, no. 7, pp. 443–457, 1969.

[111] M. Okada, A. Pekarovskiy, and M. Buss, “Robust trajectory design for object throwing based on sensitivity for model uncertainties,” *2015 IEEE International Conference on Robotics and Automation (ICRA)*, pp. 3089–3094, 2015.

[112] Y. Yamanaka, W. Hijikata, and M. Okada, “Robust controller design based on dynamic sensitivity analysis,” *2018 JSME Annual Conference on Robotics and Mechatronics (Robomec)*, vol. 2018, pp. 2P2–E11, 2018.

[113] Y. Abe and S. Katsura, “Compensation of nonlinear dynamics for energy/phase control of hopping robot,” *Precision Engineering*, vol. 69, pp. 36–47, 2021.

[114] S. Kajita, T. Yamaura, and A. Kobayashi, “Dynamic walking control of a biped robot along a potential energy conserving orbit,” *IEEE Transactions on Robotics and Automation*, vol. 8, no. 4, pp. 431–438, 1992.

[115] T. Takenaka, T. Matsumoto, T. Yoshiike, and S. Shirokura, “Running gait generation for biped robot with horizontal force limit,” *Journal of the Robotics Society of Japan*, vol. 29, no. 9, pp. 849–856, 2011.

List of Achievements

Journals (As the first author)

[1] Yoshitaka Abe and Seiichiro Katsura, “Energy Disturbance Observer for Estimation and Control of Reaction Energy,” *IEEJ Journal of Industry Applications*, Vol. 3-D, No. 4, pp. 335–343, 2014.

[2] Yoshitaka Abe and Seiichiro Katsura, “Compensation of Nonlinear Dynamics for Energy/Phase Control of Hopping Robot,” *Precision Engineering*, Vol. 69, pp. 36–47, 2021.

International Conference (As the first author)

[1] Yoshitaka Abe and Seiichiro Katsura, “Energy Bilateral Control for a New Control Scheme,” *The 39th Annual Conference of the IEEE Industrial Electronics Society, IECON ’13-VIENNA*, pp. 6118–6123, 2013.

[2] Yoshitaka Abe and Seiichiro Katsura, “Stabilization Control of a 2-mass Resonant System Based on Energy Control Theory,” *The 13th International Workshop on Advanced Motion control (AMC’ 2014-YOKOHAMA, JAPAN)*, pp. 225–230, 2014.

[3] Yoshitaka Abe and Seiichiro Katsura, “Stabilizing Control of a Nonlinear Two-mass System Based on Energy Control,” *The 1st IEEJ International Workshop on Sensing, Actuation, and Motion Control (SAMCON’ 2015-NAGOYA, JAPAN)*, TT1-1-5, 2015.

[4] Yoshitaka Abe, Kuo Chen, Mitja Trkov, Jingang Yi, and Seiichiro Katsura, “Control of Robotic Biped Walkers under Foot Slip,” *The 1st International Symposium on Applied Abstraction and Integrated Design (AAID’ 2017-YOKOHAMA, JAPAN),*, RS-4-2, 2017.

[5] Yoshitaka Abe, Kuo Chen, Mitja Trkov, Jingang Yi, and Seiichiro Katsura, “Disturbance Observer-Based HZD Control of Bipedal Walking and Slip Recovery,” *Dynamic Walking 2017-MARIEHAMN, FINLAND),*, No. 365, 2017.

[6] Yoshitaka Abe, Kuo Chen, Mitja Trkov, Jingang Yi, and Seiichiro Katsura, "Disturbance Observer-Based Balance Control of Robotic Biped Walkers under Slip," *The 2017 IEEE International Conference on Advanced Intelligent Mechatronics (AIM' 2017-MUNICH, GERMANY),*, pp. 1489–1494, 2017.

[7] Yoshitaka Abe and Seiichiro Katsura, "Hopping-Height and Oscillation-Timing Control with Optimal Design of Spring Parameters," *The 4th IEEJ International Workshop on Sensing, Actuation, and Motion Control (SAMCON' 2018-TOKYO, JAPAN)*, TT11-6, 2018.

[8] Yoshitaka Abe and Seiichiro Katsura, "Force Command Generation of Hopping-Height Control Based on Energy Control," *The 5th IEEJ International Workshop on Sensing, Actuation, and Motion Control (SAMCON' 2019-CHIBA, JAPAN)*, SS3-2, 2019.

[9] Yoshitaka Abe and Seiichiro Katsura, "High-Power and Precise Actuation System with Direct Drive and Variable Structured Elasticity," *The 2019 IEEE International Conference on Mechatronics (ICM' 2019-ILMENAU, GERMANY),*, pp. 396–401, 2019.

[10] Yoshitaka Abe and Seiichiro Katsura, "Energy/Phase Control Based on Harmonic Oscillator for Hopping Height Control of a Legged Robot," *The 6th IEEJ International Workshop on Sensing, Actuation, and Motion Control (SAMCON' 2020-TOKYO, JAPAN)*, SS16, 2020.

[11] Yoshitaka Abe and Seiichiro Katsura, "Energy/Phase Control Based on Harmonic Oscillator for Hopping Height Control of a Legged Robot," *The 2nd International Symposium on Applied Abstraction and Integrated Design (AAID' 2020-YOKOHAMA, JAPAN),*, TS-2-4, 2020.

[12] Yoshitaka Abe and Seiichiro Katsura, "Energy-Efficient Biped Walking Speed Control Based on Energy/Phase Control of Linear Inverted Pendulum," *The SICE Annual Conference 2021 (SICE' 2021-TOKYO, JAPAN),*, 2021.

International Conferences (As the Co-author)

[1] Masahiro Komuta, Yoshitaka Abe, and Seiichiro Katsura, "Walking Control of Bipedal Robot on Soft Ground Considering Ground Reaction Force," *The 2017 IEEE International Symposium on System Integration (SII' 2017-TAIWAN),*, pp. 318–323, 2017.

[2] Yuji Ogintani, Yoshitaka Abe, and Seiichiro Katsura, "Trajectory Planning of Biped Robot Based on Spatio-temporal Scaling of Sprinter's Running Form," *The SICE Annual Conference 2019 (SICE' 2019-HIROSHIMA, JAPAN),*, pp. 433–436, 2019.

Domestic Conference (As the first author)

[1] Yoshitaka Abe and Seiichiro Katsura, “Environment State Estimation Using Reaction Energy Observer,” *The 2013 Annual Meeting of the Institute of Electrical Engineers of Japan*, pp. 284–285, 2013.

[2] Yoshitaka Abe and Seiichiro Katsura, “Estimation and Control of Reaction Energy,” *The IEEJ Papers of Technical Meeting on Industrial Instrumentation and Control, IIC ’13*, pp.49–54, 2013.

[3] Yoshitaka Abe and Seiichiro Katsura, “Reaction Work Observer for Disturbance Observation of Robots in 2-mass Resonant Systems,” *The 31st Annual Conference of the Robotics Society of Japan (RSJ2013)*, 1N2-03, 2013.

[4] Yoshitaka Abe and Seiichiro Katsura, “Mechanical Energy Control Based on Calculus on the Space for Robot Control,” *The 2013 Annual Conference of the Japan Society of Mechanical Engineering (JSME2013)*, G151051, 2013.

[5] Yoshitaka Abe and Seiichiro Katsura, “Energy-Dimensional Bilateral Control for Extension of Motion Area,” *The IEEJ Papers of Technical Meeting on Mechatronics Control, MEC ’13*, pp.47–52, 2013.

[6] Yoshitaka Abe and Seiichiro Katsura, “Mechanical Energy Control for Application of a Linear Control Systems to a Nonlinear Pendulum Robot,” *The 2014 Annual Meeting of the Institute of Electrical Engineers of Japan*, pp. 281–282, 2014.

[7] Yoshitaka Abe and Seiichiro Katsura, “Mechanical Energy Control for Steady Hopping of One-Leg Hopping Robot,” *The JSME Annual Conference on Robotics and Mechatronics (ROBOMECH2015)*, 2A2-Q09, 2015.

[8] Yoshitaka Abe and Seiichiro Katsura, “Decomposed Control for a Legged Hopping Robot Based on Leg-Length and Leg-Angle Modal Transformation,” *The 2017 Annual Meeting of the Institute of Electrical Engineers of Japan*, pp. 464–465, 2017.

[9] Yoshitaka Abe and Seiichiro Katsura, “Hitting Control of a Ball Based on Force Control,” *The JSME Annual Conference on Robotics and Mechatronics (ROBOMECH2015)*, 2P2-G09, 2018.

[10] Yoshitaka Abe and Seiichiro Katsura, “Hopping-Height Control of a Legged Robot by Energy/Phase Control Based on Harmonic Oscillator,” *The IEEJ Papers of Technical Meeting on Mechatronics Control, MEC ’19*, pp.39–44, 2019.

Domestic Conference (As the co-author)

[1] Hirotoshi Masuda, Yoshitaka Abe, and Seiichiro Katsura, “Study of Spinning Ball Trajectory by Hitting Using Variable-structured Elastic Actuator,” *The 2019 Annual Meeting of the Institute of Electrical Engineers of Japan*, pp. 328–329, 2019.

[2] Yuji Ogitani, Yoshitaka Abe, and Seiichiro Katsura, “Running Control of a Biped Robot Inspired by Sprinter ’ s Running Form,” *The 2019 Annual Meeting of the Institute of Electrical Engineers of Japan*, pp. 330–331, 2019.

Awards

[1] “Hatakeyama Award”
Japan Society of Mechanical Engineers
March, 2013

Career

[1] April 2013∼March 2018
Research Associate
the Program for Leading Graduate School for “Science for Development of Super Mature Society”
from the Ministry of Education, Culture, Sport, Science, and Technology in Japan